600 Jahre Universität Rostock

Traditio et Innovatio

Investigation of Mesospheric instabilities: Observations and Direct Numerical Simulations

Dissertation to

obtain the academic degree of Doctor of Engineering (Dr.-Ing)

from the Faculty of Mechanical Engineering and Marine Technologies at the University of Rostock

by

Kesava Prasad Ramachandran

from Chennai, India

Reviewers:

Prof. Dr. Sven Grundmann, University of Rostock

Prof. Dr. Jorge. L. Chau, Leibniz Institute of Atmospheric Physics

Date of submission: 30.11.2023

Date of defense: 23.04.2024

https://doi.org/10.18453/rosdok_id00004757

44.5mm27.5mm



Dieses Werk ist lizenziert unter einer
Creative Commons Namensnennung - Weitergabe unter gleichen Bedingungen 4.0 International Lizenz.



This work is licensed under a Creative Commons Attribution 4.0 International License.

Abstract

Instabilities play an important role in understanding the energy balance of the atmosphere. This thesis focuses on investigating atmospheric instabilities with horizontal wavelengths of less than a few kilometers in the Mesosphere and Lower Thermosphere (MLT) region. To this effect, we report a particular kind of gravity wave event called the mesospheric undular bore observed over Germany using airglow imagers. Mesospheric bores are a type of non-linear response that causes the amplification of gravity waves, due to trapping, which is characterized by a propagating step-like jump followed by undulating waves. A notable aspect of this observation is the rapid dissipation of the bore within the imager's field of view. The observation was complemented by a two-dimensional Direct Numerical Simulation (DNS) of the Navier-Stokes equations under the Boussinesq approximation using a pseudo-spectral framework. The DNS results successfully replicated crucial characteristics of the observed airglow event, such as nonlinear wave-steepening, the number of trailing waves, and their dissipation. These results were achieved by introducing a thermal duct and a wave-like perturbation.

Furthermore, the DNS results suggest that, under specific background conditions, the system produces a solitary wave response with a high peak amplitude, bearing a resemblance to recently observed MLT extreme vertical drafts in terms of morphology. Additionally, the inclusion of a Doppler duct (wind shear) alongside the thermal duct led to the generation of secondary instabilities that have been previously reported in observations, accompanying both bores and solitary waves. Our findings also indicate that the thermal and Doppler ducts that control the background environment, must have sufficient magnitude to impact instability generation. Moreover, when the background was regulated solely by the Doppler duct , the system did not produce bores or solitary waves, underscoring the essential role of the thermal duct in bore generation. We also extended the existing DNS to three dimensions (3D), and the results led to the conclusion that kilometer-scale dynamics are also influenced by the generation of secondary instabilities in the direction transverse to the propagation direction.

Zusammenfassung

Instabilitäten spielen eine wichtige Rolle für das Verständnis des Energiehaushalts der Atmosphäre. Diese Arbeit konzentriert sich auf die Untersuchung von kilometergroßen Instabilitäten mit horizontalen Wellenlängen von weniger als 100 km in der Mesosphäre und der unteren Thermosphäre (MLT) Region. Zu diesem Zweck berichten wir über eine besondere Art von Schwerewellenereignis namens mesosphärische Gezeitenwelle (Bore)., die über Deutschland mit Hilfe von Airglow-Imagern beobachtet wurden. Mesosphärische Gezeitenwelle sind eine Art nichtlineare Reaktion, die aufgrund von räumlicher Eingrenzung zu einer Verstärkung von Schwerewellen führt, die durch einen fortschreitenden stufenartigen Sprung, gefolgt von wellenförmigen Bewegungen, gekennzeichnet ist. Ein bemerkenswertes Merkmal dieser Beobachtung ist die schnelle Auflösung der Gezeitenwelle innerhalb des Sichtfelds des Imagers. Die Beobachtung wurde durch zweidimensionale DNS der Navier-Stokes-Gleichungen unter der Boussinesq-Approximation ergänzt. Die DNS-Ergebnisse reproduzierten erfolgreich entscheidende Eigenschaften des beobachteten Airglow-Ereignisses, die Anzahl der nachfolgenden Wellen und ihre Auflösung, innerhalb eines thermischen Kanals und durch das Auftreten wellenförmiger Störungen.

Des Weiteren legen die DNS-Ergebnisse nahe, dass das System unter spezifischen Hintergrundbedingungen eine isolierte Wellenreaktion mit einer hohen Spitzenamplitude erzeugt, die in Bezug auf die Morphologie Ähnlichkeiten mit extremen vertikalen Aufwinden aufweist. Zusätzlich führte die Einbeziehung des Doppler-Kanals(Windgradient) neben dem thermischen Kanal zur Erzeugung von sekundären Instabilitäten, die zuvor in Beobachtungen sowohl bei Gezeitenwellen als auch bei isolierten Wellen berichtet wurden. Unsere Ergebnisse deuten auch darauf hin, dass die thermischen und Doppler-Kanäle, die die Hintergrundumgebung für die Wellen darstellen, eine ausreichende Ausprägung haben müssen, um die Generierung von Instabilitäten zu beeinflussen. Darüber hinaus produzierte das System bei einer Regulierung des Hintergrunds ausschließlich durch den Doppler-Kanal weder Gezeitenwellen noch isolierte Wellen, was die wesentliche Rolle des thermischen Kanals bei der Entstehung von atmosphärischen Gezeitenwellen unterstreicht. Wir erweiterten die bestehende DNS auf drei Dimensionen (3D), und diese Ergebnisse führten zu dem Schluss, dass kilometergroße Dynamiken auch von der Erzeugung sekundärer Instabilitäten in Richtung quer zur Ausbreitungsrichtung beeinflusst werden.

Acknowledgements

First of all, I would like to thank my advisors, Prof. J. L. Chau and Prof. S. Grundmann, for their excellent guidance during my doctoral studies. Specially to Prof. J. L. Chau who encouraged me to start this journey and has supported me during my stay at the Institute of Atmospheric Physics, Kuehlungsborn. I will deeply miss our conversations and discussions, and even more his pieces of advice.

I also want to thank my parents and my brother for their love and support for my entire life. Likewise, I would like to give special thanks to my girlfriend Juliana Jaen for her love and unwavering support during this journey.

I also like to thank my IAP mates for their company and interesting discussions. It was truly a great experience working with you.

Contents

1 Introduction **1**

1.1 Earth's atmosphere . . . 2
1.2 MLT dynamics . . . 4
1.3 Objective of this thesis: Connecting observations and numerical simulations . . 5
1.4 Outline of the thesis . . . 7

2 Basic Physics and Mathematics of Atmospheric Dynamics **9**

2.1 Waves . . . 9
2.2 Wave parameters . . . 10
2.2.1 Wave scales . . . 10
2.2.2 Wave phase and Wave speed . . . 11
2.2.3 Group velocity . . . 11
2.3 Linear theory of gravity waves . . . 13
2.3.1 Taylor-Goldstein equation . . . 13
2.4 Thermodynamics of the atmosphere . . . 16
2.4.1 Equation of state . . . 16
2.4.2 Hydrostatic Approximation . . . 16
2.4.3 Scale Height . . . 17
2.4.4 Adiabatic process . . . 17
2.4.5 Static stability . . . 19
2.5 Equations of Atmospheric Motion . . . 21
2.6 Frames of reference: Lagrangian and Eulerian frame . . . 24

3 Atmospheric Instabilities **25**

3.1 Instabilities and Turbulence . . . 25
3.1.1 Kelvin-Helmholtz Instability . . . 27
3.1.2 Ekman instability . . . 31
3.1.3 Rayleigh-Benard instability . . . 32
3.2 Bores and Solitary waves: Theory and Observation . . . 34

3.2.1 Analogy to Hydraulic Jump: A Linear model of mesospheric bores 41

4 Observation techniques to study atmospheric instabilities in the MLT 43
4.1 Tools to study kilometer-scale instabilities: Airglow imagers and Satellites 43
4.2 Using Noctilucent clouds to study atmospheric dynamics 45
4.3 Observing Polar Summer Mesospheric Echoes (PMSE) using MAARSY 47

5 Direct Numerical Simulations for studying instabilities in the MLT 50
5.1 Direct Numerical Simulations 50
5.2 Dedalus: A Pseudo-spectral solver for solving partial differential equations . . . 51
5.3 Simulation setup in Dedalus 52
5.4 Selection of grid resolution and basis system 53
5.5 Effects of vertical boundaries 55

6 Case study of a dissipating mesospheric bore: Observation and Direct Numerical Simulations 57
6.1 Observation of mesospheric undular bore in Airglow Imagers 58
6.2 Background conditions during the bore propagation: Temperature and Stability profiles 63
6.3 Background conditions during the bore propagation: Winds and Vertical Wavenumber 65
6.4 2D Direct Numerical Simulations of bore 68

7 Direct numerical simulations of instabilities and bores: 2D and 3D DNS 73
7.1 Effect of the thermal duct and the amplitude of initial perturbation on the instability generation 74
7.2 Instability generation in dual ducts: Thermal and Doppler ducts 82
7.2.1 Formation of secondary instabilities in dual ducts 87
7.2.2 Formation of solitary waves in dual ducts 89
7.3 Generation of instabilities in vertically displaced ducts 92
7.4 Effect of viscosity on instability formation 94
7.5 Effect of the inversion layer magnitude 98
7.6 Can bores form in only Doppler ducts? 104
7.7 Three-dimensional simulation of instabilities 106

8 Summary and Outlook 111

A List of peer-reviewed publications 115

B Boussinesq Approximation **116**

Symbols and Acronyms **119**

List of Figures **121**

List of Tables **128**

Bibliography **128**

Chapter 1

Introduction

In this chapter

1.1 Earth's atmosphere 2
1.2 MLT dynamics 4
1.3 Objective of this thesis: Connecting observations and numerical simulations 5
1.4 Outline of the thesis 7

"I was observing the motion of a boat which was rapidly drawn along a narrow channel by a pair of horses, when the boat suddenly stopped—not so the mass of water in the channel which it had put in motion; it accumulated round the prow of the vessel in a state of violent agitation, then suddenly leaving it behind, rolled forward with great velocity, assuming the form of a large solitary elevation,… which I have called the Wave of Translation. "

Report on Waves. 1845, John Scott Russell

The above passage by John Scott Russell is the first recorded observation of a solitary wave in a channel flow. This observation and the following decades of theoretical research by Lord Rayleigh and others have laid the foundational work on nonlinear waves, particularly concerning solitary waves and bores. Until a couple of decades ago, there was very little interest concerning undular bores and solitary waves in the upper atmospheric community although observations have been

reported in the lower troposphere, the most prominent being the "Morning Glory" clouds. While the presence of waves in the atmosphere is not scarce, the sightings of bores and solitary waves are rare and not an everyday occurrence. However, before delving deep into the topic of undular bores, solitary waves, and associated kilometer-scale instabilities, the reader is given a gentle introduction to the features of Earth's atmosphere, particularly Mesosphere and Lower Thermosphere (MLT) which is the region of Earth's atmosphere between roughly 55-120 km.

1.1 Earth's atmosphere

The Earth's atmosphere is a highly dynamic region that is largely dominated by waves of many scales, instabilities, and turbulence (Wallace and Hobbs, 2006). These dynamical processes interact with each other regularly covering different spatial and temporal scales. To understand and characterize them, both observations and modeling efforts are required and should complement each other. More often, the observations require combining multiple instruments like radars, lidars, airglow imagers, sounding rockets, and satellite observations. There are advantages and disadvantages when it comes to a particular instrument and hence co-located observations of the entire atmosphere by different instruments provide a complete picture in understanding atmospheric dynamics. Figure 1.1 shows the different layers of the atmosphere. The troposphere is the lowest layer of Earth's atmosphere and is neutrally stable or weakly stratified for the most part. Its relative homogeneity results from convection: during the day the sun warms the ground and the heat is transferred to the air above it by convection leading to the movement of air masses (Sutherland, 2010). Almost all of the Earth's weather phenomena occur in this layer. The troposphere is bounded above by tropopause which marks the start of temperature inversion. The altitude of the tropopause is around 16 km in the equatorial regions and around 9 km at the poles. Above the troposphere is the stratosphere which extends to about 50 km altitude. This layer is relatively strongly stratified due to the increase of temperature with height hence the name. The stratification is strong due to chemistry: ozone which is produced in large quantities in the equatorial stratosphere efficiently absorbs solar radiation heating the air so that the temperature increases with height (Sutherland, 2010).

The relatively weakly stratified layer that extends from stratopause to about 90 km is the mesosphere. There is less prominence of ozone here and the internal heating is weaker. The mesospause which demarcates the upper boundary of the mesosphere is the region of the coldest temperatures on the Earth (Lübken, 1999). The stratosphere and the mesosphere together are called the

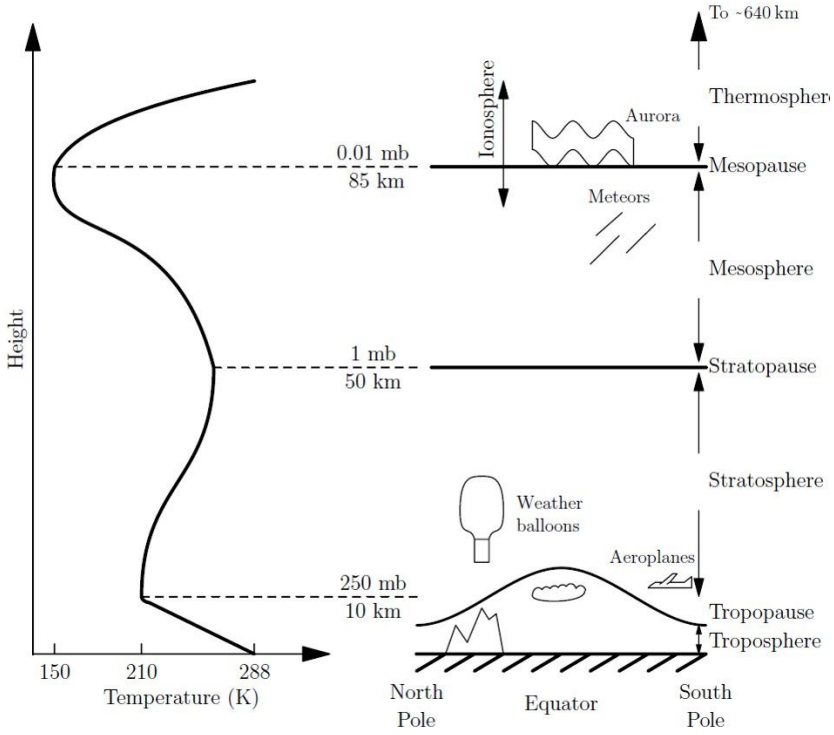


Figure 1.1: Schematic representing the vertical structure of the atmosphere. The four main layers are illustrated. Figure taken from (Sutherland, 2010)

middle atmosphere. The thermosphere extends above the mesosphere to about 600 km altitude, beyond which is the exosphere and space. The internationally accepted boundary to outer space, the Kármán line, is in the lower thermosphere at 100 km (Wallace and Hobbs, 2006; Sutherland, 2010). The altitude between 50 and 120 km is commonly referred to as the Mesosphere and Lower Thermosphere (MLT) region. This region of the atmosphere is still poorly understood due to the constraints it poses to in-situ measuring instruments such as rockets, due to costs, and is inaccessible for others like balloons, aircraft, satellites, and drones. Continuous measurements in the MLT regions can only be obtained using ground- and satellite-based remote-sensing techniques. However, it's important to note that these tools do have limitations, particularly in their ability to accurately resolve global flows down to their smallest scales where energy dissipation becomes important. Concurrently, great strides have been made in recent years in improving atmospheric models to accurately resolve the small-scale flow structures.

1.2 MLT dynamics

The Mesosphere and Lower Thermosphere is a region that exhibits a balance of processes that set it apart from any other region of the atmosphere and hence is treated as a separate entity (Smith, 2012). Even with the observational limitations, much has been learned about MLT in recent years. In order to understand the dynamics of the MLT, it is important to characterize the background state of the region, namely the temperature balance, the interaction of waves with the background wind and themselves, coupling between the MLT and the other regions of the atmosphere. A detailed review of the above-mentioned processes is given in Smith (2012). Figure 1.2 shows the theoretical horizontal and vertical kinetic energy spectra as a function of wavenumber along with the different regimes of turbulence. The planetary scales which are the largest scales of motion in the atmosphere are an important component in understanding the dynamics as they carry most of the energy that may cascade down to small scales. The horizontal length scales of these motions are in the range of a few thousand kilometers while timescales range from several weeks to months. Some examples of these waves are Rossby waves and Kelvin waves (Vallis, 2017). At-

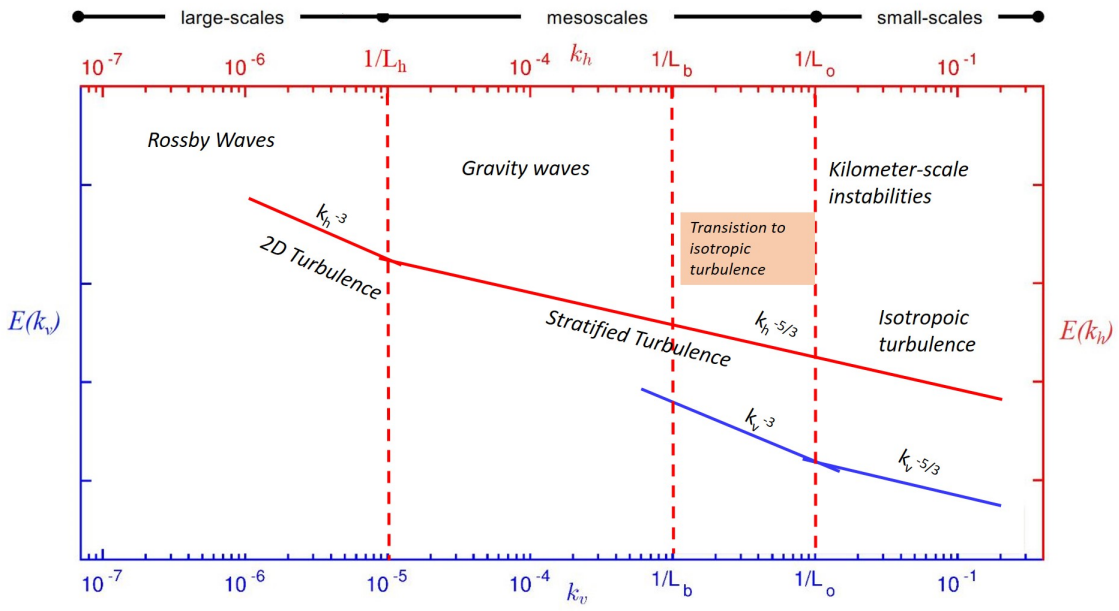


Figure 1.2: Theoretical horizontal and vertical kinetic energy spectrum diagram describing the scales of motion in which regimes are dominated by Rossby Waves, gravity waves, and isotropic turbulence. The X-axis (log scale) represents the wavenumber while the Y-axis represents the energy content. Figure adapted from (Urco Cordero, 2020)

mospheric tides are gravity wave modes whose period is one day or an integral fraction of a day

(Smith, 2012). The tides that are seen in the MLT region have their source in the lower altitudes, modified by local conditions. The atmospheric tides can lead to large variations in winds, temperature, density, airglow emissions, etc (Fritts and Alexander, 2003; Smith, 2012). One of the major sources of tides is the diurnal variation in the heating in the troposphere that comes from the absorption of sunlight by water vapor and latent heat release (Smith, 2012). On the other hand heating in the stratosphere is due to the absorption of ultraviolet radiation by ozone.

In the MLT, the transport of energy and momentum across the different scales takes place through complex processes and one of the main drivers of this complex process is the atmospheric gravity waves (GW). These waves have horizontal length scales between hundreds of kilometers to tens of kilometers. They are one of the main sources of the energy budget in this region due to their ability to travel large distances carrying momentum and energy with them. Three features of GW are important, namely, the generation, propagation, and dissipation (Fritts and Alexander, 2003). Sources of these GW include topography where the waves generated in the lower atmosphere propagate vertically upwards, spontaneous generation, convection, and wave-mean flow interaction leading to the generation of additional waves (Fritts and Alexander, 2003; Smith, 2012). They play an important role in the transport of energy and momentum from the lower atmosphere to higher altitudes such as the mesosphere or even to the upper thermosphere. As the waves propagate vertically, their amplitudes increase due to decreasing neutral density and conservation of angular momentum. At the mesospheric altitudes, they become significant and unstable owing to these large amplitudes thereby breaking and leading to the generation of instability and turbulence (Fritts and Alexander, 2003; Sutherland, 2010; Nappo, 2013). The deposition of momentum due to these processes can greatly alter the background flow by either accelerating or decelerating it (Nappo, 2013). The effects of GW are not only seen in winds but also in temperature fluctuations, neutral air density, and electron density (Hauchecorne et al., 1987; Lübken et al., 1990). These effects are realized using a variety of instruments such as radars, lidars, balloons, airplanes, satellites, cameras, and rockets by measuring the changes in the parameters. Furthermore, global circulation models and observations have pointed to the importance of GW in the vertical coupling between the lower and middle atmosphere (Fritts and Alexander, 2003; Smith, 2012).

1.3 Objective of this thesis: Connecting observations and numerical simulations

The primary goal of this thesis is to delve into the kilometer-scale dynamics of mesospheric instabilities through the combined use of observational capabilities and direct numerical simulations.

The instabilities under consideration exhibit horizontal scales ranging from a few kilometers to tens of kilometers and extend vertically over approximately 3 to 5 kilometers.

As mentioned above, with the recent advancements in techniques like better spatial and temporal coverage of the observable atmosphere (Latteck et al., 2012; Conte et al., 2021), improved imaging techniques to quantify dynamical structures in three-dimensions (Urco et al., 2019), good progress has been made on characterizing the small-scale structures. Figure 1.3 shows two such observations of the kilometer-scale structures that were observed using the Polar Mesospheric Summer Echoes (PMSE) as tracers. The left side of the figure shows the first four-dimensional characterization of Kelvin-Helmholtz (KH) instability showing billow structures in both the spanwise (XZ-cut) and streamwise (XY-cut) direction (Chau et al., 2020). The right side shows the observation of extreme mesospheric vertical drafts where the reported values were more than five standard deviations larger than the observed vertical wind variability (Chau et al., 2021). Both of the reported observations have a horizontal and vertical extent of less than 10 km. In addition to

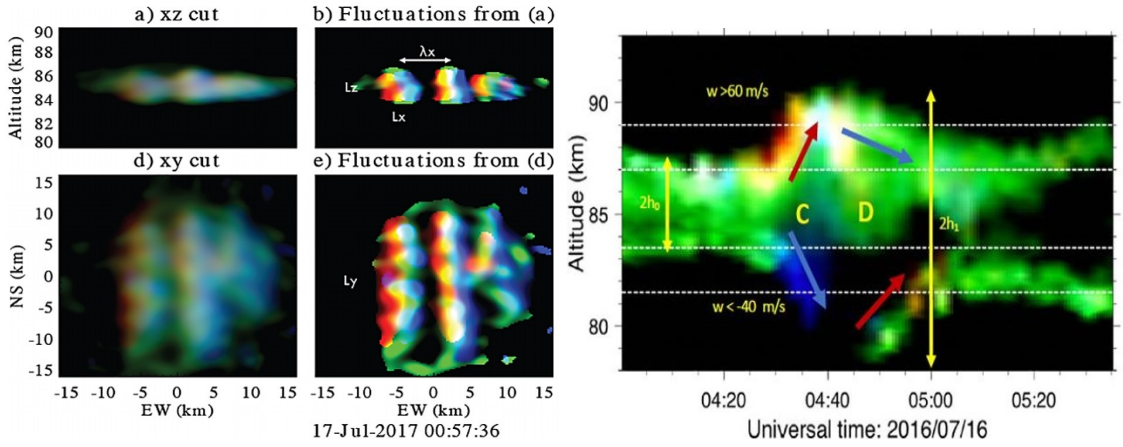


Figure 1.3: (Left) 2D cuts of PMSE images of KHI with spanwise and streamwise orientation. Figure taken from (Chau et al., 2020) (Right) PMSE observation of extreme vertical velocities in the order of 50 m/s in up and downdrafts. Figure taken from (Chau et al., 2021). In both the figures, red indicates positive (upwards) velocity, and blue indicates negative (downwards) velocity.

these recent radar observations, the usage of airglow imagers to investigate kilometer-scale structures like mesospheric bores and solitary waves has been going on for several years (Dewan and Picard, 1998; Smith et al., 2003; She et al., 2004). The airglow imagers cover also a much larger observational area compared to radars but the vertical information of these structures is lost since one can only obtain 2D information. Consequently, even if the radars offer limited horizontal coverage, one can characterize the small-scale structures in multi-dimensions as a result of the new radar imaging technique which is important for discerning their dynamics (Urco et al., 2019).

While observations can provide the realistic variables that are needed to investigate the kilometer-scale dynamics, they cannot characterize the state that exists a priori to the observation. This characterization is only possible when numerical simulations are utilized to complement the observations. Seyler (2005), Laughman et al. (2009), Fritts et al. (2014), Feraco et al. (2018), Hysell and Larsen (2021), Dong et al. (2021), and Fritts et al. (2023) have extensively used direct numerical simulations (DNS) to study mesospheric bores, solitary waves, KH instabilities, extreme vertical drafts, and other small-scale structures in the MLT. While whole atmospheric general circulations models are useful, their limitations of not resolving kilometer-scale structures, both in terms of spatial and temporal scales, makes them not an optimal framework pertaining to the studies of these kilometer-scale instabilities. In contrast, by using DNS we can resolve these smallest scales of motion by numerically resolving them directly instead of parameterizing them. Seyler (2005) developed a 2D DNS based on the Navier-Stokes equations under Boussinesq approximation to simulate the undular bores by considering parameters that are relevant in the mesospheric altitudes where the background is controlled by only thermal duct. This was the first attempt to connect mesospheric undular bore observations with the underlying theory. Laughman et al. (2009) later extended the work of Seyler (2005) by taking into consideration not only the thermal duct but also the Doppler duct. Since these two studies, no consistent numerical approach has been undertaken to study mesospheric bores and solitary waves. In this study, we wish to bridge the gap between observations and simulations by employing DNS to investigate and reproduce observed mesospheric instability events. We also extend the simulations by investigating the effects various parameters like the amplitude of the perturbation, duct width, inversion layer strength, viscosity, etc. have on the bore generation. Finally, we broaden our numerical simulation of the above-mentioned instabilities to 3D.

1.4 Outline of the thesis

The structure of the thesis is as follows: Chapter 2 begins with introducing the fundamentals of wave mechanics, defining wave parameters like wavelength, wavenumber, phase, and group speed. An overview of the linear theory of internal gravity waves and the dispersion relation is provided. The second half of this chapter deals with the fundamental thermodynamic properties of the atmosphere and equations that govern atmospheric dynamics under the Boussinesq approximation. In Chapter 3, the theory of atmospheric instabilities is presented. This includes a comprehensive discussion on the undular bores, and the existing theories to explain their dynamics and formative mechanisms. Other common atmospheric instabilities like Kelvin-Helmholtz

instability, Ekman-layer instability, and Rayleigh-Benard instability are also explained. Chapter 4 gives a brief overview of the instruments that were used in our investigation of mesospheric dynamics. Chapter 5 gives an introduction to the pseudo-spectral solver Dedalus and Direct Numerical Simulations (DNS). In Chapter 6, we report the case study of a dissipating mesospheric undular bore using an airglow imager and DNS. Chapter 7 presents the results of the comprehensive DNS experiments to understand the mesospheric instabilities in their various forms. We conclude the chapter by presenting some first results of 3D mesospheric instabilities. Chapter 8 provides the summary and future research outlook.

Chapter 2

Basic Physics and Mathematics of Atmospheric Dynamics

In this chapter

2.1 Waves 9
2.2 Wave parameters 10
2.3 Linear theory of gravity waves 13
2.4 Thermodynamics of the atmosphere 16
2.5 Equations of Atmospheric Motion 21
2.6 Frames of reference: Lagrangian and Eulerian frame 24

2.1 Waves

A wave can be considered a manifestation of periodic oscillations of fluid particles whose motions are associated with the transport of momentum and energy. A fluid that is stably stratified can support wave motions (Sutherland, 2010). Figure 2.1 shows the schematic representation of wave presence in the atmosphere. These waves could be traveling upward in every direction. We would also see waves moving upwards like 'wiggles' increasing in frequency and magnitude and depending on the background conditions either being transmitted or reflected. It would constitute a picture of complexity and unending variety. The vertical transport of energy and momentum is

accomplished more readily by small-scale gravity waves than planetary or synoptic-scale waves (Fritts and Alexander, 2003). Depending on the feature of the wave, (i.e.) where they occur, they are classified as internal and external waves. External waves are the ones that occur on the surface of the fluids. Ocean waves are examples of surface waves that occur at the air-sea interface. Internal gravity waves occur within the body of the fluid where the restoring force is gravity. Another class of waves are the inertial-gravity waves where the Coriolis force, in addition to buoyancy, acts to restore equilibrium.



Figure 2.1: A schematic of atmospheric gravity waves. Figure from (Hines, 1974)

2.2 Wave parameters

2.2.1 Wave scales

In this thesis work, the cartesian coordinate system (*x*,*y*,*z*) is used with *x* and *y* in the horizontal plane and *z* in the vertical direction. *Wavelength* λ, is defined as the distance between two successive crests or troughs of a wave. The horizontal *wavenumber* which is a fundamental property of a wave is normally denoted by *k* and is related to the wavelength by

$$k = \frac{2\pi}{\lambda}. \tag{2.1}$$

In three dimensions,the wavenumbers in *x*, *y*, and *z*, are labelled *k*,*l*, and *m*, respectively,

$$k = \frac{2\pi}{\lambda_x}, l = \frac{2\pi}{\lambda_y}, m = \frac{2\pi}{\lambda_z}, \tag{2.2}$$

where $\lambda_x, \lambda_y, \lambda_z$ are the wavelengths in x, y, and z directions, respectively. A schematic of the wave vector with its corresponding wavefronts of a two-dimensional wave is shown in Figure 2.2. The horizontal and vertical wavenumbers, k and m are also denoted. We can think of the wavenumber as 2π times the number of wave oscillations per unit length, or wavelength per unit radian. The wave period τ, is the time required for the fluid particles to make one oscillation. For a wave moving in a still medium, the wave period is the time required for the successive wave crests to pass a stationary point or an observer. The angular frequency ω, is 2π times the number of wave oscillations per unit time or radians per second,

$$\omega = \frac{2\pi}{\tau}. \tag{2.3}$$

2.2.2 Wave phase and Wave speed

The speed with which the wave troughs or crests move is called phase speed. The direction of the speed of propagation is called the phase velocity. Let us describe a 1D wave having the amplitude A, wavenumber k, and frequency ω as $A\cos(kx - \omega t)$. The minus sign indicates that the wave is moving in the positive x-direction. Let ϕ be the phase angle $\phi = kx - \omega t$. In the x-z plane, the wave in two dimensions can be denoted by the following expression,

$$\phi = \mathbf{k} \cdot \mathbf{r} - \omega t = kx + mz - \omega t, \tag{2.4}$$

where $\mathbf{r}$ is the position vector defined by $\mathbf{r} = x\mathbf{x} + z\mathbf{z}$ and the magnitude of the $\mathbf{k}$ is $|\mathbf{k}| = \sqrt{k^2 + m^2}$. To determine the phase speed of the wave a point on the wave is picked, say the wave crest and it is followed along the direction of propagation. Differentiating the equation 2.4, with respect to time t, we get

$$\frac{d\phi}{dt}_{\phi} = \mathbf{k} \cdot \frac{d\mathbf{r}}{dt} - \omega = 0, \tag{2.5}$$

and consequently,

$$\frac{d\mathbf{r}}{dt} = c = \frac{\omega}{|\mathbf{k}|} = \frac{\omega}{\sqrt{k^2 + m^2}}. \tag{2.6}$$

where c is the phase speed of the wave.

2.2.3 Group velocity

More dynamically essential and more difficult to perceive than the phase velocity is the group velocity, denoted by c_g, which is the velocity at which the energy of the wave packet is transported

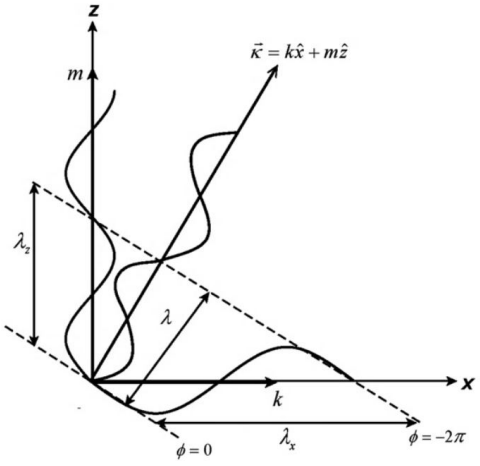


Figure 2.2: An illustration of a two-dimensional wave with its corresponding horizontal and vertical components. The wavefronts are perpendicular to the wave vector. Figure from (Nappo, 2013)

by the small amplitude waves. The phase velocity and group velocity may have different magnitude and direction of propagation. So, if one intends to infer the transport of energy, one should not just look at the direction of propagation of the waves. Imagine that a stone is thrown into a pond of still water. There will be a ring wave that spreads away from the center. If we could follow the wave, we would see that the surface of the wave is disturbed continually by the ever-present smaller waves that translate from the rear to the front of the wave, called the wavelets. Hence one can say that the initial disturbance had created a spectrum of waves spread over a range of wavenumbers and travel as wave packets. As the wavelets move from the rear to the front, their wavelength increases and moves faster. The energy of the initial disturbance is contained in the wave packets that are observed on the surface of the water. The rate of change of the phase ϕ of the wave is given by $2\pi/\tau = \omega$, which is the angular frequency. But the phase is also a function of distance, x, since at a given time the phase decreases in value, with increasing distance. The phase satisfies the following relations

$$\frac{\partial \phi}{\partial x} = -k\frac{\partial \phi}{\partial t} = \omega\frac{\partial k}{\partial t} + \frac{\partial \omega}{\partial x} = 0. \tag{2.7}$$

ω can also be considered as a function of the k, (i.e.) $\omega = \omega(k)$. Equation 2.7 can be written as

$$\frac{\partial k}{\partial t} + \frac{d\omega}{dk}\frac{\partial k}{\partial x} = 0. \tag{2.8}$$

Here we define the group velocity as $c_g = d\omega/dk$.

2.3 Linear theory of gravity waves

Linear wave theory gives a linearized description of the gravity waves in a homogeneous fluid layer. Many of the properties of gravity waves can be understood from the linear theory which describes a simplified set of linear equations (Hines, 1960). The process of linearization involves expanding a state variable, say q into a background state q_0 and first-order perturbation q_1. The mean background flow is thought to be steady or slowly varying and uniform in the horizontal direction but varying vertically. The perturbation q_1 is assumed to be much smaller than the mean state q_0 and that the product of the perturbations is infinitesimally small. These small perturbations can be caused due to turbulence, and other instabilities but in the linear theory only the perturbation related to gravity waves is considered. Although the linear theory with its simplistic approach is a useful tool to understand the nature of gravity waves, it is not without its cost. In the realistic atmosphere, waves interact with other waves, and wave breaking can lead to turbulence and interaction with the mean flow whose effects are not readily quantified in the linear theory (Fritts and Alexander, 2003). While linear theory describes the possible disturbance of an existing state, the dynamic theory tells the consequences of the forces acting to change the motions of the system (Nappo, 2013). Hence, linear theory can only predict the possible wave states in a fluid (Fritts and Alexander, 2003; Nappo, 2013).

2.3.1 Taylor-Goldstein equation

The Taylor-Goldstein equation describes the dynamics of internal waves in the medium of a stratified fluid (Sutherland, 2010; Nappo, 2013). It is the linearized version of Navier-Stokes equations in the presence of gravity and density gradient. We consider the 2D Euler equations for irrotational, frictionless, adiabatic flow under Boussinesq approximation

$$\frac{\partial u}{\partial t} + u\frac{\partial u}{\partial x} + w\frac{\partial u}{\partial z} = -\frac{1}{\rho}\frac{\partial p}{\partial x} \tag{2.9}$$

$$\frac{\partial w}{\partial t} + u\frac{\partial w}{\partial x} + w\frac{\partial w}{\partial z} = -\frac{1}{\rho}\frac{\partial p}{\partial z} - g \tag{2.10}$$

$$\frac{\partial u}{\partial x} + \frac{\partial w}{\partial z} = 0 \tag{2.11}$$

$$\frac{\partial \rho}{\partial t} + u\frac{\partial \rho}{\partial x} + w\frac{\partial \rho}{\partial z} = 0. \tag{2.12}$$

Now we define the mean state and the perturbation as follows

$$q(x,z,t) = q_0(z) + q_1(x,z,t). \tag{2.13}$$

Assuming that the background flow is in hydrostatic balance, equations 2.9-2.12 yield

$$\frac{\partial u_1}{\partial t} + u_0\frac{\partial u_1}{\partial x} + w_1\frac{du_0}{\partial z} = -\frac{1}{\rho_0}\frac{\partial p_1}{\partial x} \tag{2.14}$$

$$\frac{\partial w_1}{\partial t} + u_0\frac{\partial w_1}{\partial x} = -\frac{1}{\rho_0}\frac{\partial p_1}{\partial z} - \frac{\rho_1}{\rho_0}g \tag{2.15}$$

$$\frac{\partial u_1}{\partial x} + \frac{\partial w_1}{\partial z} = 0 \tag{2.16}$$

$$\frac{\partial \rho_1}{\partial t} + u_0\frac{\partial \rho_1}{\partial x} + w_1\frac{d\rho_0}{\partial z} = 0, \tag{2.17}$$

where $\rho_0(z)$ is the background atmospheric density. Assuming that a solution exists for the above equations in the form

$$q_1(x,z,t) = \tilde{q}(z)e^{i(kx-\omega t)}, \tag{2.18}$$

and using equation 2.18 in equations 2.14-2.17 we get,

$$-i\omega\tilde{u} + iu_0k\tilde{u} + \tilde{w}\frac{du_0}{dz} = -\frac{i}{\rho_0}k\tilde{p} \tag{2.19}$$

$$-i\omega\tilde{w} + iu_0k\tilde{w} = -\frac{1}{\rho_0}\frac{d\tilde{p}}{dz} - \frac{\tilde{\rho}}{\rho_0}g \tag{2.20}$$

$$ik\tilde{u} + \frac{d\tilde{w}}{dz} = 0 i\omega\tilde{\rho} + iu_0k\tilde{\rho} + \tilde{w}\frac{d\rho_0}{dz} = 0. \tag{2.21}$$

The intrinsic frequency Ω is defined as the frequency that is measured relative to the flow, given by,

$$\Omega = \omega - u_0k \tag{2.22}$$

where ω is the frequency measured by the observer in a coordinate system that is fixed, and u_0 is the background wind. Using equation 2.22 in the equations 2.19-2.21, we get the *polarization equations*

$$i\Omega\tilde{u} - \tilde{w}\frac{du_0}{dz} = \frac{i}{\rho_0}k\tilde{p}, \tag{2.23}$$

$$i\Omega\tilde{w} = \frac{1}{\rho_0}\frac{d\tilde{p}}{dz} + \frac{\tilde{\rho}}{\rho_0}g, \tag{2.24}$$

$$ik\tilde{u} + \frac{d\tilde{w}}{dz} = 0, \tag{2.25}$$

$$i\Omega\tilde{\rho} - \tilde{w}\frac{\rho_0}{g}N^2 = 0 \tag{2.26}$$

Solving for $\tilde{w}$, we get

$$\frac{d^2\tilde{w}}{dz^2} + \left[\frac{N^2}{(c-u_0)^2} + \frac{u_0''}{(c-u_0)} - -\frac{1}{4H_s^2} - k^2\right]\tilde{w} = 0 \tag{2.27}$$

This is the Taylor-Goldstein equation for atmospheric gravity waves, where $u_0'' = \frac{d^2u_0}{dz^2}$, *c* is the phase speed, u_0 is the background wind speed and H_s is the scale height. The term inside the square brackets on the left-hand side of the equation 2.27 is commonly denoted by m^2 which is the vertical wavenumber defined in §2.2 used to determine the vertical propagation characteristics of the wave. If $m^2 > 0$ then vertical propagation of the waves is allowed. If $m^2 < 0$, then the vertical propagation of the waves is prohibited and these are called evanescent waves. This relation plays an important role in the prediction of the formation of ducts. The first term inside the brackets of the above equation $N^2/(c-u_0)^2$ is called the buoyancy term which influences whether *m* is real or complex. The second term $u_0''/(c-u_0)$ is the curvature term which becomes important when there is a strong background wind shear. $1/4H_s^2$ is the compressibility term since the scale height is a function of density and the last term k^2 is the non-hydrostatic term. When *c* is equal u_0 then $c - u_0$ is zero. The altitude at which this happens is called the critical level. In the case of zero background wind and $\lambda << H_s$, the Taylor-Goldstein equation reduces to,

$$\frac{d^2\tilde{w}}{dz^2} + \left[\frac{k^2N^2}{\omega^2} - k^2\right]\tilde{w} = 0. \tag{2.28}$$

The general solution is

$$\tilde{w}(z) = A\,e^{imz} + B\,e^{-imz}, \tag{2.29}$$

where *m* is the vertical wavenumber given by

$$m^2 = k^2\left[\frac{N^2}{\omega^2} - 1\right], \tag{2.30}$$

and *A* and *B* are the positive and negative branches of the solution. Solving the equation 2.30 for ω gives the dispersion relation,

$$\omega = \pm\frac{kN}{\sqrt{(k^2+m^2)}}. \tag{2.31}$$

$$\omega = ck = \pm\frac{kN}{\sqrt{(k^2+m^2)}}. \tag{2.32}$$

A schematic of the dispersion effects is shown in Figure 2.3 In equation 2.30 if $\omega < N$, then *m* is real and the wave is said to be propagating or internal. If $\omega > N$, then *m* is imaginary and the

wave is said to be evanescent or external.

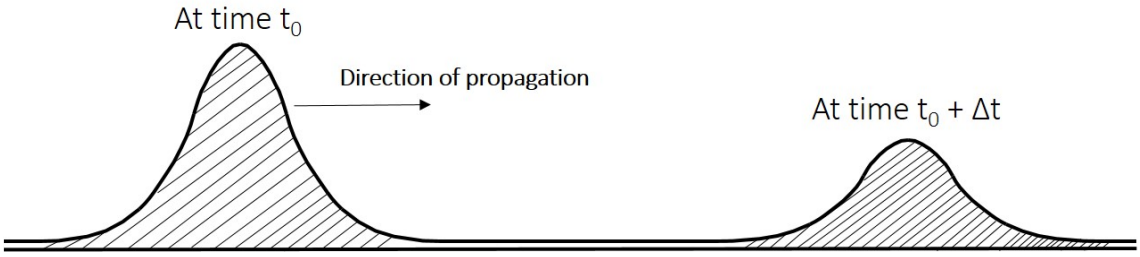


Figure 2.3: A cross-section of a wave showing the effects of wave dispersion at early and later times.

2.4 Thermodynamics of the atmosphere

2.4.1 Equation of state

The thermodynamic state of the atmosphere is determined by the values of pressure p, temperature T, and density (or specific volume) at any given point. These variables are related to each other for dry air by the equation of state for an ideal gas by,

$$p = \rho RT. \tag{2.33}$$

where R is the universal gas constant for dry air ($R = 287 J/kg/K$)

2.4.2 Hydrostatic Approximation

In the atmosphere, the pressure of the air decreases with increasing altitude hence creating a pressure difference between the different levels of the atmosphere. This pressure difference causes an upward force called the pressure-gradient force. The force of gravity which can be considered as constant over the Earth acts to balance this thereby keeping the atmosphere bounded to the Earth. In other words, the pressure-gradient force prevents gravity from collapsing the atmosphere, whereas gravity prevents the pressure-gradient force from diffusing the atmosphere into outer space. Consider an elemental volume of atmosphere with unit cross-section height δz, and

density ρ. The weight of the volume is $g\rho\delta z$, and this force is directed downward. The pressure force acting on the volume is different at the top and bottom. Let this difference $\delta\rho$. The balance between the pressure and gravity forces gives

$$\delta p = -\rho g \delta z. \tag{2.34}$$

In the limit of small δz, equation 2.34 becomes,

$$\frac{\partial p}{\partial z} = -\rho g. \tag{2.35}$$

which is generally referred to as the hydrostatic equation.

2.4.3 Scale Height

The scale height is the height within which some parameter, such as pressure or density, decreases by a factor of $1/e$ in an isothermal atmosphere. This is obtained by substituting equation 2.33 into equation 2.35 leading to

$$\frac{1}{\rho}\frac{\partial p}{\partial z} + \frac{1}{T}\frac{\partial T}{\partial z} = -\frac{-g}{RT}. \tag{2.36}$$

Integrating the equation 2.36 over z gives,

$$\rho(z) = \rho_0 e^{-gz/RT_0}, \tag{2.37}$$

where ρ_0 is the density at the surface and T_0 is the averaged temperature. If we define the isothermal scale height *H* of the atmosphere to be RT_0/g, then equation 2.37 becomes

$$\rho(z) = \rho_0 e^{-z/H}. \tag{2.38}$$

Equation 2.38 shows that the density decreases exponentially with height.

2.4.4 Adiabatic process

Any material that changes its physical state (e.g., its pressure, temperature, or volume) without the addition or removal of heat is said to be under an adiabatic state.

Concept of an Air Parcel: In fluid mechanics, mixing is considered to be due to the random motion of individual molecules. In the atmosphere, the mixing is mainly due to the vertical exchange of the macroscale "air parcels" with the horizontal scale ranging from a few meters to the scale of the earth itself (Wallace and Hobbs, 2006). An air parcel is a parcel large enough to contain a very great number of molecules, but small enough so that the properties assigned to it are approximately uniform within it. To gain insights into the vertical motions of the air parcels, two important parameters, namely the adiabatic lapse rate and potential temperature, need to be defined.

Dry adiabatic lapse rate: Here we will derive the expression for the rate of change of temperature as a function of height for a dry air parcel. Since we are considering only an adiabatic process and if one assumes that the hydrostatic equilibrium is valid for a unit mass of air parcel, then the work done by the air parcel is given by

$$d(c_p T + \Phi) = 0. \tag{2.39}$$

where Φ is the geopotential of the Earth. The geopotential Φ at any point in the Earth's atmosphere is defined as the work that must be done against the Earth's gravity to raise a mass of 1 kg from sea level to that point and is given by $d\Phi = gdz$. Using this equation 2.39, we get

$$-\left(\frac{dT}{dz}\right) = \frac{g}{c_p} \equiv \Gamma_d, \tag{2.40}$$

where Γ_d is the dry adiabatic lapse rate. Due to the expansion of the air parcel as it rises in the atmosphere, its temperature will decrease with height and hence Γ_d given by the equation2.40 is positive. Upon substituting the known values of $g = 9.81\ m\ s^{-2}$ and specific heat, $c_p = 1004\ J\ K^{-1}\ kg^{-1}$ gives $\Gamma_d = 9.8\ K\ km^{-1}$ which is the value of the adiabatic lapse rate of dry air. It is to be noted here that the above expression is the rate of change of the temperature following a parcel of dry air.

Potential Temperature: The potential temperature θ, of a dry air parcel is defined as the temperature that a parcel of air would have if it were expanded or compressed adiabatically from its existing pressure and temperature to standard pressure p_0 (1000 hPa). The potential temperature can be expressed in terms of the state variables, p and T. From the first law of thermodynamics, we have

$$c_p dT - \alpha dp = 0. \tag{2.41}$$

where $\alpha = 1/\rho$ is the specific volume of the air parcel. Substituting equation 2.33 in the 2.41

$$\frac{c_p}{R}\frac{dT}{T} - \frac{dp}{p} = 0. \tag{2.42}$$

Integrating equation 2.42 from a state of p_0 and T to a state in which the pressure is p and temperature is θ, we get

$$\frac{c_p}{R}\log\left(\frac{T}{\theta}\right) = \log\left(\frac{p}{p_0}\right). \tag{2.43}$$

Taking antilog on both sides,

$$\left(\frac{T}{\theta}\right)^{c_p/R} = \frac{p}{p_0}, \tag{2.44}$$

or

$$\theta = T\left(\frac{p_0}{p}\right)^{R/c_p}. \tag{2.45}$$

Potential temperature is a conserved quantity for an air parcel and is a useful parameter since most atmospheric processes are often close to adiabatic and hence the potential temperature remains essentially constant, just like density in an incompressible fluid.

2.4.5 Static stability

The ability of the air parcel at rest to become turbulent or laminar due to the effects of buoyancy is called stability. Here we refer to only the stability of dry air, where the effects of moisture are neglected. Let's consider a layer of atmosphere in which the actual rate of temperature decrease, given by Γ, is less than the dry adiabatic lapse rate Γ_d as shown in Figure 2.4(a). If a parcel of dry air originally located at point X is raised to the height defined by points A and B, its temperature will fall to T_A which is less than the temperature T_B at this level. Also since the parcel will then adjust to the surrounding ambient air pressure, according to the ideal gas equation this parcel will be colder and hence denser than the warmer ambient air. As a result, this parcel will tend to return to its original level. If the parcel is displaced downward from X, it becomes warmer and hence lighter than the ambient air and will tend to rise back to its original level. In both cases, the parcel of air encounters a restoring force after the initial displacement and returns to its equilibrium level. In this scenario, the atmosphere is said to be stably stratified ($\Gamma < \Gamma_d$). The larger the difference $\Gamma_d - \Gamma$, the greater the restoring force for a given displacement and hence the greater the static stability. Hence wave motions are possible only when the atmosphere is stably stratified (i.e. $d\theta/dz > 0$). Atmospheric layers with negative lapse rates (temperature increasing with height) are called inversions. In the lower atmosphere, the inversions can act as a "lid" that traps the pollution-laden air beneath it. If $\Gamma > \Gamma_d$ as is illustrated in Figure 2.4(b), a parcel of dry air displaced upward from X, will arrive at point A with a higher temperature than the surroundings, it will be less dense than the ambient environment and hence will continue to rise. Similarly, if the air parcel is displaced downwards, then it will be cooler than the ambient

air and hence will continue to sink if left to itself. Such a situation is called statically unstable. The nature of the atmosphere is such that it tries to bring itself back to equilibrium conditions by strong vertical mixing.

An important parameter to establish the measure of the stability of the environment is the Brunt-Vaisala frequency or the buoyancy frequency given by

$$N^2 = \frac{g}{\theta}\frac{d\theta}{dz}, \tag{2.46}$$

where θ is the averaged potential temperature of the environment. The three stability criteria for dry air, based on the change of temperature with height, are,

$$d\theta/dz > 0 \text{ statically stable}$$
$$d\theta/dz = 0 \text{ statically neutral}$$
$$d\theta/dz < 0 \text{ statically unstable.}$$

The period of buoyancy oscillation in the troposphere is about 8 min while it is about 4 min in the mesosphere.

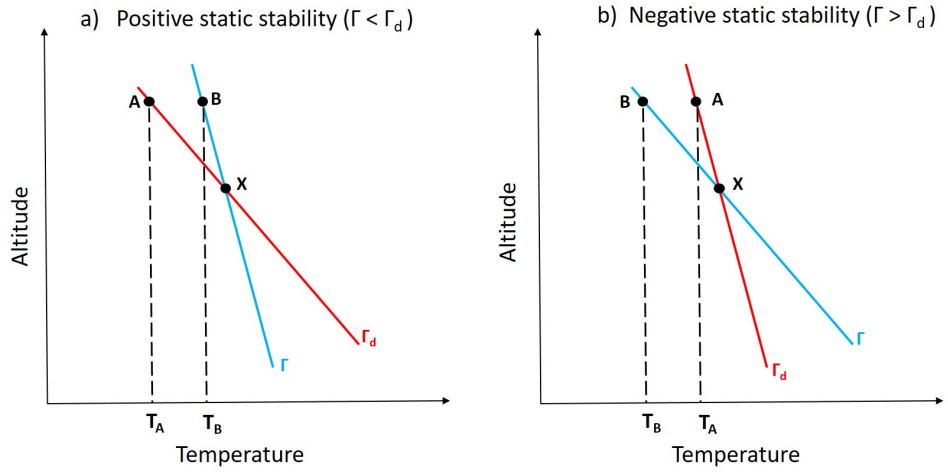


Figure 2.4: An illustration to describe the conditions of stability of a displaced dry air parcel in the atmosphere. a) Positive static stability $\Gamma > \Gamma_d$, b) Negative static stability $\Gamma < \Gamma_d$

2.5 Equations of Atmospheric Motion

From Newton's second law of motion, the momentum equation that is most commonly used in dynamic meteorology and atmospheric physics is as follows,

$$\frac{D\mathbf{u}}{Dt} = -2\Omega \times \mathbf{u} - \frac{1}{\rho}\nabla p + \mathbf{g} + \nu\nabla^2\mathbf{u}. \tag{2.47}$$

In the above equation, we have made use of the material derivative, which is defined as follows,

$$\frac{D}{Dt} = \frac{\partial}{\partial t} + u\frac{\partial}{\partial x} + v\frac{\partial}{\partial y} + w\frac{\partial}{\partial z} = \frac{\partial}{\partial t} + \mathbf{u}\cdot\nabla. \tag{2.48}$$

Equation 2.47 states that the acceleration following the relative motion of an air parcel in a rotating frame equals the sum of the gravity or buoyancy, the pressure gradient force, viscosity, and Coriolis force.

- **The buoyancy force** - On Earth, all fluids feel the force of gravity. It is a downward pointing vector whose magnitude is the effective acceleration due to gravity. In the cartesian coordinate system, **g** = -g**z**. In most geophysical applications a constant value of $9.80\ m\ s^{-2}$ is considered.
- **Pressure gradient force** - The pressure gradient force drives the fluid from the regions of high pressure to regions of low pressure. In the Earth's atmosphere, the air pressure decreases with altitude, creating a height pressure gradient that is counteracted by the Earth's gravity.
- **Viscous force** - Viscosity is a force due to the internal motion of the molecules. The effects of viscosity are negligible in the large-scale flows in the atmosphere. In incompressible fluids under the Boussinesq approximation, the only way for the energy to be removed from the fluid is due to the action of viscosity. This generally depends on the length and the time scales over which viscosity does indeed influence the flow. The typical value of kinematic viscosity near the mesopause altitudes is around $10\ m^2\ s^{-1}$ (Hines, 1960; Seyler, 2005).
- **Coriolis force** - Coriolis force is an apparent force that acts on a fluid moving in a rotating, accelerating (non-inertial) frame of reference. This force impacts the large-scale motions of the atmosphere and ocean on the rotating Earth. The time, length, and velocity scales are important in determining the effect of the Coriolis force on the fluid. The importance

of rotation on the fluid can be estimated by the non-dimensional Rossby number which is the ratio of inertial force to the Coriolis force

$$Ro = \frac{U}{Lf} \tag{2.49}$$

where *U* and *L* are the characteristic velocity and length scales,respectively, f is the Coriolis parameter, given by $f = 2\Omega sin\phi$ and ϕ is the Earth's latitude. A small *Ro* signifies that the influence of Earth's rotation is significant and cannot be neglected. This is typically in the cases of cyclones and other large-scale weather systems where the Coriolis force exerts a significant influence on the flow. If the *Ro* is large, then the rotational effects are negligible compared to the inertial forces. This happens usually in the flows where the length scales are typically small like in the mesoscale regimes. Since this thesis work is concerned with the investigation of kilometer-scale mesospheric instabilities, the effects of the Coriolis force are not considered.

As mentioned before, we are studying the dynamics of kilometer-scale instabilities having horizontal scales of a few kilometers to a few tens of kilometers in the MLT region. For these horizontal scales, the Coriolis force is small and hence can be neglected. Rewriting equation 2.47 without the Coriolis term leads to the following momentum balance equation,

$$\frac{\partial \mathbf{u}}{\partial t} + \mathbf{u} \cdot \nabla \mathbf{u} = -\frac{\nabla p}{\rho} - \mathbf{z}g + \nu \nabla^2 \mathbf{u} \tag{2.50}$$

$$\nabla \cdot \mathbf{u} = 0 \tag{2.51}$$

The thermodynamic energy equation is given by

$$\frac{\partial \theta}{\partial t} + \mathbf{u} \cdot \nabla \theta = \kappa \nabla^2 \theta \tag{2.52}$$

In the above equations **u** = (U_0+u,V_0+v,w) is the horizontal and the vertical components of the velocity respectively, U_0 and V_0 are the background winds in zonal and meridional directions, respectively, *p* is pressure, ρ is the mass density, θ is the potential temperature,ν is the kinematic viscosity, κ is the thermal diffusivity, and **g** = -*g***z** to denote the downward force of gravity. The numerical simulations done by (Seyler, 2005) did not consider the effect of dissipation when using potential temperature as a passive scalar on the bore evolution whereas this term is included in our equations (See Equation 2.52).

The divergence-free condition (2.51) allows one to write equation 2.50 in stream function-vorticity

formulation with the stream function(ψ) given by,

$$\mathbf{u} = -\mathbf{j} \times \nabla\psi,\ u = -\frac{\partial\psi}{\partial z},\ w = \frac{\partial\psi}{\partial x} \tag{2.53}$$

Upon taking the curl ($\nabla\times$) of the equation 2.50, we have,

$$\partial_t\zeta + \mathbf{u}\cdot\nabla\zeta = \partial_x(\frac{1}{\rho})\partial_z p - \partial_z(\frac{1}{\rho})\partial_x p \tag{2.54}$$

The streamfunction and vorticity are related by

$$\zeta = -(\partial_x^2 + \partial_z^2)\psi \tag{2.55}$$

where ζ is the *y* component of vorticity.

We now assume Boussinesq approximation and write the density and pressure as $\rho = \rho_0 + \rho'$, $p = p + p'$ and making use of hydrostatic pressure balance ($dp/dz = -\rho_0 g$, ρ_0 is the basic state density), we get the following relations,

$$\partial_t\nabla^2\psi + [\psi, \nabla^2\psi] = -\partial_x\theta + \nu\nabla^2\psi \tag{2.56}$$

$$\partial_t\theta + [\psi, \theta] = N^2(z)\partial_x\psi + \kappa\nabla^2\theta \tag{2.57}$$

The potential temperature is written in terms of its equilibrium state and perturbation, $\theta = \theta(z) + \theta'$. The buoyancy frequency is then given by

$$N^2(z) = -\frac{g}{\theta}\frac{d\theta}{dz} \tag{2.58}$$

and $[A, B] = \partial_x A\partial_z B - \partial_z A\partial_x B$ is the Jacobian. ν is the kinematic viscosity

The three-dimensional form of the Navier-Stokes equations under Boussinesq approximation is given below (Feraco et al., 2018),

$$\partial_t\mathbf{u} + \mathbf{u}\cdot\nabla\mathbf{u} = -\nabla p - \theta\mathbf{z} + \nu\nabla^2\mathbf{u} \tag{2.59}$$

$$\partial_t\theta + \mathbf{u}\cdot\nabla\theta = N^2 w + \kappa\nabla^2\theta \tag{2.60}$$

$$\nabla\cdot\mathbf{u} = 0 \tag{2.61}$$

2.6 Frames of reference: Lagrangian and Eulerian frame

Since fluid parcels move in a medium that might also be moving, it is important to define a particular frame of reference without which confusion can arise regarding the observation. In a Lagrangian reference frame, the evolution of the fluid parcel can be described mathematically in a frame of reference that moves with the parcel. Here some parcels will be moving faster and slower away from the observer. Eulerian frame of reference is the one in which the coordinate system is fixed to the earth. Here, the focus is on how the properties of the fluid change in time at a fixed point. These changes occur not only due to the changes in the properties of the parcel but also due to the movement of the fluid parcels of different properties past that point. The observations in both frames of reference are related through a set of mathematical relations along with the constraint that the physics should be identical. In most geophysical applications, the Eulerian frame of reference is preferred (Nappo, 2013).

Chapter 3

Atmospheric Instabilities

In this chapter

3.1 Instabilities and Turbulence 25
3.2 Bores and Solitary waves: Theory and Observation 34

3.1 Instabilities and Turbulence

"When … an infinitely small variation of the present state will alter only by an infinitely small quantity the state at some future time, the condition of the system, whether at rest or in motion, is said to be stable; but when an infinitely small variation in the present state may bring about a finite difference in the state of the system in a finite time, the condition of the system is said to be unstable."

Scientific Papers of James Clerk Maxwell, 1866.

The above quote by James Clerk Maxwell explains clearly the qualitative concept of the stability of a state or a physical system. Hydrodynamic stability concerns the stability and instability of motions of fluid due to small variations (Drazin and Reid, 2004). These unstable motions tend to evolve into an important state of motion called *turbulence* with a broad spectrum of spatial and temporal scales. The problems related to hydrodynamic stability were recognized by Herman von

Helmholtz, Lord Kelvin, Lord Rayleigh, and Osborne Reynolds. Osborne Reynolds's seminal paper in 1882 on the nature of an unstable flow in a pipe where he conducted different experiments and determined a critical parameter, the Reynolds number, that determines when the flow is laminar or turbulent, illustrates the aim of the study of hydrodynamic stability, namely, to find whether under a given condition a laminar flow is unstable and if so to determine how it breaks down into turbulence (Drazin and Reid, 2004).

In the Earth's atmosphere, instabilities are a major reason for the movement of air masses and the circulation without which the atmosphere will be in a constant state of equilibrium. Theoretical and observational studies over the years have shown that large-scale and small-scale waves alike play an important role in the transport of momentum and energy over considerable distances. For the transported momentum and energy to have a permanent effect on the background flow, these motions must undergo breaking and dissipation (Fritts, 1984; Fritts and Rastogi, 1985). The mechanisms that are thought to contribute the most to the dissipation of these dominant wave motions are dynamical and convective instabilities. Convective instability happens when the warm air rises resulting in thermal mixing with the surrounding air leading to the development of clouds and convective storms. Dynamic instability is produced through the horizontal movement of air and the physical forces that act on it like the Coriolis force, pressure gradient force, and buoyancy force. Due to the scales at which they occur, these instabilities result in considerable turbulence throughout the atmosphere which in turn is expected to play a significant role in the vertical transport of heat and other atmospheric constituents (Feraco et al., 2018).

While decades of observational evidence have revealed the importance of these small-scale instabilities near the planetary boundary layer, due to observing limitations, only recently progress has been made in the MLT region (Lehmacher et al., 2007; Chau et al., 2020; Mesquita et al., 2020; Hysell and Larsen, 2021; Bui et al., 2023). Combined with the high-resolution direct numerical simulation (DNS), modeling studies have confirmed the pervasiveness of these instabilities in the multi-scale flows and their potential importance in the energy dissipation and turbulent mixing (Fritts et al., 2014; Fritts et al., 2018; Feraco et al., 2018; Dong et al., 2021; Bui et al., 2023). These turbulent processes and the small-scale instabilities generated by the breaking of waves, dissipation, and mixing also play an important role in the energy budget of the MLT, as they transport momentum and energy between different layers of the atmosphere. Quantifying the impact of these instabilities is essential for achieving a comprehensive understanding of the various dynamic processes at play.

Chau et al. (2021) reported a peculiar event that was observed in the PMSE layers between 80 and 90 km wherein the layers were pushed up and down with vertical velocities of around 60 m/s and

40 m/s in the up and downdrafts, respectively (See Figure 1.3). They reported that this observation of extreme vertical drafts resembles, morphologically, a solitary wave or an undular mesospheric bore oscillating in a varicose mode similar to other observations (Fritts et al., 2020). The vertical scale of their event is more than two times larger than what has been previously observed regarding bores or solitary waves. Feraco et al. (2018) ran a series of DNS in a highly stratified environment of low Froude number (Fr $\sim 0.1 - 0.01$) and high Reynolds number and predicted the relatively frequent occurrence of these extreme vertical drafts localized in space and time due to resonant interaction between GWs and turbulent motions. Hence, in addition to the conventional instabilities like the KH instability, Ekman layer instability, etc., the above-mentioned small-scale instabilities accompanied by extreme vertical velocities may also play an important role in the MLT dynamics than previously thought.

Below we give a brief introduction to some of the commonly observed instabilities in the MLT.

3.1.1 Kelvin-Helmholtz Instability

Kelvin-Helmholtz instability is a fluid instability that occurs due to shear in the velocity of a continuous fluid or at the interface between two fluids. This problem was first studied experimentally by Herman von Helmholtz and a mathematical problem was first posed and solved by Lord Kelvin. For atmospheric turbulence to be maintained, the inertial forces need to overcome the static stability that arises when heavier air is beneath the lighter air. If such a condition remains throughout, then the atmosphere will be at rest and no motions will take place. Suppose a basic incompressible flow with an inviscid fluid of variable density having a velocity $U(z)$ and density $\rho(z)$, where z is the height. In such a flow, the essential mechanism of instability is the conversion of available potential energy to kinetic energy overcoming the buoyancy effects thereby resulting in the velocity shear to destabilize the flow. Figure 3.1 shows the velocity profile of a stratified system where the fluid is flowing in opposite directions. This system is perturbed with a small amplitude sinusoidal disturbance that leads to the onset of the instability as shown in Figure 3.2. In the atmosphere, this kind of motion can be routinely observed as a result of the interaction of waves of different scales, from the planetary waves at larger scales to gravity waves at smaller scales (Fritts and Alexander, 2003; Fritts et al., 2014). This interaction of superposition among the waves can initiate instabilities like the Kelvin-Helmholtz instability that accounts for dissipation, generation of turbulence, and mixing (Baumgarten and Fritts, 2014; Kjellstrand et al., 2022; Fritts et al., 2023). Spatially and temporally localized instabilities can lead to sporadic and patchy turbulence and mixing due to the localized deposition of energy and momentum (Feraco et al., 2018;

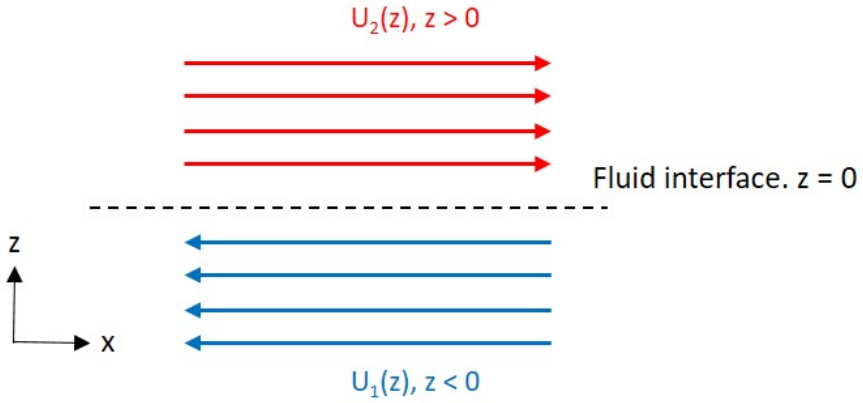


Figure 3.1: Schematic of the background velocity profile for Kelvin-Helmholtz instability

Feraco et al., 2021). These have significant effects on the large-scale motions thereby influencing the circulation in the atmosphere.

The non-dimensional number that controls the onset of the Kelvin-Helmholtz instability is the Richardson number which can be defined as the ratio of the buoyancy term to the flow shear term and is given by,

$$Ri = \frac{g}{\rho} \frac{\partial \rho / \partial z}{(\partial u / \partial z)^2} \tag{3.1}$$

where g is gravity, ρ is the density, u is the flow velocity and z is height.

If the Richardson number is much less than unity, then the buoyancy term is small and becomes unimportant in the flow. This means that the inertial forces are stronger leading to overturning of the flow and the onset of the instability. On the contrary, if this value is much greater than unity, then the buoyancy effects are dominant, and hence the kinetic energy that is needed to overturn the flow and homogenize the fluids is not sufficient. The value of $Ri < 1/4$ is a necessary condition for the velocity shear to overcome the tendency of the stratified fluid to remain stratified and the turbulent mixing to occur.

The Kelvin–Helmholtz instability manifests within the atmosphere as an intermittent yet widespread occurrence (Fritts et al., 2023). However, our understanding of the spatial and temporal dimensions in which these dynamics transpire remains limited. This is primarily attributed to the scarcity of observational resources and the relatively recent advancement of modeling techniques capable

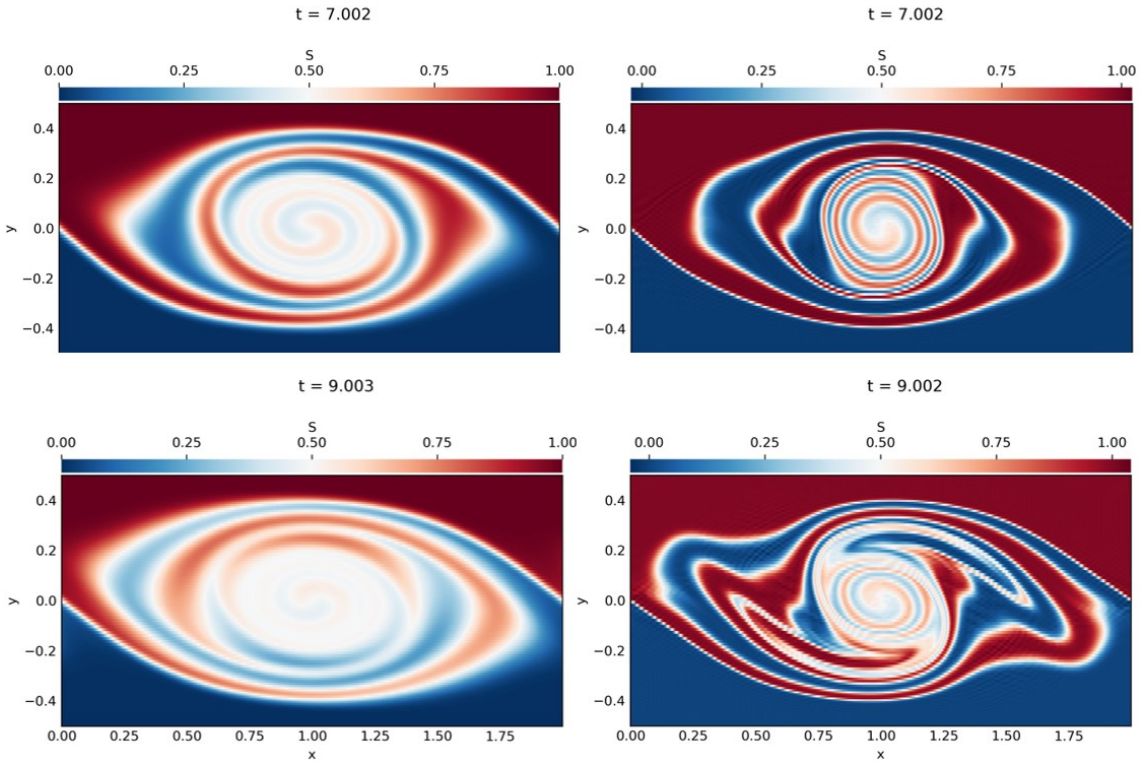


Figure 3.2: Time evolution of Kelvin-Helmholtz instability from high resolution (512×512) direct numerical simulations for a (Left) Reynolds number of 1000, (Right) Reynolds number of 5000

of tackling extensive, multiscale challenges at sufficiently elevated Reynolds numbers. However, in recent years the capabilities of ground-based observations have vastly improved and the small-scale GWs and instability dynamics can be studied more thoroughly due to the advances in the measurement techniques (Chau et al., 2020; Hysell and Larsen, 2021). Recent MLT observations reveal the widespread occurrence of large-scale KHI that may contribute to significant turbulence and mixing in the MLT, but which has not been investigated, nor accounted for, in large-scale modeling of the MLT to date. These observations include the ones from radars, lidars, PMC imagers, airglow imagers, and satellites (Baumgarten and Fritts, 2014; Chau et al., 2020; Fritts et al., 2018). Chau et al. (2020) reported the first-ever observation of a KHI event in time and three dimensions utilizing a novel radar volumetric imaging (Urco et al., 2019) thereby revealing irregular KH billows having horizontal wavelengths of $\sim$ 8 km at 85 km. This event had the characteristics of weak stratification (Froude number $\sim$ 1) and strong turbulence (Re $\approx$ 25000) In addition to the primary KH overturning billows, structures resembling striations of 2 km were reported in the direction transverse to the propagation direction. They identify these transverse structures as secondary billows that were reported in direct numerical simulations (Fritts et al., 2014). Hysell and Larsen (2021) reported similar structures in the lower thermosphere where the reported

secondary billows were helical in structure and aided in the mixing and diffusion. These types of small-scale multidimensional observational capabilities and state-of-the-art numerical simulations will enable complete quantification of small-scale dynamics and better parameterization in large-scale general circulation atmospheric models (Chau et al., 2020).

Mathematical treatment of Kelvin-Helmholtz Instability

Here we give a mathematical treatment to the instability by deriving the dispersion relation (Vallis, 2017). Let us consider two fluid masses of equal density flowing with two velocities, U_1 and U_2 in x-direction as shown in Figure 3.1 separated by a common surface, $z = 0$. What will happen to this flow when it is perturbed slightly? If the amplitude of the initial perturbation is small, after the onset of the instability, we can neglect the nonlinear interactions in the governing equation since these are the squares of small quantities. Then the Euler equations satisfy the perturbation for $z > 0$ as follows

$$\frac{\partial \mathbf{u}'}{\partial t} + U\,\frac{\partial \mathbf{u}'}{\partial x} = -\nabla p' \tag{3.2}$$

$$\nabla \cdot \mathbf{u}' = 0. \tag{3.3}$$

We can write a similar equation for $z < 0$ with the velocity being $-U$. We can assume periodic boundary conditions in x-direction, the perturbations can be represented as Fourier series expansion of the form

$$\phi'(x, z, t) = Re \sum_k \phi_k(z, t) e^{ikx} \tag{3.4}$$

where ϕ is any field variable like the pressure or velocity. Considering the z-component of 3.2 for the dispersion relation

$$\frac{\partial w'}{\partial t} + U\,\frac{\partial w'}{\partial z} = -\frac{\partial p'}{\partial z} \tag{3.5}$$

The perturbations are of form $w' = w\, e^{(ikx+\sigma t)}$ and $p' = p\, e^{(ikx-kz)}e^{\sigma t}$.

$$(\sigma + ikU)w = k\, p \tag{3.6}$$

The time dependence of the instability is given by the term $e^{\sigma t}$. The growth rate σ is complex; if it is a positive real component, then the perturbation will grow leading to instability. If σ is a non-zero imaginary component, then there will be oscillatory motion. The vertical velocity at the interface of the two fluids, $z = 0$ is the rate of change of displacement η due to the given perturbation.

$$w = \frac{\partial \eta}{\partial t} + U\,\frac{\partial \eta}{\partial x} \tag{3.7}$$

$$w = (\sigma + ikU)\eta, \tag{3.8}$$

where η is the displacement at the interface. Substituting 3.8 into 3.6 gives

$$(\sigma + ikU)^2\eta = k\, p. \tag{3.9}$$

The above equations are for the flow at $z > 0$. Using similar reasoning, for $z < 0$ we have

$$(\sigma - ikU)^2\eta = k\, p. \tag{3.10}$$

Combining equations 3.9 and 3.10, we get,

$$\sigma^2 = k^2U^2 \tag{3.11}$$

Equation 3.11 has two roots. If the root is positive then the amplitude of the perturbation grows exponentially like $e^{\sigma t}$ and the flow is said to be *unstable*.

3.1.2 Ekman instability

Ekman instability is a type of surface instability that has been observed predominantly in the ocean where a layer of fluid is under a force balance between pressure gradient force, Coriolis force, and friction. The result of this force balance is called the Ekman spiral which is illustrated in Figure 3.3. Imagine wind blowing over a free surface of water. Due to the action of the wind, some of its energy will be transported to the water's surface, and associated friction caused by this will move the water as well. This results in what is called the surface currents in the ocean. Some of the energy then gets transferred to deeper layers of the fluid causing the adjacent layers to move too. Two things happen here: 1) Due to friction the speed diminishes with depth, and 2) As the movement is transferred deeper, the Coriolis force acts to deflect each layer to the right of the one above it causing a spiral pattern called the Ekman spiral.

The hydrodynamic stability of the Ekman layer adjacent to a rigid surface has been investigated over the years starting with the work of Lilly (1966). The theoretical explanations put forth by Lily confirmed two types of Ekamn instability, namely *type-1* and *type-2* instabilities. Type-1 instability is an inflection point instability in an inviscid flow while type-2 is a traveling wave viscous type instability. The critical Reynolds number that predicts the onset of the instability is lower for type-2 than for type-1. The aforementioned shear instability like the KHI is a special case of

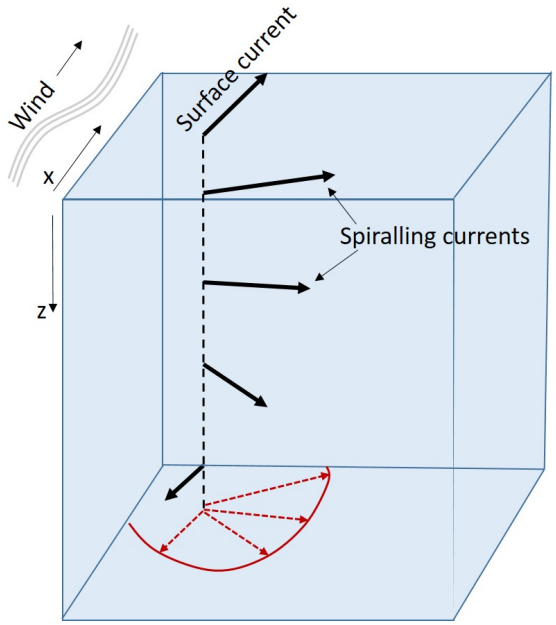


Figure 3.3: Schematic diagram to illustrate the Ekman Spiral in a column of fluid. The black solid arrows indicate the direction of the flow at each layer of the column. The red dotted arrows at the bottom of the column indicate the projection of the formed spiral

turning point instability where in addition to wind shear, the rotation plays an important role in the onset of the instability. Ekman spiral is considered a useful prototype to characterize flows with wind shears and the subsequent formation of banded structures or rolls that have been frequently observed in the MLT region (Allen and Bridges, 2003; Dubos et al., 2008; Bui et al., 2023). Bui et al. (2023) recently reported a series of radar observations of small-scale bands or braid-like structures in the E-region of Earth's atmosphere which is between 95-150 km. They also reported secondary banded structures oriented normally to primary waves which is a consequence of the turning shears acting on the primary waves. With the recent advances in coherent radar scattering techniques, many small-scale structures are being resolved with a higher degree of accuracy thereby prompting investigations into these often overlooked small-scale instabilities (Hysell and Larsen, 2021).

3.1.3 Rayleigh-Benard instability

Rayleigh-Benard instability or Rayleigh-Benard convection is the movement of fluid that is confined between two thermal layers and is heated from below to produce a temperature difference that results in the transfer of energy between the upper and lower layers due to the temperature

gradient. This results in the formation of convection rolls which allow for efficient energy transport between the different layers as shown in Figure 3.4. An important parameter that is associated with the convection is the Rayleigh number which is the ratio time scale for the diffusive thermal transport to the time scale for convective thermal transport. The critical value of Rayleigh number demarcates the fluid regime as being characterized by conduction or convection. Below the critical Rayleigh number, there is no fluid motion and the transfer of heat is solely through conduction while above it convective motions set in leading to turbulent flow. The study of the convective instability in the middle atmosphere began with the observations of unstable lapse rates in the MLT region (Fritts and Rastogi, 1985). Hines (1960) suggested that the gravity waves that are generated in the lower atmosphere propagate upwards resulting in such observed fluctuations. These GW motions would achieve large amplitudes in the MLT altitudes and likely result

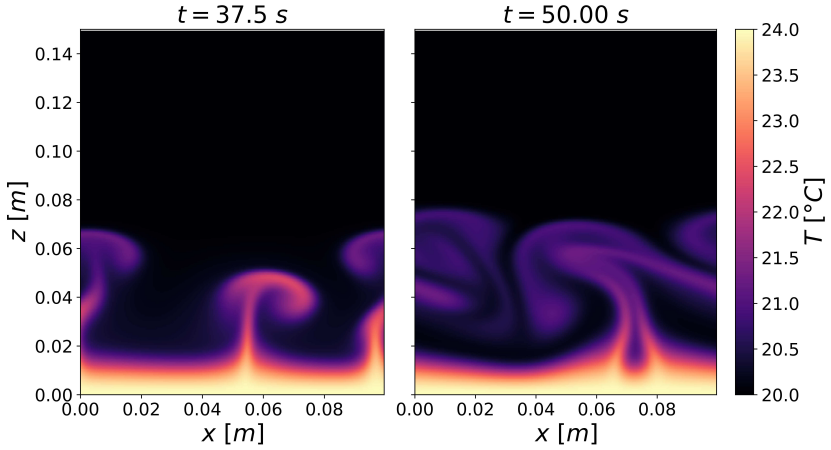


Figure 3.4: Time evolution of Rayleigh-Benard instability in a highly stratified fluid from high resolution (512×512) DNS.

in turbulence and energy cascade to smaller scales. Due to the complexity involving these fine-structure convective instabilities, the studies that have contributed most to our understanding of these processes have involved laboratory experiments (McEwan, 1971; McEwan, 1973), where several internal waves were superposed to produce regions of instability that may be representative of their dynamics in the middle atmosphere. These instabilities occur on large vertical scales typically with layer depths of 3-10 km compared to KHI suggesting that they must provide a high level of dissipation in order to offset the amplitude growth with height. More often the dynamics that lead to the formation of dynamical instabilities can lead to subsequent convective instabilities due to the breaking that accompanies the former. Hence what emerges is a complex system of two or more instabilities interacting and driving the dynamics of the middle atmosphere.

3.2 Bores and Solitary waves: Theory and Observation

A tidal bore, sometimes also known as aegir or eagre, is a series of large wave crests that travel upstream into a river or estuary as a result of a surge in the tides. The occurrences of bores have been extensively investigated for over a century starting with the seminal paper on tidal bores by Rayleigh (1908) and others (Lighthill, 1978). Lighthill (1978) provided a good theoretical description of open-channel bores which was later used to characterize the types of bores such as undular bores and turbulent bores. Examples of such occurrences have been well-noted in the past like the famous Severn River bore in the UK, shown in Figure 3.5 and the Hangzhou bore on the Qiantang River in China (Lighthill, 1978). Bores are also known to occur in the lower troposphere, the most famous example being the "morning glory" traveling wave-cloud system in northern Australia (Smith, 1988).

The observation of undular bores in the mesosphere has only been recently reported by Taylor et al. (1995) and Swenson and Espy (1995) who reported "wall" waves that exhibited apparent features that resembled an undular bore, but which were previously undocumented in the MLT. These observations generated significant interest in mesospheric bores that continue to the present. The observation of bores, as reported by Taylor et al. (1995), was identified as such by Dewan and Picard (1998) who developed a simple linear model for the bore propagation in the mesosphere and estimated several parameters. They based their linear model on the two-layer shallow water theory following Rayleigh (1908). The analysis of Dewan and Picard (1998) led to the estimation and relation among several bore parameters like the bore wavelength, amplitude, phase speed, and energy dissipation rate. Their follow-up paper(Dewan and Picard, 2001) suggested the interaction of gravity wave critical level layer with the mean flow as a possible cause for the formation of mesospheric bores, with both the bore and the inversion layer, that serves as a waveguide for the bore propagation, to have the same source. They showed that when the horizontal phase velocity of a gravity wave and the total background wind (including the mean wind plus the tidal component) are equal (i.e. at a critical layer), the resulting interaction between the wind and wave, combined with nonlinear effects, accelerates the fluid and acts as a piston, driving bore formation.Fritts et al. (2018) recently demonstrated a strong local deposition of momentum and the ensuing interaction with the mean flow of a large amplitude GW encountering a mesospheric inversion layer. Studies by Walterscheid et al. (1999), Snively and Pasko (2003), Snively and Pasko (2008), and Fritts et al. (2018) demonstrated the trapping and or reflection of GWs upon impinging on a thermal or a velocity duct that may exhibit instabilities, secondary GWs, and partial transmission or reflection depending on the duct and GW parameters.



Figure 3.5: Left: Tidal bore in the Severn river in the UK. Right: Turbulent tidal bore in Qiantang River in China. Images taken from *https://noc.ac.uk*

Mesospheric bores are non-linear responses that cause GW amplification, due to trapping in ducts (Fritts et al., 2018). In the case of bores in rivers, this duct can be in the form of a channel that acts as a boundary for the bore to propagate. However since the atmosphere is an open system, such bounded domains cannot be easily found. This raises an interesting question as to how bounded ducts occur in the atmosphere. The linear model of Dewan and Picard (1998) proposes that this duct or channel in the atmosphere is formed as a consequence of strong inversion layers, with localized high atmospheric stability, N^2, where N is buoyancy frequency. Ducts can also be formed due to local wind maxima along the GW propagation or a combination of both, i.e. thermal and wind ducts called "dual" ducts (Chimonas and Hines, 1986). This duct can act as a wave-guide in the bore propagation, similar to channels in the case of tidal bores.

Figure 3.6 shows the undular mesospheric bore observation reported by Taylor et al. (1995) employing two airglow emissions, the O(^{1}S) or OI (557.7nm) emission, and hydroxyl (OH) emission layers. This "spectacular gravity wave event" as called by Taylor et al. (1995), shows a linear dark front advancing into a region of brightness in the O(^{1}S) emission layer at 96 km. The front was also associated with a marked change in the structure with dark wave crests and troughs following the front. On the other hand, a striking "complementary effect" was observed in the OH emission layer at an altitude of 85 km where the observation was of a bright front propagating into a field of darkness with wave crests and troughs in brightness following it and locked to it. In other words, the images in the OH layer were like "negative images" of the O(^{1}S) images. Dewan and Picard (1998) realized that there was a sudden increase in the temperature of about 40 K near 90 km. They hypothesized that this inversion layer had the characteristics needed for a region of enhanced stability producing the channel or wave-guide necessary for bore propagation. According to this hypothesis, if a horizontal wave-guiding channel is to be assumed near 90 km which aids the bore propagation, then the structures evolve such that the OH and Na (sodium) layers

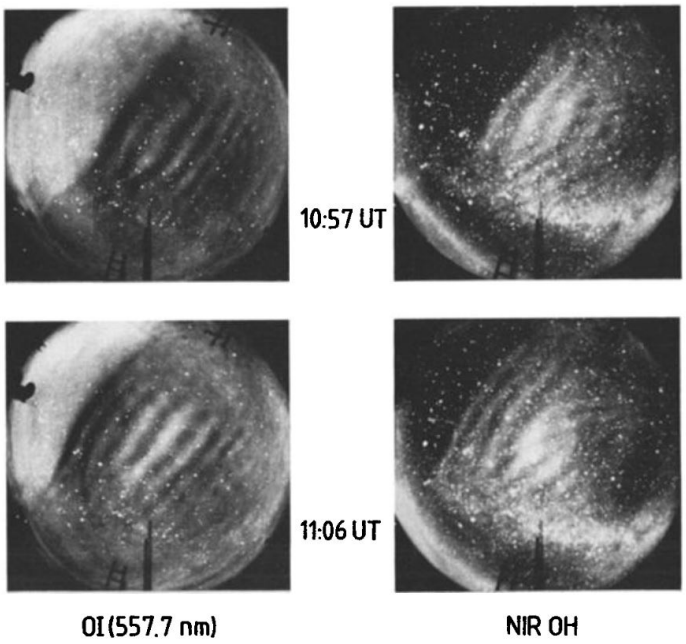


Figure 3.6: Sequence of all-sky CCD images showing the first reported observation of mesospheric undular bore. Shown on the left are images from the OI(557.7nm) emission and on the right are the airglow images from OH emission. Adapted from Taylor et al. (1995)

which are below will be depressed (pushed down so they become warmer, denser and seemingly brighter). Consequently, the emission layers above this altitude, O(^{1}S) and O_2 layers will be symmetrically pushed upward to a colder, denser region making them darker. This oscillation of the upper and surfaces 180° out of phase, when the upper part rises and the lower part descends, is called *varicose mode*. The bore and its associated waves oscillate symmetrically about the midplane of the duct.

According to the theory of Dewan and Picard (1998) and Dewan and Picard (2001), the following are the criteria devised to identify bores from regular gravity waves or wall waves (Smith et al., 2017).

- There is a frontal boundary separating the light and dark regions of airglow that propagates at 20-100 ms^{-1}.
- The bore front is accompanied by either a series of trailing waves (an undular bore) or a region of turbulence (turbulent bore).
- A thermal inversion layer must be present at the altitude of the bore in order to act as a ducting region for the bore to propagate. Wind shear may also contribute to the ducting.

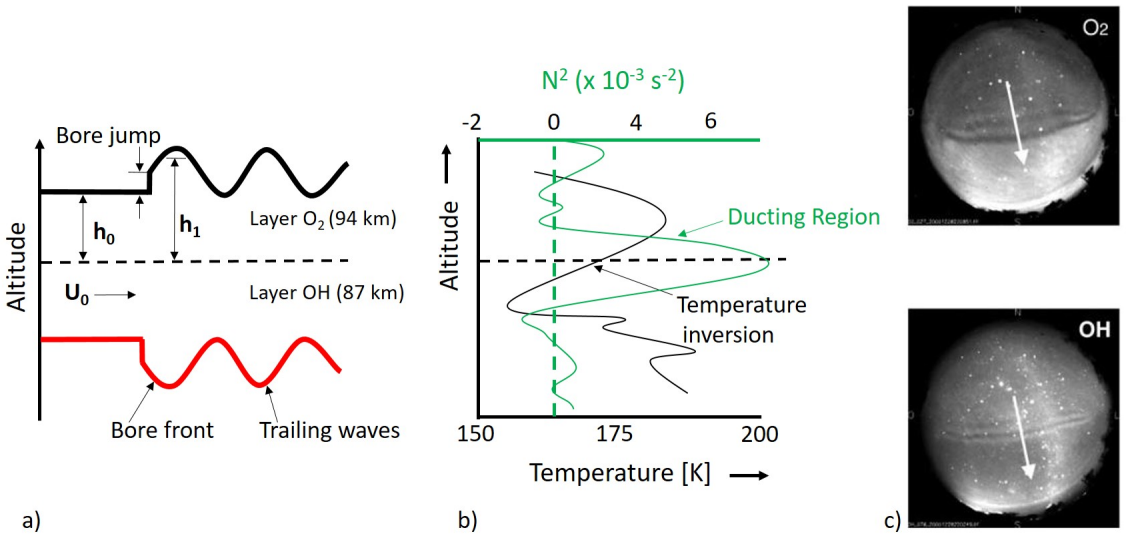


Figure 3.7: a) Schematic diagram of the oscillating duct. The dashed line indicates the center of the duct. The solid black and red colors indicate the airglow layer being pushed up and down leading to dark and bright bore, respectively. b) Sketch of the inversion layer and the associated thermal duct. c) Complementary effects observed in airglow images based on the Dewan and Picard (1998) model, O_2 layer shows a propagating dark bore and OH layer a propagating bright bore.

- Airglow emissions of the different layers will exhibit wave patterns that are either in phase or 180° out of phase with each other, depending on the relative altitudes of the layers.
- The speed and the wavelength of the bore will obey the equations 3.14-3.17 of Dewan and Picard (1998)
- The number of trailing undulations associated with the undular bore increases with time (≈2 or more eaves per hour) as the bore dissipates the energy away into the duct; assuming no energy is lost out of the duct
- The occurrence of the bore event may be associated with strong gravity wave sources.

Since the first report of the bore observation in the mesosphere by Taylor et al. (1995), numerous observations of undular bores under various conditions have been reported. These studies often employed two or more airglow emissions reported observations of dark and bright bores and provided evidence of rapid increases in the temperature confirming the initial observation of Taylor et al. (1995) and the theoretical explanation of Dewan and Picard (1998). Additional studies employing co-located ground-based measurement techniques like PMC imagers, lidars, radars, and satellite observations have deepened our understanding of the background conditions, both temperature and winds, concerning the formation and propagation of mesospheric bores (Smith

et al., 2003; Brown et al., 2004; She et al., 2004; Fechine et al., 2005; Medeiros et al., 2005; Fechine et al., 2009; Narayanan et al., 2009; Yue et al., 2010; Bageston et al., 2011; Li et al., 2013; Sarkhel et al., 2022). In recent years, interesting observations of double mesospheric bores have also been reported which are quite rare (Medeiros et al., 2016; Smith et al., 2017). There were also observations resembling "wall" waves that included enhanced temperature and *Na* column density (Swenson and Gardner, 1998; Batista et al., 2002; Li et al., 2007; Bageston et al., 2011).

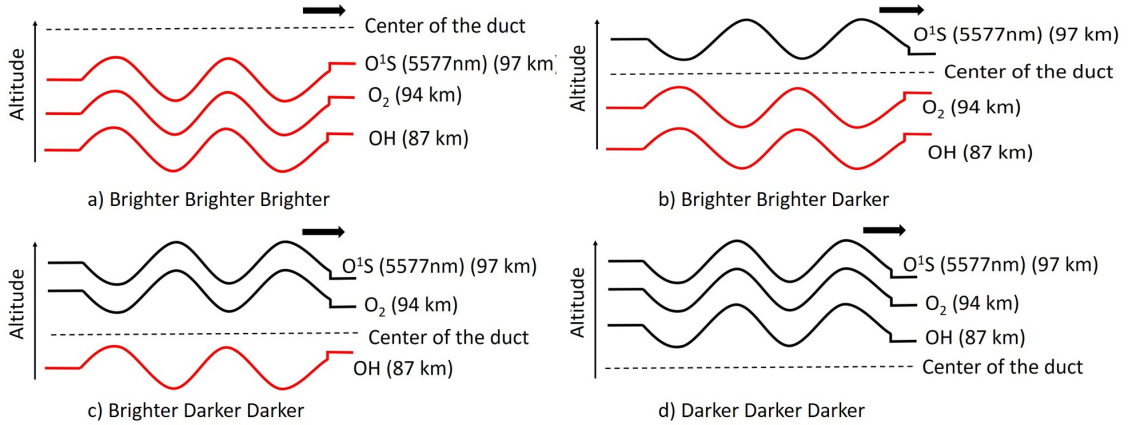


Figure 3.8: Complementary effects predicted by the linear model of Dewan and Picard (1998). Red represents the bright bore and black represents the dark bore. The solid black arrow indicates the direction of the bore propagation.

Medeiros et al. (2005) did a comprehensive study on the different responses of the OH, O_2, and the OI5577 airglow emissions to the mesospheric bore based on the theory of Dewan and Picard (1998) over equatorial Brazil between September 2000 and 2022. The results of their study are shown in Figure 3.8. If we were to assume that the nominal emission heights of the OH, O_2 and O(^{1}S) to be 87 km, 94 km, and 96 km, respectively, the model of Dewan and Picard (1998) predicts that during the bore propagation between two airglow layers, say OH and O_2, that are separated by a plane of symmetry S, the complementary effects produced are as follows: The lower layer (OH layer) is pushed down adiabatically and becomes warmer, denser, and brighter while the upper layer (O_2 layer) is pushed upward making it colder, less dense, and darker (See Figure 3.7). Using this denomination of brighter and darker bore to characterize the lowering and raising of the layers, Medeiros et al. (2005) classified the bore observations into the following four categories:

- Brighter Brighter Brighter (BBB) effect (Figure 3.8(a)) - In this case, the duct and the bore are situated above the three emission layers and are lowered as the bore propagates. A complementary, darker bore cannot be seen here.

- Brighter Brighter Darker (BBD) (Figure 3.8(b)) - In this case, the duct and the bore are located below the $O(^1S)$ layer but above the OH, O_2 layers. This means the OH and O_2 layers are pushed downward, becoming brighter while the $O(^1S)$ is pushed upward and becomes darker.
- Brighter Darker Darker (BDD) (Figure 3.8(c)) - In this case, the duct and the bore are located below the $O(^1S)$ and O_2 layers but above the OH layer. This means the OH layer is pushed downward, becoming brighter while the $O(^1S)$ and O_2 are pushed upward and become darker.
- Darker Darker Darker (DDD) (Figure 3.8(d)) - In this case, the duct and the bore are localized below the three emission layers thereby elevating the layers. A complementary, brighter bore cannot be seen here.

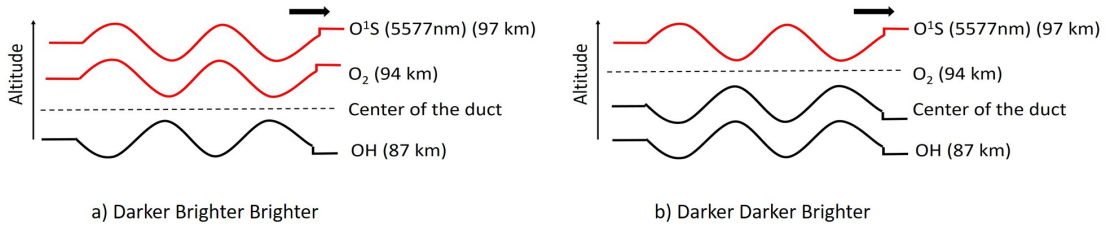


Figure 3.9: Complementary effects not predicted by the linear model of Dewan and Picard (1998). Red represents the bright bore and black represents the dark bore. The solid black arrow indicates the direction of the bore propagation.

Figures 3.9(a) and (b) are two cases of observations that show complementary effects that cannot be explained by the theory of Dewan and Picard (1998). In one case, the airglow emission layers registered a Darker Brighter Brighter (DBB) effect while in the other case, it is a Darker Darker Brighter (DDB) effect. Medeiros et al. (2005) claims that this could be explained due to the change in the emission rates of the different layers due to their sensitivity to temperature variations since an increase in the temperature results in an increase in the emission rate (García-Comas et al., 2008). If the temperature increases in the upper layer, say the O_2 layer, and decreases in the lower layer, the OH layer, then these two effects can be explained. Nevertheless, such an observation of airglow emission layers has seldom been observed and their mechanism of formation is still an open question.

Hozumi et al. (2019) investigated the geographical and seasonal variability of the mesospheric bores using the dataset spanning from September 2012 to August 2015 from the Visible and near Infrared Spectral Imager (VISI) onboard the International Space Station (ISS). They found 306

mesospheric bore events from O_2 airglow emission between 55°S and 55°N which is shown in Figure 3.10. Figures 3.10(c) and (d) show that between the months of May and July, and November and January, which are the solstice seasons, more bores are observed in the winter hemisphere during that time of the year. That is between May-July the southern hemisphere is the winter hemisphere whereas between November and January, it is the northern hemisphere. But during the equinox seasons (February-April and August-October), the occurrence rate of the bores is high for the equatorial latitudes (30°S-30°N). This indicates that the occurrence of the bores is influenced by the latitudes and seasons. The equatorial latitudes and the winter midlatitudes are also the locations of strong migrating tides that have large temperature amplitude in the MLT namely, the diurnal tides having a latitudinal peak around the equator and semidiurnal tides having a large temperature amplitude in winter midlatitudes (Forbes et al., 2008; Zhang et al., 2006; Akmaev et al., 2008). These tides with large amplitude can significantly influence the atmospheric stability leading to the formation of large amplitude inversion layers (Hauchecorne et al., 1987). One can then suppose a possible relationship between the mesospheric bores and the tidally induced inversion layers that make a favored background environment for the mesospheric bores.

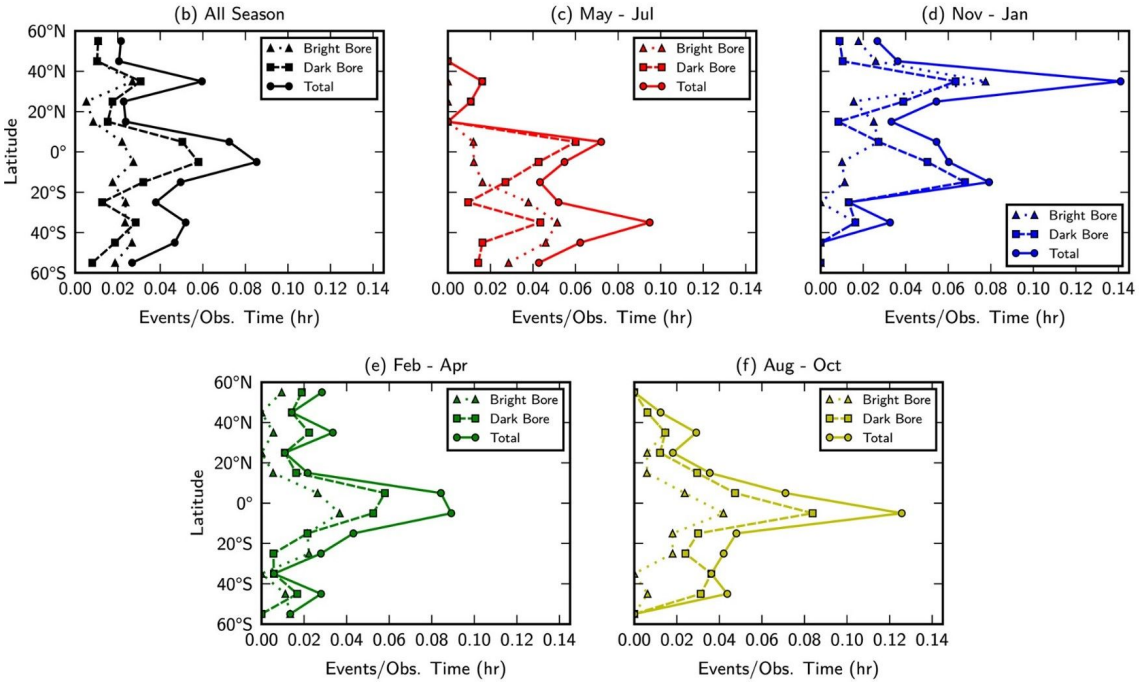


Figure 3.10: b) Distribution and occurrence of propagating mesospheric bores captured by Visible and near Infrared Spectral Imager (VISI). c)-f) Rate of occurrence of the bores as a function of latitude and seasons. Figure taken from Hozumi et al. (2019)

3.2.1 Analogy to Hydraulic Jump: A Linear model of mesospheric bores

A hydraulic jump is a phenomenon that is frequently observed in open channel flows such as rivers and estuaries which is characterized by an abrupt change in the depth of the channel fluid in response to a transition from supercritical to subcritical flow. This is analogous to the shock that is formed in a gas during the transition from subsonic to supersonic flow. Dewan and Picard (1998) observed that the airglow image data of the ALOHA-93 campaign reported by Taylor et al. (1995) resembled the sharp discontinuity of a hydraulic jump of an open channel flow. They advanced a theory akin to hydraulic jump to attribute this observed sharp front to mesospheric bores.

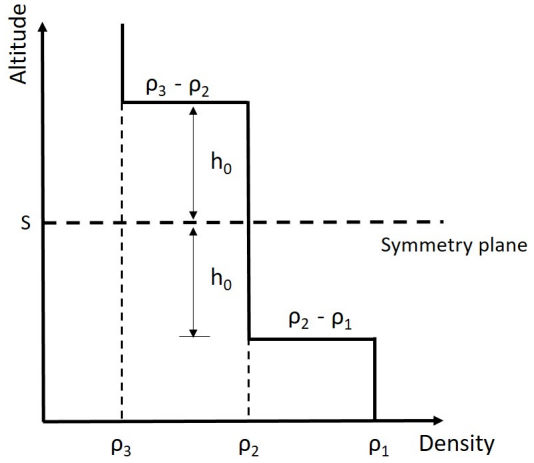


Figure 3.11: Sketch of the highly idealized density profile used by Dewan and Picard (1998).

Figure 3.11 shows a very simplified profile of density used by Dewan and Picard (1998) which they claim is the simplest guiding structure that can support an internal bore. There are three density layers, with ρ_1 and ρ_3 being semi-infinite layers and ρ_2 having a finite thickness $2h_0$. Dewan and Picard (1998) put forth the argument that any perturbation in the upper layer $\rho_3 - \rho_2$ will be mirrored in the $\rho_2 - \rho_1$ layer about the place of symmetry, assuming that there are no vertical motions inside the layer. Dewan and Picard (1998) stated that the equations governing the open channel bores will also hold for this simple model if the acceleration due to gravity g, is replaced by buoyant acceleration g' given by the following expression,

$$g' = g\frac{\rho_2 - \rho_1}{\rho_2} = g\frac{\theta_2 - \theta_1}{\bar{\theta}}, \tag{3.12}$$

where θ is the potential temperature which is commonly used instead of density in atmospheric

physics. The equation of motion for the bore velocity,*U* is then,

$$U^2 = \frac{1}{2}g'(h_0 + h_1)\frac{h_1}{h_0}, \tag{3.13}$$

where h_0 is the undisturbed height of the fluid, h_1 is the perturbed height of the fluid as the result of the bore and g' is the reduced gravity. Lighthill (1978) used laboratory experiments to show that, for an undular bore, the bore strength, β, defined as the normalized bore amplitude, is given by the expression:

$$\beta = \frac{h_1 - h_0}{h_0} \leq 0.3. \tag{3.14}$$

When this value exceeds the upper bound of 0.3, breaking occurs and turbulent bores with no trailing waves result (Rayleigh, 1908; Lighthill, 1978). For weak bores, where $\beta \ll 1.0$, the waves behind the discontinuity are predominantly sinusoidal, as seen in mesospheric undular bores (Lighthill, 1978). The wavelength of the waves behind the bore is given by,

$$\lambda = \frac{2\pi h_1}{3}\sqrt{\frac{2h_0}{h1 - h0}}. \tag{3.15}$$

The amplitude *a*, of the displacement about the perturbed height, h_1 for the waves behind the bore can be approximated by,

$$a = \frac{1}{\sqrt{3}}\frac{h_1}{h_0}(h_1 - h_0). \tag{3.16}$$

The rate of dissipation of the wave energy, *D* and the amount of energy per wave crest,*E* are given by,

$$D = \frac{\rho U g(h_1 - h_0)^3}{4h_1}.E = \frac{1}{2}\rho g a^2 \lambda. \tag{3.17}$$

With the above equation, one can estimate the number of trailing waves behind the bore.

Chapter 4

Observation techniques to study atmospheric instabilities in the MLT

In this chapter

4.1 Tools to study kilometer-scale instabilities: Airglow imagers and Satellites 43
4.2 Using Noctilucent clouds to study atmospheric dynamics 45
4.3 Observing Polar Summer Mesospheric Echoes (PMSE) using MAARSY 47

4.1 Tools to study kilometer-scale instabilities: Airglow imagers and Satellites

Airglow is a faint emission of light by a planetary atmosphere and is defined as an emission of light by atoms and molecules excited through chemical processes in the atmosphere as shown in Figure 4.1. It is frequently observed in the low and middle-latitude regions. The atoms or molecules will get excited when they receive solar energy and after some time will come back to their ground state resulting in the emission of excess energy in the form of photons. The lifetime of these processes is different for different species and is height-dependent. Due to the high collision frequency

in the lower atmosphere, emission detection is not always possible. However, with altitude, the collision frequencies decrease and hence the airglow emissions are predominant above 80 km. Airglow emissions have been used for many years as a tracer to study atmospheric wave dynamics by measuring the changes in the intensity of the emissions as a consequence of wave propagation. Moreover, the airglow imaging technique is widely used to directly estimate wave characteristics like the wavelength, phase speed, periodicity, and propagation direction (Ramachandran et al., 2023). There are several airglow emissions like the OH Meinel band, O_2 atmospheric band, Na

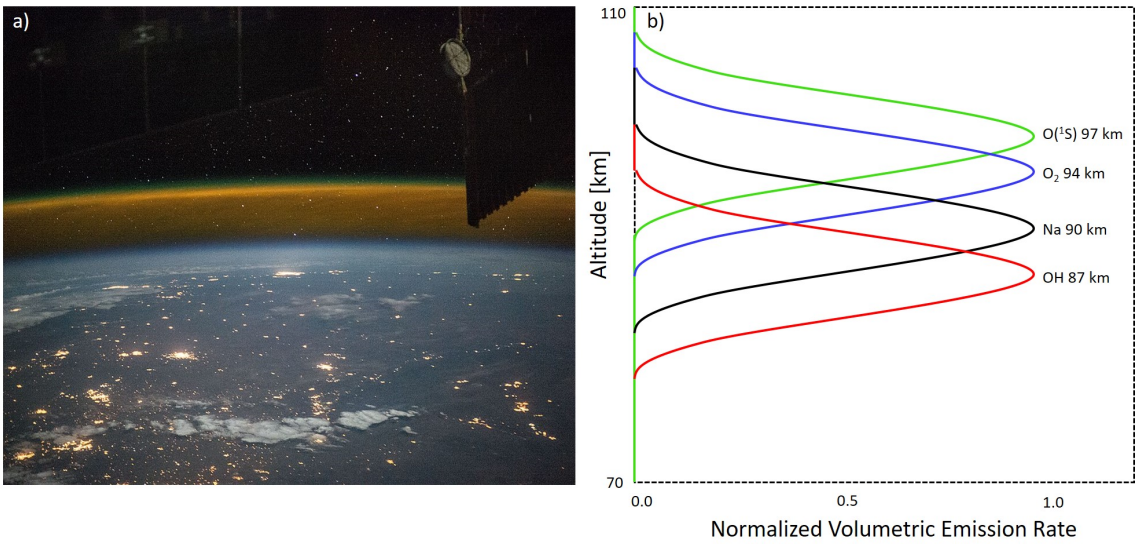


Figure 4.1: (a) Airglow as viewed from the International Space Station. The altitude of this emission is between the mesosphere and thermosphere. Image taken from *https://eol.jsc.nasa.gov* (b) A sketch of different mesospheric airglow layers and their peak emission altitudes.

and $O(^1S)$ which can be monitored from ground-based as well as space-borne instruments. The hydroxyl (OH) emissions arise in the mesosphere having a peak emission altitude of around 87 km, OH emissions are mainly associated with infrared wavelength in the range of 700-4500 nm and are considered one of the most intense emissions in the Earth's atmosphere (Martinis et al., 2018). The molecular oxygen (O_2) has a peak emission altitude of around 90 km with a range of altitudes between 90 and 100 km. One of the major species of airglow emissions is the atomic oxygen ($O(^1S)$) which emits radiation by various processes in the middle and upper atmosphere.

The multi-wavelength all-sky imager (ASI) installed by Boston University and operated by IAP in Kühlungsborn (54.12°N; 11.77°E) has six filters enabling the observation of different MLT altitudes. The present study uses two narrow-band filters to observe night-glow emissions in the MLT at wavelengths of 557.7 nm ($O(^1S)$ green line) and 864.5 nm (O_2 emission), and a broadband OH emission filter with a spectral range of 695–1,050 nm.

Remote-sensing of the observations is accomplished not only by ground-based instruments but also through satellite observations. The Sounding of the Atmosphere using Broadband Emission Radiometry (SABER) instrument is one of four instruments on NASA's TIMED (Thermosphere Ionosphere Mesosphere Energetics Dynamics) satellite. These measurements are used to provide vertical profiles of kinetic temperature, pressure, geopotential height, and volume mixing ratios for the different trace species. The ambient kinetic temperature retrieval at a particular altitude is accomplished using the 15 μm emission from CO_2 molecules in the atmosphere assuming the local and non-local thermodynamic equilibrium conditions (García-Comas et al., 2008). The uncertainty in retrieved SABER temperature in the MLT region is around 4–5 K with a vertical resolution of 2 km. By measuring the above-mentioned parameters, we can characterize the background conditions that make the environment conducive for kilometer-scale instabilities. Another instrument is the Visible and Near Infrared Spectral Imager (VISI) onboard the International Space Station (ISS). Hozumi et al. (2019) used this data from this instrument to characterize around 300 bore events based on seasonal and geographical variability. Both SABER and VISI can do observations across different filters of the airglow like the OH Meinal band (730 nm), the O_2(762 nm), and the OI band (630 nm). A multi-instrument approach to studying the MLT region is important to understand the dynamics of kilometer-scale dynamics

4.2 Using Noctilucent clouds to study atmospheric dynamics

Noctilucent Clouds (NLCs) are ice-related phenomena that occur in the middle latitude summer mesopause region and in the polar regions (Gerding et al., 2021). They are known to be the highest clouds in the Earth's atmosphere and have been used as tracers to study dynamics and instabilities in the MLT (Baumgarten and Fritts, 2014). While lidars have been used to detect the NLC observation, human eye or automated Charge-Couple Device (CCD) cameras are mainly possible at middle latitudes of around 60° latitude. The NLC studies are done, these days, mostly using satellites, lidars at high and middle latitudes (Gerding et al., 2021), or cameras (Baumgarten and Fritts, 2014). NLCs provide an alternate viewing of small-scale dynamics which are constrained by large vertical averaging of airglow intensities or temperature over the depth of an airglow layer (Baumgarten and Fritts, 2014). The optical layer thickness is usually around 1 km thick at full width at half maximum (FWHM). The fundamental difference between the airglow and the NLC observations is that the vertical weighting of the imaging is much smaller for NLC (FWHM $\sim$ 1km) than for airflow (FWHM $\sim$ 10km) and that the NLCs are long-lived tracers in contrast to the airglow being an instantaneous response to the local density. Baumgarten and Fritts (2014) employed NLC imaging

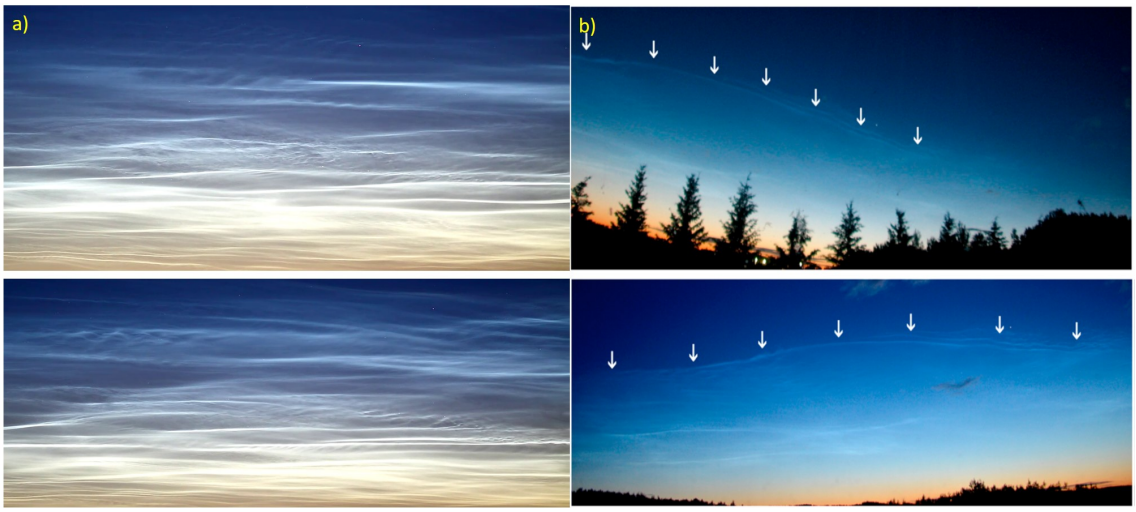


Figure 4.2: a) Snapshots of NLC exhibiting small-scale structures with an intermix of waves and turbulence. b) Mesospheric front exhibiting soliton-like behavior. The white arrows indicate the position of the soliton. Taken from Dalin et al. (2013).

from the ground using high-resolution photography to study KHI dynamics having small-scale features of around 3 to 10 km and other smaller-scale instabilities accompanying them. Dalin et al. (2013) reported the first common volume ground-based measurement of mesospheric fronts in the NLCs. Their frontal structure was represented by a nonlinear step-like disturbance resembling a soliton-like structure which is shown in Figure 4.4.

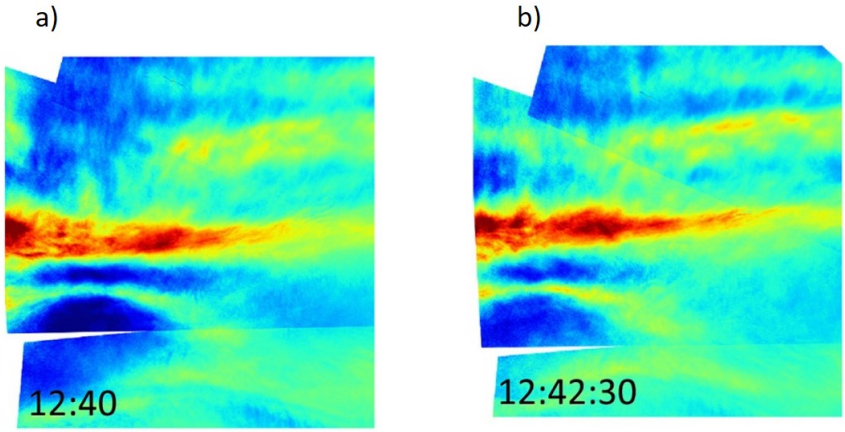


Figure 4.3: 65 × 65 km horizontal coverage of the composite FOV imaging showing the bore evolution at ∼ 82 km and propagation at a higher spatial and temporal resolution of ∼ 50 m, and 2.5 min, respectively. Figure taken from Fritts et al. (2020)

While the NLC cameras can provide comprehensive spatial and temporal information of the observed events, they still suffer from the lack of vertical information. Hence, it is important to com-

bine them with lidars from which high-resolution vertical profiles could be obtained to investigate the background dynamics. To this effect, Polar Mesospheric Cloud (PMC) Turbo imaging is one of the most commonly used techniques to study the sources and effects of instabilities and turbulence in geophysical fluids. Figure 4.3 shows one such observation that was captured in the PMC imager representing a mesospheric bore at around 82 km. The setup comprises seven PMC imagers and a Rayleigh lidar thereby overlapping large and small imager fields-of-view, along with PMC altitudes and displacements, facilitating the study of phenomena ranging from gravity wave sources at scales of up to 100 km to fine-scale turbulence at approximately 20 m. The lidar system measures the backscatter profile and vertical displacements within the PMC layer and assesses temperature perturbations caused by gravity waves in the stratosphere beneath the PMC layer. The insights provided by PMC Turbo have the potential to enhance the accuracy of modeling and deepen our comprehension of various fluid systems, including those found in oceans, lakes, other planetary atmospheres, and stellar interiors (Kjellstrand et al., 2020; Fritts et al., 2020).

4.3 Observing Polar Summer Mesospheric Echoes (PMSE) using MAARSY

Middle Atmosphere Alomar Radar System (MAARSY) is an active phase array that consists of 433 three-element cross-polarized Yagi antennas and operates at 53.5 MHz located in Andoya, Norway (69.30° N, 16.04° E) (Latteck et al., 2012; Chau et al., 2021). Polar Mesospheric Summer Echoes have been routinely observed using MAARSY since 2010 (Latteck et al., 2012). It is very well known that PMSE are very strong radar echoes produced by the presence of ice particles, turbulence, and free electrons in the mesopause at polar regions. (Rapp and Lübken, 2004). They are mainly used as tracers to understand the atmospheric dynamics (Chau et al., 2021).

In the polar summer mesopause, the conditions are ideal for the formation, and growth of ice crystals of different sizes. The occurrence of PMSE is normally between May and August. Depending on the size of these ice particles, they may be observed by the naked eye such as noctilucent clouds (NLCs) at an altitude of about 80 km which are visible to the observers at high latitudes due to their illumination by the sun (Rapp and Lübken, 2004; Baumgarten and Fritts, 2014). Much smaller ice particles exist between 80-90 km which can be transported up and down due to the presence of waves and turbulence in the mesosphere resulting in the formation of small-scale structures. This transport can lead to irregularities in the signal refractive index which is determined by the electron density at these altitudes. These irregularities can lead to radar echoes at high frequencies (VHF) as observed from the ground and are known as PMSE (Latteck et al.,

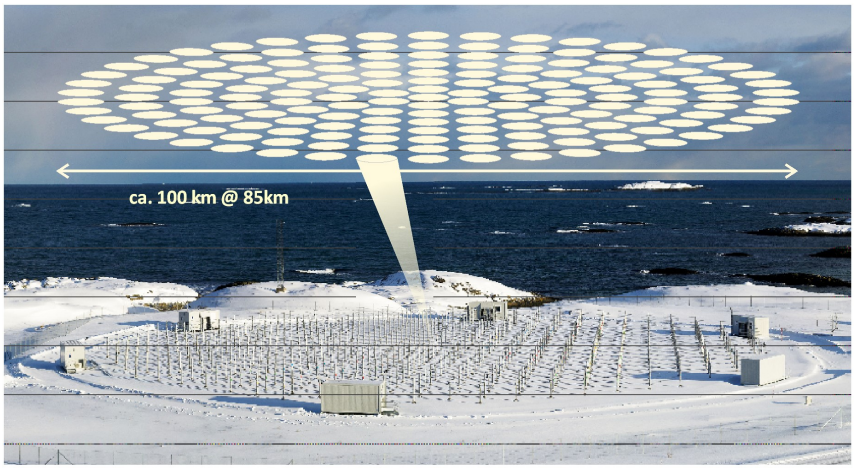


Figure 4.4: MAARSY radar system located at Andoya, Norway

2012). The use of PMSE to study mesospheric instabilities has been advanced further by integrating novel volumetric radar imaging techniques into the MAARSY radar system (Urco et al., 2019). This novel technique employs Multiple Input Multiple Output (MIMO) approach. MIMO techniques find widespread application in both the realms of telecommunications and radar remote sensing. In telecommunications, MIMO is employed to enhance both channel capacity and reliability (Urco et al., 2019). In radar applications, MIMO typically refers to a system that transmits distinct waveforms through various spatially separated transmit antennas. These signals are then reflected off radar targets and received by multiple spatially separated receiving antennas. The versatility of MIMO methods has led to their adoption in a diverse array of radar applications. This encompasses applications such as ground-penetrating radar for extracting land mine characteristics, through-the-wall imaging radar for urban remote sensing, and maritime navigation (Urco et al., 2019). From this imaging technique, we can obtain the 3D spatial information of the observed events and their temporal evolution. Compared to the airglow imagers or Lidars, which can provide only 2D information of the observations, using this new imaging technique we can obtain the full 4D information of the observations which is important for understanding the dynamics. See Figure 1.3 for examples of PMSE observations of kilometer-scale instabilities. Figures 4.5 (a) and (b) show the results of the application of MIMO for studying kilometer-scale instabilities. We can see how the usage of the MIMO technique effectively captures complex structures of the instabilities that otherwise would have been lost. The employed MIMO technique leverages time diversity, wherein one-sixth of MAARSY's complete array is temporally interleaved. During reception, 15 smaller sections, referred to as hexagons, were employed. This integration led to a receiving aperture diameter that was effectively 50% larger than in previous experiments, along with 45 effective receiving channels. The attained angular resolution is approximately 0.6° (equivalent to 0.9 km at 85 km), a marked improvement of at least 6 times compared to the multi-beam

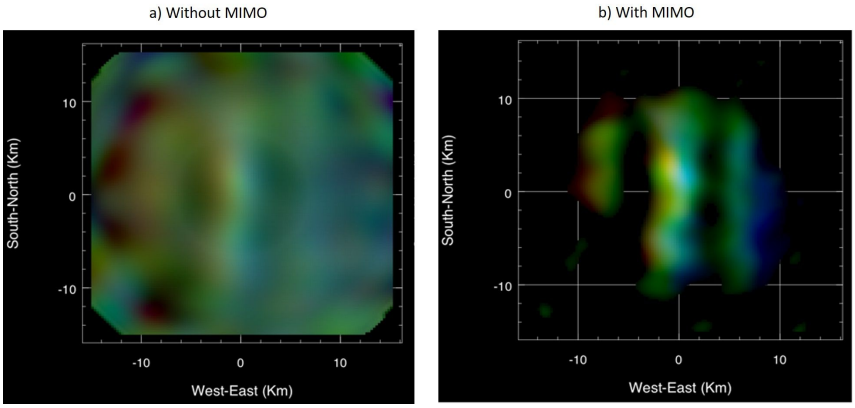


Figure 4.5: Example of the application of MIMO technique to study the KH instability.

approach at MAARSY (Urco et al., 2018; Urco et al., 2019; Chau et al., 2020).

Chapter 5

Direct Numerical Simulations for studying instabilities in the MLT

In this chapter

5.1 Direct Numerical Simulations 50
5.2 Dedalus: A Pseudo-spectral solver for solving partial differential equations 51
5.3 Simulation setup in Dedalus 52
5.4 Selection of grid resolution and basis system 53
5.5 Effects of vertical boundaries 55

5.1 Direct Numerical Simulations

A direct numerical simulation (DNS) is a simulation in which the Navier-Stokes equations are numerically solved without any parameterization or turbulence model. In DNS, all the scales of the systems are resolved with almost no numerical dissipation and thus is very useful in the context of its application to small-scale geophysical flows, especially kilometer-scale flows. Commonly, in geophysical flows, the scales of interest are large enough that the small-scale features of the

system are numerically modeled. This may lead to their effects not accurately represented in the context of energy transfer and dissipation. The characteristics of the small-scale flows can be better captured in the DNS down to the smallest scales. This opens doors to investigating small-scale instabilities in the kilometer-scale regime that require the simulation domain to be small enough to resolve all scales of motion.

Many simulation packages employ DNS for geophysical problems. Packages like FEniCS[1] and Firedrake[2] allow the users the symbolically enter the equations in variational form and use finite-element discretization for numerically solving the PDEs. Channelflow[3] uses sparse Chebyshev methods to simulate the Navier-Stokes equations which allow for invariant solutions using dynamical systems techniques. Recent packages like Chebfun[4] and ApproxFun[5] are highly flexible toolkits for approximating functions using spectral methods. Geophysical High-Order Suite for Turbulence (GHOST) is a highly scalable pseudospectral code that solves a variety of PDEs often encountered in studies of turbulent flows. It can solve compressible and incompressible hydrodynamic equations with both stratified and rotating dynamics (Feraco et al., 2018). However, the above-mentioned packages suffer from drawbacks of reduced efficiency, and restriction to solving only incompressible flows in periodic geometry, are not optimized to run on highly parallelized architectures, and are not easily optimizable codes. Dedalus bridges this gap and provides a framework applying modern, sparse spectral techniques to highly parallelized simulations of custom PDEs (Burns et al., 2020)

5.2 Dedalus: A Pseudo-spectral solver for solving partial differential equations

Dedalus is a framework for solving a broad range of partial differential equations (PDEs) using spectral methods, including initial-value, boundary-value, and generalized eigenvalue problems. A spectral method discretizes functions by expanding them over a set of basis functions. They solve the PDEs by creating a set of algebraic equations for coefficients of the truncated solution (Burns et al., 2020). Different approaches come with their advantages and disadvantages. The trigonometric polynomials of sine and cosine series are the conventional spectral bases providing

[1] https://fenicsproject.org
[2] https://www.firedrakeproject.org/
[3] http://channelflow.org/
[4] http://www.chebfun.org/
[5] https://github.com/JuliaApproximation/ApproxFun.jl

an exponential convergence to smooth functions on periodic domains. Classical orthogonal polynomials are also frequently used as spectral bases, the most common being Chebyshev polynomials with exponential convergence on finite intervals. These methods find broad application in numerical analysis and give highly accurate and efficient algorithms for manipulating functions and solving differential equations (Burns et al., 2020). Dedalus uses sparse spectral techniques in a highly parallelized environment of customized PDEs which allows users to discretize domains as a function of spectral series and specify systems of PDEs on those domains. The multidimensional fields are represented using direct products of spectral bases. The commonly used bases are Fourier, Chebyshev, Legendre, and Compound Chebyshev basis grids as shown in Figure 5.1.

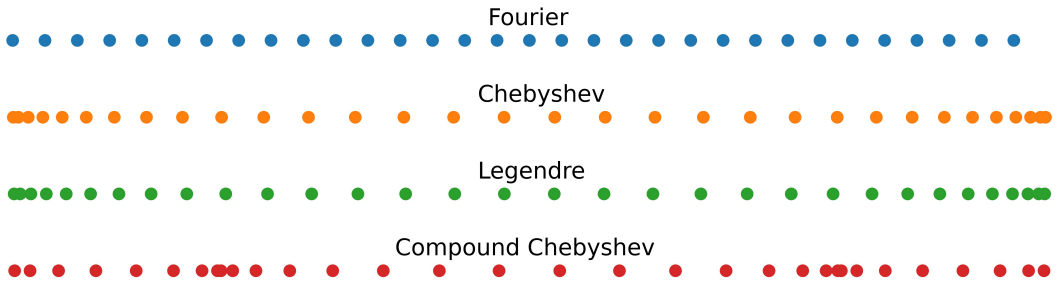


Figure 5.1: Different basis grids in Dedalus. The Fourier grid is evenly spaced. The Chebyshev and Legendre basis grids cluster near the ends of a finite interval. The Compound basis concatenates other bases on adjacent segments.

5.3 Simulation setup in Dedalus

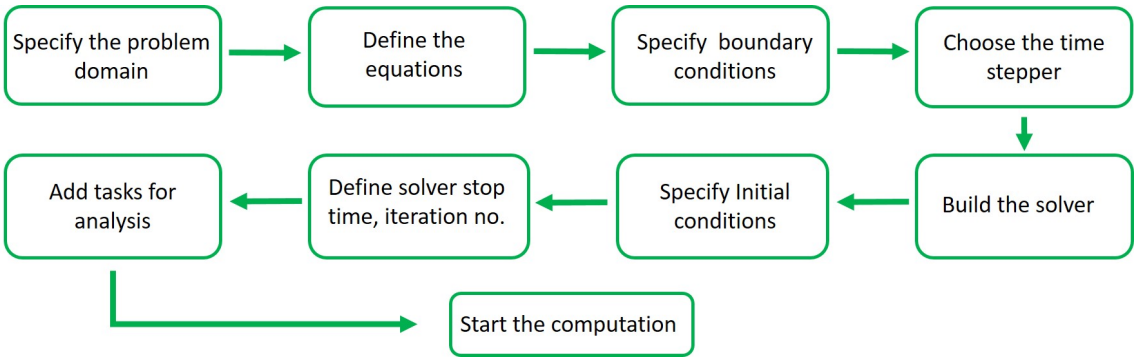


Figure 5.2: Block diagram showing the steps to set up a simulation in Dedalus.

The following points to the steps taken to set up a simulation in Dedalus.

- When simulating a problem in Dedalus, the first set is to specify the domain. The domain can be rectangular or spherical depending on the problem being studied. Domains are built by taking the direct product of bases.
- Once the problem domain is specified, we define the equations to be solved. The equations entry is symbolic text having a very easy user interface. An example of equation definition is as follows:

  problem.add equation("dt(u) + dx(p) - 1/Re(dx(dx(u)) + dy(uy)) = - u*dx(u) - v*uy")*

  The symbolic entry of the equation in Dedalus is such that the linear terms are ordered in the LHS of the equation and the nonlinear terms on the RHS. This is done so that the time stepping schemes can implicitly integrate the LHS terms and explicitly integrate the terms on the RHS thereby providing temporal stability for linear terms without the need for iterative algorithms for nonlinear terms (Burns et al., 2020).
- Next is the setting up of the right boundary conditions. If one is using Fourier basis, then boundary conditions are not needed since they indicate a periodic boundary. If, however, Chebyshev or another basis is used, the appropriate boundary conditions should be specified.
- Choosing the time-stepping scheme is important as it can affect the stability of the simulation. Dedalus uses a mixed implicit-explicit (IMEX) multi-step and Runge-Kutta time integrators for time-stepping schemes.
- Now one can set the initial conditions. For Initial value problems (IVP), initial conditions are set by directly modifying the state variable data before running a simulation.
- For IVPs, one should specify the stopping criterion of the simulation by specifying either the number of iterations or the simulation stop time.
- Dedalus has a sophisticated analysis framework in which the user specifies analysis tasks as strings. Users can output full data cubes, slices, volume averages, and more. Data is output in the hdf5 file format.
- Once the above steps are thoroughly verified, the simulation can be started.

5.4 Selection of grid resolution and basis system

Figure 5.3 shows the results of the DNS of KH instability for different grid resolutions. The grid G1024 is the highest we employed for our simulation test and G256 is the lowest. We can see that

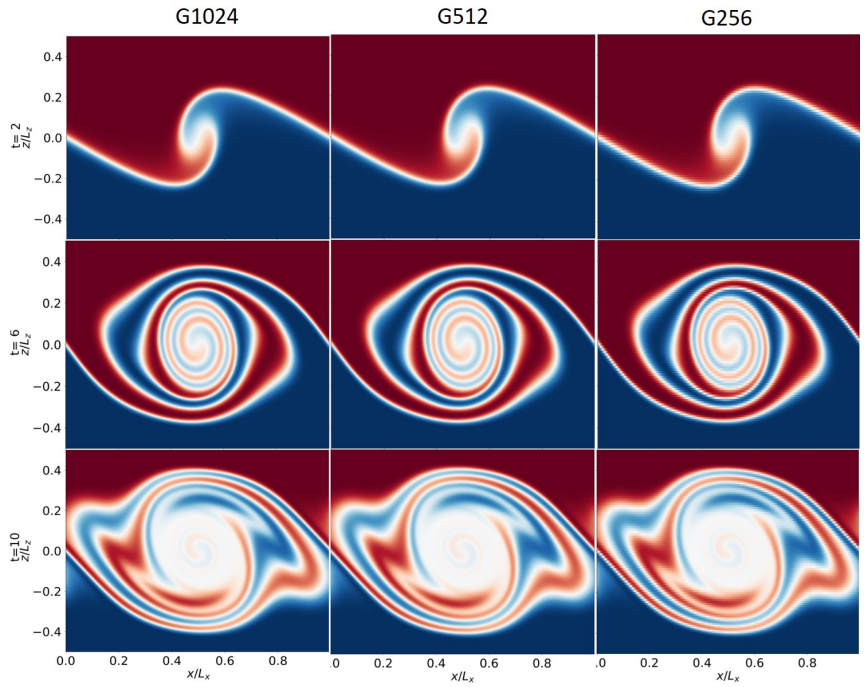


Figure 5.3: Panel plot showing the tracer evolution of KH instability for different resolutions with $\mathrm{Re} = 10^5$. All the simulations are well resolved with small differences in the lower resolution.

all the grid resolution settings qualitatively captured the evolution of KH instability to a finer degree leading to the small-scale structures being well-resolved even in the lowest grid resolution. For all the runs the CFL factor was under 0.8. The computation time taken for the G1024 to resolve the flow fully was about $\approx$ 4h in computer time compared to just $\approx$ 1h and 20 mins for G512 and G256, respectively. Hence, as a compromise between the computational cost and the stability of the simulations, we chose to use G512 for our simulations. Dedalus has been tested for its stability and convergence for many different resolutions and scaled to thousands of processors. (Burns et al., 2020; Lecoanet et al., 2015) Figure 5.4 shows the 2D flow field evolution for a double-periodic

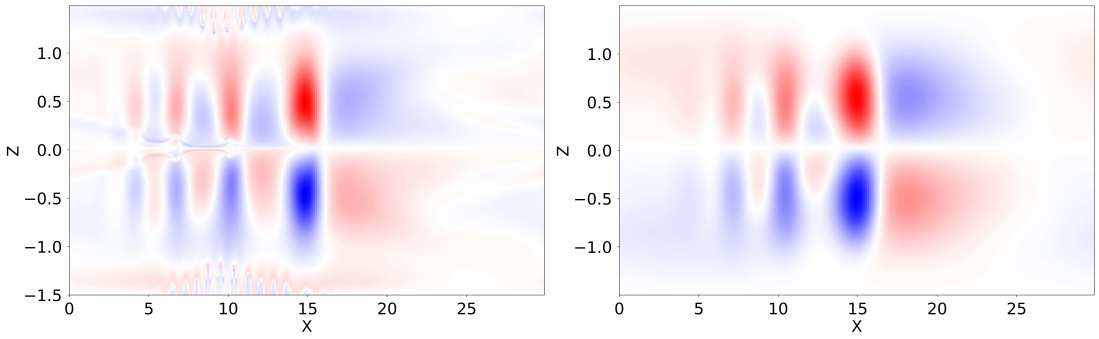


Figure 5.4: Plot showing the evolution of the flow field under (a) double Fourier domain and (b) Fourier-Chebyshev domain.

domain and a domain having periodic boundary conditions in the horizontal and rigid lid conditions in the vertical, respectively. Although the evolution of the two systems looks similar, near the upper and lower boundaries in the double periodic domain we can see the development of spurious noise which has a feedback effect on the whole flow field. Due to the periodic conditions, the flow has the chance to exit one end of the small domain and enter on the other side end thereby creating unnatural conditions that interfere with the flow evolution. At the center of the domain which demarcates the positive and negative perturbation, we can see some small-scale fluctuations which may have been due to the under-resolving of the flow by the Fourier basis. In contrast, in the domain where Chebyshev bases were employed such spurious noise was not detected with the far field boundaries, where the velocity becomes zero, acting as a sink for the flow and the flow field is well resolved. The Chebyshev basis also has the advantage of resolving the flows near the boundaries with more collocation grid points than the Fourier basis. This shows the importance of choosing the correct basis grid depending on the problem that is being studied.

5.5 Effects of vertical boundaries

Figure5.5 shows the effect vertical boundaries have on the evolution of instabilities. Figure 5.5(a) shows the evolution where the size of the vertical domain 3, which we will call a restricted domain, and the simulation domain in Figure 5.5b has a vertical dimension of 6 which will be called extended domain for simplicity. The vertical domain has rigid lid boundary conditions. Both sim-

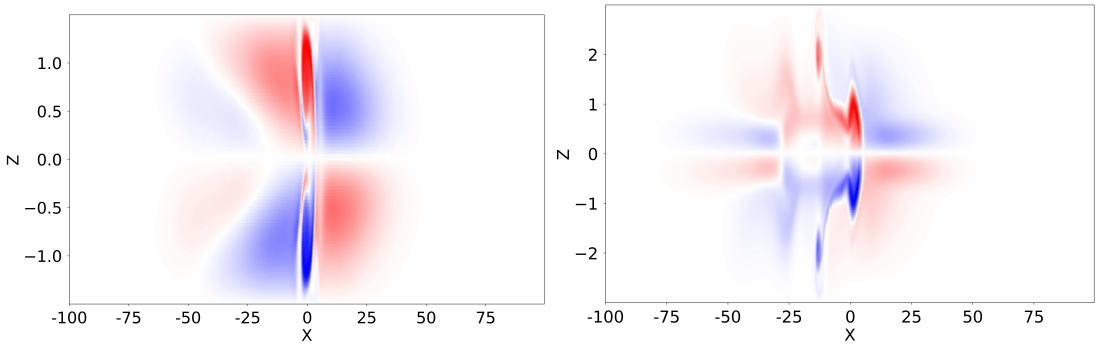


Figure 5.5: Contour plots showing the effect of vertical boundaries on flow field evolution.

ulations were initialized with the same initial perturbation of a ducted wave and in both cases, we can see the overturning vortex being formed. In the restricted domain, while there is a clear formation of the overturning vortex resembling KH instability, it may seem that this is due to the flow near the boundary being forced to evolve in such a manner as a result of rigid boundaries at

the top and bottom. To negate the boundary effects and to see whether the formation of such an overturning structure is not a numerical artifact, the extended vertical domain simulation was run. This results also in the flow evolution of overturning structures far away from the vertical boundaries. We can also see the breakaway of the vortex-like structure from the primary structure which might have been suppressed in the restricted domain. Nevertheless, we can conclude that the formation of the structures resembling KH instability is not a result of numerical artifacts. However, this also shows that the size of the domain should be carefully selected for the problem under investigation.

Chapter 6

Case study of a dissipating mesospheric bore: Observation and Direct Numerical Simulations

In this chapter

6.1 Observation of mesospheric undular bore in Airglow Imagers . . . 58
6.2 Background conditions during the bore propagation: Temperature and Stability profiles . . . 63
6.3 Background conditions during the bore propagation: Winds and Vertical Wavenumber . . . 65
6.4 2D Direct Numerical Simulations of bore . . . 68

In this chapter, the findings of a recent observation of a mesospheric undular bore between 90 and 97 km is reported. The investigation of this mesospheric observation is carried out using airglow imagers located in northern Germany with the coordinates 54°N and 12°E. Moreover, the observation was complemented by the usage of SABER temperature data and winds from the SIMONe radar network as a means to study the background conditions that were present during the observed event. Finally, two-dimensional (2D) direct numerical simulations were used to reproduce some of the features of the observation. The results and the discussion presented in this section have been published in Ramachandran et al. (2023)

6.1 Observation of mesospheric undular bore in Airglow Imagers

On March 16, 2021, the airglow imagers positioned at the Insitute of Atmospheric Physics, Kühlungsborn (54.1° N; 11.8° E) captured an interesting mesospheric event over northern Germany. Figure 6.1 shows the evolution, propagation, and subsequent dissipation of this mesospheric phenomenon as a sequence of the O(^{1}S) airglow emission layer images. A lone wave was first detected entering the FOV of the imager from the southwest direction at around 21.30 UT. The appearance of the wavefront in the O(^{1}S) emission resulted in a sharp increase in the airglow intensity against a darker background, resulting in the wave appearing brighter. The propagation direction of the bore is from southwest to northeast. The front of the wave extended from horizon to horizon in the East-West(EW) direction with a horizontal extent of at least 500 kms. Initially, the left side (western side) of the front is more clearly visible than the right side(eastern side) but later on at 21.50 UT, the full wavefront becomes visible with an EW orientation. By 22.00 UT, the features of the mesospheric wavefront start to become apparent in that trailing wave undulations begin to form. Also at time 21:30 UT, one can see a slight "bend" of the frontal structure in the zonal direction which is not visible at later times. Hozumi et al. (2018) and Mondal et al. (2021) also see this peculiar pattern of horizontal undulation of the frontal structure although the horizontal undulation of their wavefronts is in the range of a few hundred kilometers. Particularly, the undular bore structure reported by Hozumi et al. (2018) had a horizontal undulating wavefront of around 1000 km. This feature of a leading edge wavefront with trailing waves fits the description of an undular mesospheric bore (Dewan and Picard, 1998). The trailing waves appear to be phase-locked to the leading wavefront traveling at the same speed. A maximum of three trailing waves were observed when the bore reached the zenith between 22:20 and 22:36 UT before it dissipated into the background. The dissipation first starts on the right side (eastern side) of the image as one can still see the frontal structure on the left side of the image at 23:00 UT. The dissipation then takes over the entire bore with the time for dissipation being less than 25 min.

Another interesting facet of this mesospheric bore observation was the presence of gravity waves propagating in the eastward direction of the airglow imager. These waves span the meridional distance of about 400 kms with wavelengths ranging from 18-60 km. It is well known that in the MLT, the dynamics are influenced by the non-linear interaction of the waves and it might be plausible that this large-scale GW could have had some influence on the propagation of the observed mesospheric bore. However, the following two features of this large-scale GW make it seem that it may not have had any role in the formation of the bore:

- Its propagation direction is perpendicular to the bore propagation direction

- It did not dissipate within the FOV, hence it could not have contributed to the formation of the thermal duct.

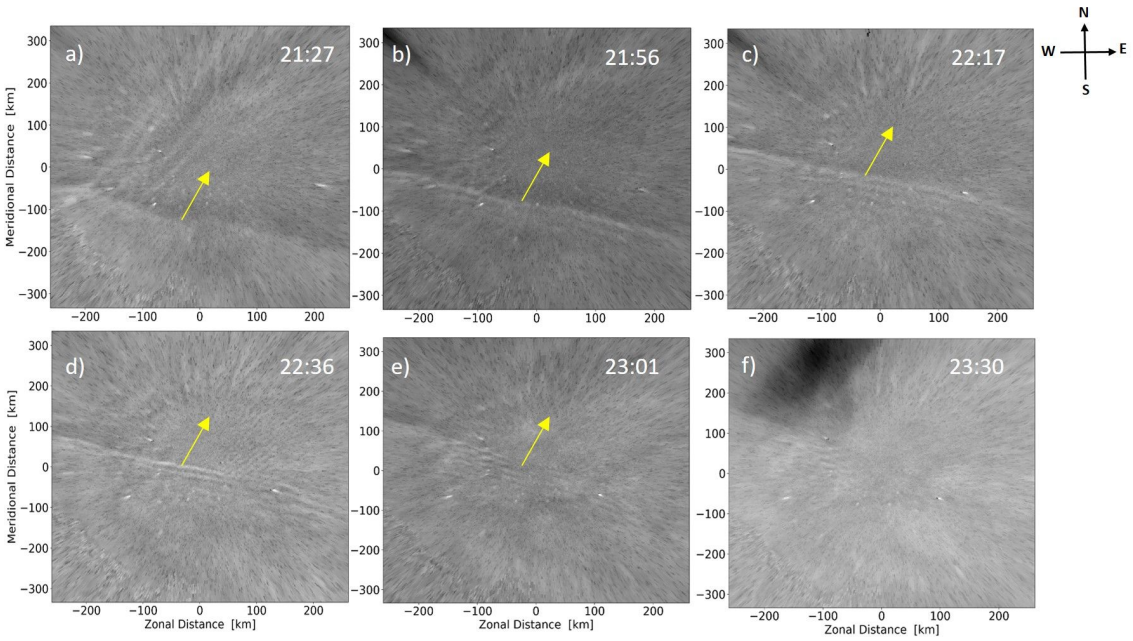


Figure 6.1: A sequence of O(^{1}S) 557.7 nm airglow images over northern Germany on March 16, 2021. A front-like structure appeared on the southwestern edge of the image at around 21:30 UT and propagated northeast in the consecutive images followed by trailing waves. The yellow arrow points in the direction of propagation. Figure taken from Ramachandran et al. (2023)

The signature of the mesospheric bore was also observed in the O_2 and OH emission layers at an altitude of 94 and 90 km, respectively as shown in Figure 6.2 and 6.3. The leading wavefront of the mesospheric bore is clearly visible also in the O_2 and OH emission layers while the features that resemble the trailing wave undulations are only faintly visible at the earlier times. These trailing wave undulations indeed become more visible at later times (22:36 UT) before the bore dissipates. In this emission layer, a slight bend of the wavefront, which was also apparent in the O(^{1}S)(5577nm), is also visible. Also seen are the eastward propagating GWs spanning almost the entire meridional extent. As in the O(^{1}S), the bore reaches the zenith of the field of view of the imager before the dissipation sets in with the eastern side dissipating first followed by the western part of the bore.

Upon looking at the emission layer images between 22:30 UT and 22:50 UT, one could discern the presence of small-scale ripple-like structures in the center and eastern side of the images. Peterson and Adams (1983) and Taylor and Hapgood (1990) were the first to report such type of ripple-like structures from the nightglow emission. They identified these ripples as small-scale

wave patterns that are similar in their morphology to the billow-type waves seen in noctilucent clouds. Figure 6.4 shows the Keogram brightness plot of the different airglow images. Keograms

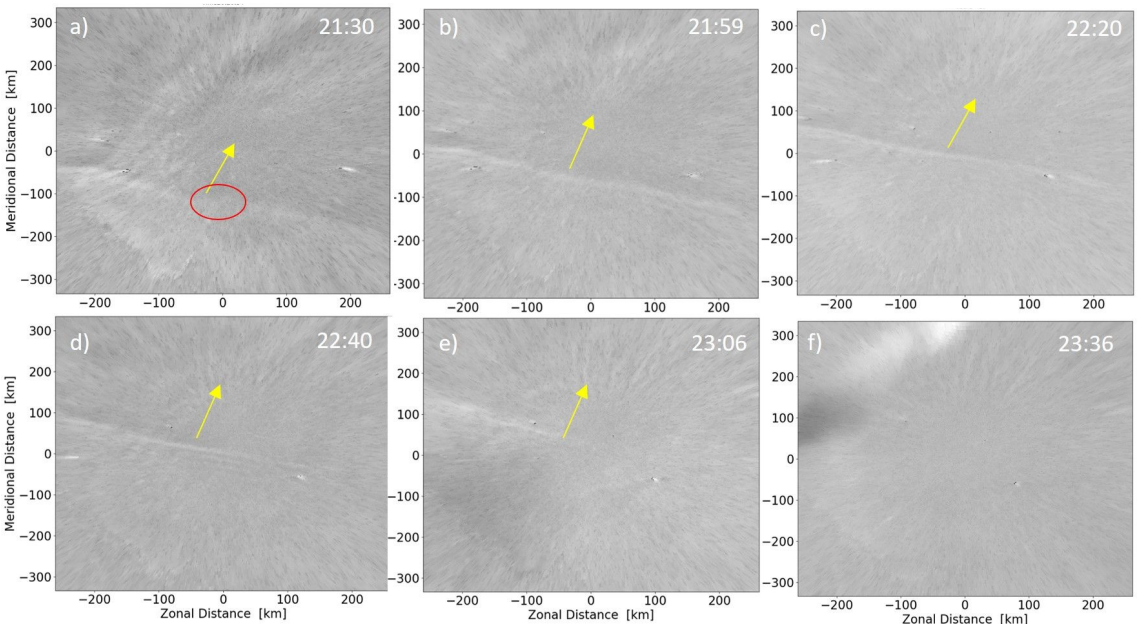


Figure 6.2: A sequence of $O(_2)$ airglow images over northern Germany on March 16, 2021. A front-like structure appeared in the southwestern edge of the image at around 21:30 UT and propagated northeast in the consecutive images followed by trailing waves. The yellow arrow points in the direction of propagation. Figure taken from Ramachandran et al. (2023)

are used as a practical tool in determining the wave activity throughout the recorded night and allow one to determine the spatial and temporal activity wave activity as seen in terms of latitude and longitude of the area. The banded structure denoted by the black oval represents the spatial and temporal limit of our bore event. The bright red pixels at the center of the image are an indication of the presence of the bore structure seen in the airglow images. It is clear that the bore starts to form at around 21:30 UT and with time the trailing undulations are visible. The keogram of the $O(^1S)$ layer shows multiple red bands starting at around 22.00 UT which is a clear indicator of the trailing wave undulations as is seen in the residual images (Figure 6.1). By obtaining the spatial and temporal information of the bore from the Keogram, the horizontal phase speed of the bore was calculated. The observed phase speed from $O(^1S)$, O_2 and OH images are 30 ± 7 m/s 25 ± 6 m/s and 28 ± 5 m/s, respectively. The airglow instrument is setup in such a way that the filters cannot provide simultaneous observations of all three layers thereby resulting in a small time delay between each measurement. The time delay (dt) between $O(^1S)$, O_2 and OH images are 61 and 88 s respectively. Since there is a slight delay in the measurement of each filter, there will be a time lag when calculating the intensity variation between the different layers. To rectify this problem, the horizontal displacement of the bore during the aforementioned time delays is calculated us-

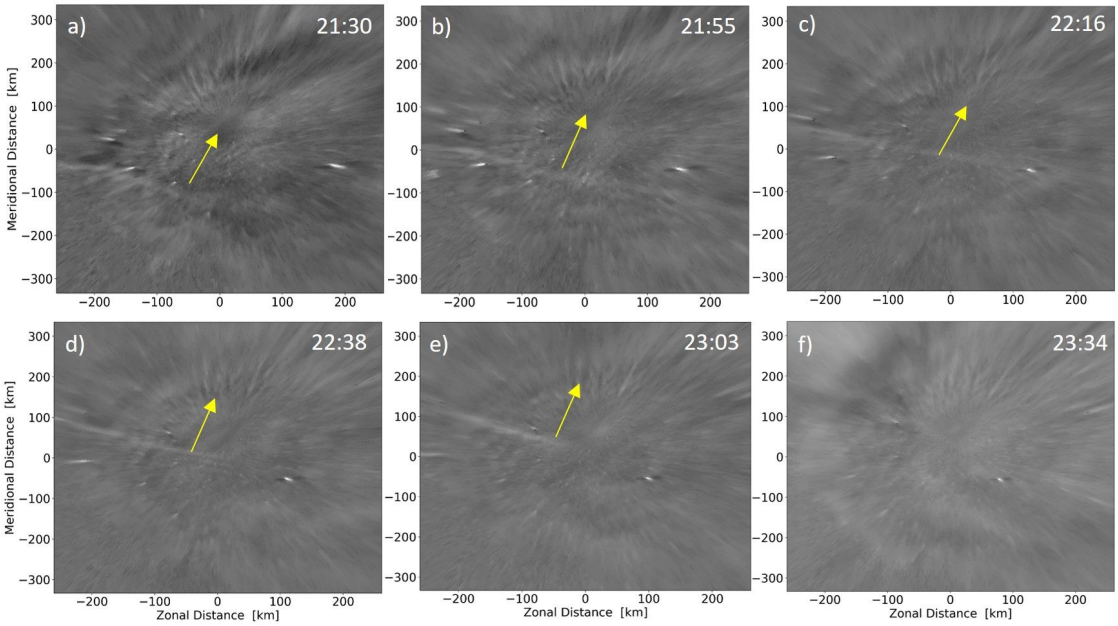


Figure 6.3: A sequence of OH airglow images over northern Germany on March 16, 2021. A front-like structure appeared in the southwestern edge of the image at around 21:30 UT and propagated northeast in the consecutive images followed by trailing waves. The yellow arrow points in the direction of propagation.Figure taken from Ramachandran et al. (2023)

ing the mean phase speed of the bore, and the displacements are added to the O_2 and OH distance scale. To put it more concisely these intensity curves have been horizontally shifted based on the calculated phase speed of the leading front and taking the average phase speed of three layers as a reference to account for the time difference between each image in the different layer. This result is shown in Figure 6.5 with the intensity variation of $O(^1S)$, O_2, and OH layers marked by magenta, green, and blue lines at the same time in each frame along the direction of propagation, respectively. The propagation of the bore will cause perturbations in the emission layers which in turn will cause the brightness intensity of the layers to change. To calculate the brightness intensity, the directional position North is first fixed concerning the bore propagation. The residual images of the different layers are then rotated by an azimuth angle of 14° in the anti-clockwise direction from North thereby making the orientation of the bore parallel to the East-West and finally taking an average in the direction perpendicular to the bore propagation, (i.e) East-West direction. There is a clear lag in the phase between the different layers at 21:48 UT with a downward phase progression could be an indication of an upward propagating gravity wave. In the next 15 mins of the observation, the phase lag between the $O(^1S)$ and O_2 has become negligible indicating that the GW that was propagating upwards may have been trapped near the $O(^1S)$ emission altitude and started evolving as a bore. At a later time, all three layers exhibit an in-phase alignment and the trailing waves start to appear. A very clear presence of the trailing undulations is first visible

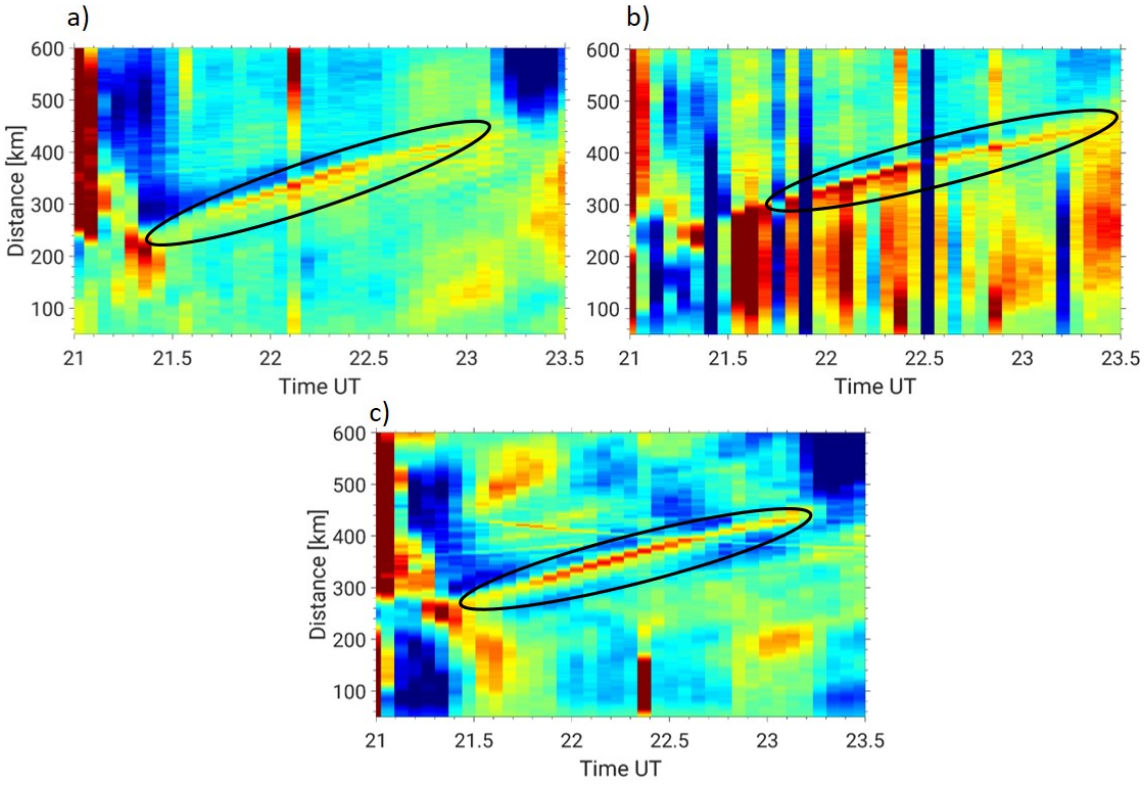


Figure 6.4: Keogram brightness plot of different airglow layers. a) O(^{1}S) airglow emission, b) O_2 airglow emission, and c) OH airglow emission. The solid black oval indicates the structure of the undular bore in the airglow.

in the O(^{1}S) images (Figure 6.5(b)) while the other images show the undulations at a later time (>22.00 UT). In total, the O(^{1}S) layer shows at least 3 trailing undulations while the other two layers show at least 1 trailing undulation. The non-linear steeping of the emission layers followed by the sharp front-like structure at 21:48 UT is consistent with the non-linear effects and the complementary effects of the airglow layers proposed by Dewan and Picard (1998) where during the passage of a bore the layers are pushed up and down. This up and down movement of the layers causes adiabatic heating and cooling of the layer leading to them becoming denser and brighter when pushed down and less denser and darker when pushed up. Our mesospheric event is an internal undular bore since the relative changes in the emission layers are in phase with each other. In other words, during the bore passage the emission layers are all pushed down to a warmer region thereby resulting in an increased brightness intensity (see Figure 6.5). Similar to the bores, there are other frontal events called the "wall" waves that have been reported in the literature (Li et al., 2007; Li et al., 2013). The first distinguishing feature of our bore observation compared to the "wall" wave event reported by Li et al. (2007) and Bageston et al. (2011) is that the wall wave is an upward propagating GW, with a clear leading and ending edge, leads to a significant time

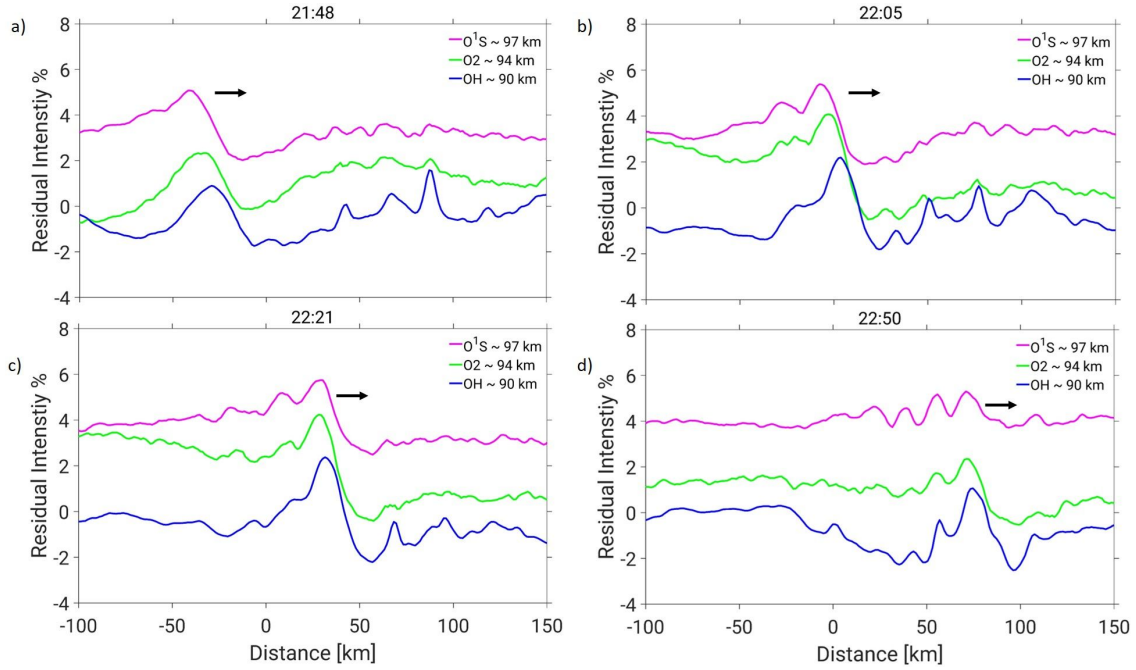


Figure 6.5: (a–d) The magenta, green, and blue solid lines in each panel depict the intensity variation of $O(^1S)$, O_2, and OH airglow emissions at constant time, respectively along their line of propagation. The black arrow indicates the propagation direction. Figure taken from Ramachandran et al. (2023)

delay between different airglow emission layers which results in the layers being 90° out of phase with each other. The bore is phase-locked with no phase variation in the altitude (i.e.) the airglow layers exhibit the same phase. Secondly, the bore will generate waves, or an increasing region of turbulence, behind the leading wavefront as it propagates along (Fritts et al., 2020). While for a wall wave, an inversion layer is not required, the existence of the inversion layer is crucial for the bore theory (Li et al., 2007). Therefore it is important to look into the background temperature and stability profiles during the time of the event.

6.2 Background conditions during the bore propagation: Temperature and Stability profiles

Figure 6.6 shows the altitude profile of the background temperature and the static stability (N^2) at two different locations which are located with ≈ 400 km from the bore observation location. The emission altitudes of the airglow layers are marked by horizontal dotted lines. The level-2 data obtained from TIMED SABER has a vertical resolution of 300 m. This data was then interpolated

every 1 km in order to make the vertical resolution of the temperature profile and the wind profile consistent. Upon looking at the two profiles in Figure 6.6, one can recognize the presence of two

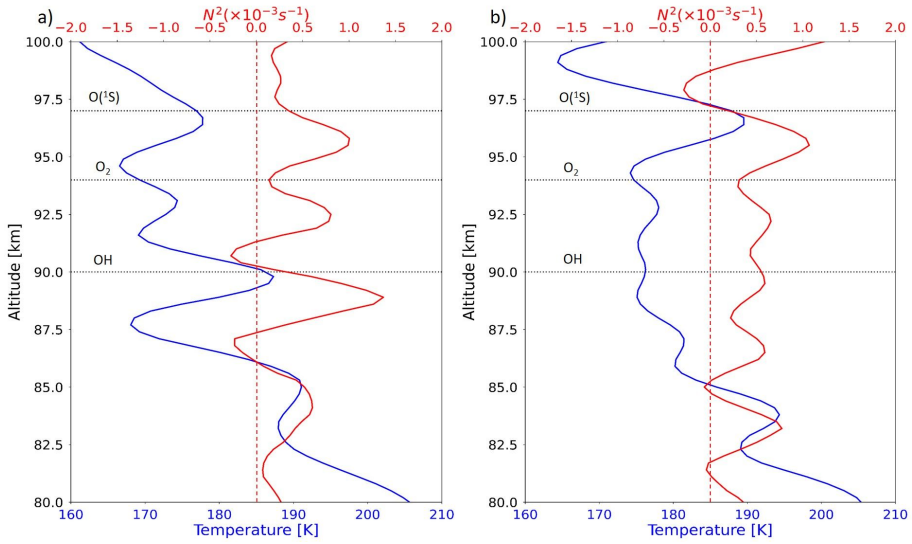


Figure 6.6: (a) SABER-1 (23:58 UT, 50.10°N, 9.57°E) and (b) SABER-2 (23:59 UT, 51.06°N, 15.47°E) represents the vertical profile of temperature from SABER (blue line) and the corresponding squared Brunt-Väisälä frequency (N 2) profile (red line) at two different locations on 16 March 2021. The horizontal solid lines indicate the peak emission altitudes of O(1S), O2, and OH airglow emissions on 16 March 2021. The vertical red dashed lines point to zero values in the stability profile. A persistent inversion layer is visible between 95 and 97 km. Figure taken from Ramachandran et al. (2023)

inversion layers in the SABER-1 profile: an upper inversion layer of ≈ 15 K centered between the O_2 and the O(^{1}S) emission layers altitude(95-97 km) and a lower inversion layer of ≈ 20 K near the OH emission layer altitude(88-90 km) while the SABER-2 profile has only one inversion layer of ≈ 15 K between the O_2 and the O(^{1}S) emission layers altitude(95-97 km). Normally, the altitude of the OH peak emission is around 87 km but on the day of the observed event, the peak emission of the OH emission layer was at around 90 km which is shown in Figure 6.7. According to the complementary effects proposed by Dewan and Picard (1998), and shown in Figure 6.5, all three emission layers during the observations show an increase in the brightness intensity as the bore was propagating. This means that the thermal duct that enabled the bore propagation can only be located near the O(^{1}S) emission layer altitude, between 95-97 km. Medeiros et al. (2005) investigated the different responses of the bore seen in O(^{1}S), O_2 and OH emission layers and concluded that for a bore to be bright in all three layers, the duct should be located above all the layers. SABER v2.0 satellite scans a horizontal area of 200-300 km and measures the energy emitted from this large horizontal surface area. So the temperature profile is to be taken to represent the background conditions that may have existed when the bore was observed. Moreover, the vertical stability profile (N^2)

profile shows a duct region near the O(^{1}S) peak emission altitude at both the measured locations. Therefore, it is safe to say that this thermal duct supported the formation of the bore.

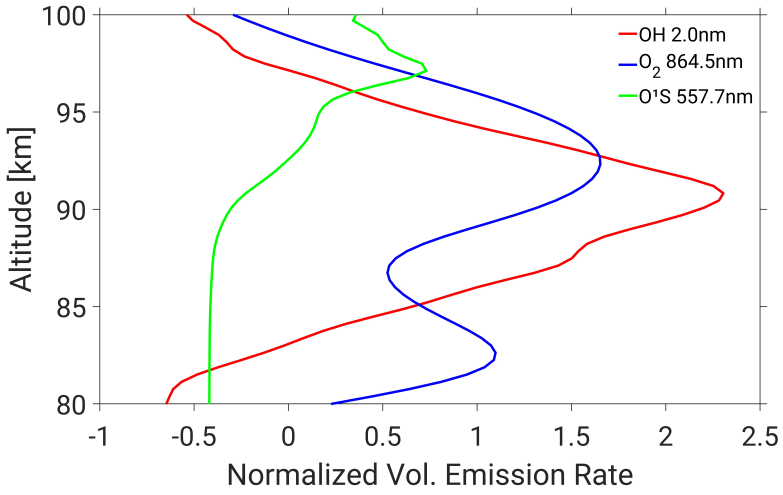


Figure 6.7: Volumetric emission rate of different airglow layer on 16 March 2021

6.3 Background conditions during the bore propagation: Winds and Vertical Wavenumber

Since mesospheric bores are formed due to upward propagating gravity waves that get trapped inside a duct caused by an inversion layer or/and wind shear and propagate horizontally in a duct, it is also important to look into the vertical propagation characteristics of the wave structure (Smith et al., 2017; Fritts et al., 2020). It has been mentioned in Chapter 3 that the background conditions conducive for the bore formation and propagation can not only be in the form of thermal duct/inversion but also due to the wind shear. There has been plenty reported in the literature on the ducting of waves due to the presence of regions of evanescence that trap the vertically propagating GWs Therefore it is pertinent to look into the background wind conditions that were present during the bore observation. The background winds over northern Germany obtained from the SIMONe network for the 15 and 16 March 2021 are shown in Figure 6.8. The vertical dashed line indicates the period of the observed undular mesospheric bore. On the day of the mesospheric bore event, 16 March 2021, we see a clear pattern in the wind that resembles semi-diurnal tidal activity in both the zonal and meridional components. Moreover, the magnitude of the winds on

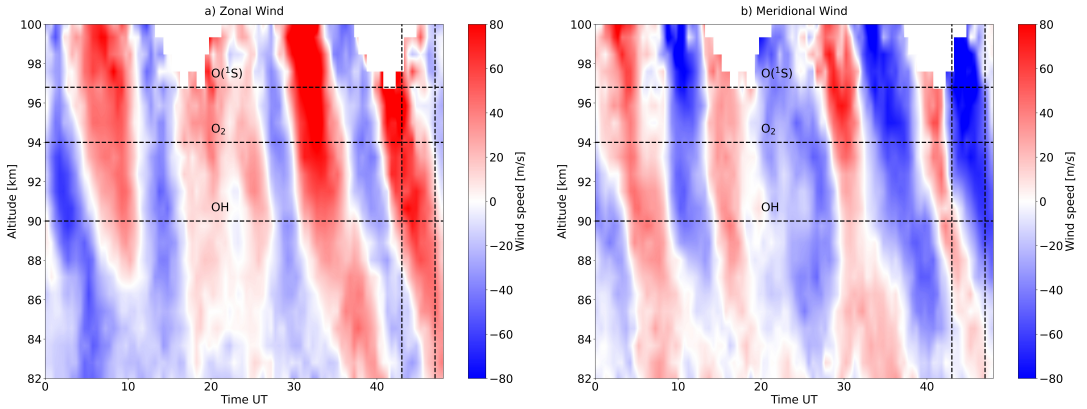


Figure 6.8: (a) The zonal, (b) the meridional winds on 15 and 16 March 2021. The horizontal dotted lines indicate the peak emission altitudes of O(^{1}S), O_2, and OH airglow emissions on 16 March 2021. The two vertical dotted lines indicate the time limit of the bore event on 16 March 2021.

the event day is 20-30 m/s larger than on the previous day. Jaen et al. (2022) reported the climatology of the zonal and meridional winds over northern Germany between 1999 - 2022 and the mean value of zonal and meridional wind during March is around 50 m/s and 30 m/s, respectively. This shows that the winds that were reported on the day of the event were much larger than the climatological mean. The winds also exhibit a change in direction from east to west and north to south before and after the bore event, respectively. This suggests that in addition to the thermal duct provided by the temperature inversion, the wind gradient may also have had some contribution in the form of the Doppler duct to the formation and propagation of the bore during this night. The resultant wind has mostly eastward at 90 km, it changed to southward at 94 km. Coincidentally, the resultant wind was in the southwest direction at 97 km which is the level of peak O(^{1}S) emission, which nearly is opposite to the direction of bore propagation. This schematic of the resultant wind direction and the bore propagation direction is shown in Figure 6.9.

To investigate further the existence of a possible wind ducting, one should calculate the vertical wavenumber profile in order to establish the regions of evanescence that permit the conditions conducive for bore propagation (Smith et al., 2017). With the available temperature and wind profiles and by taking the WKB approximation of the Taylor-Goldstein equation, the vertical wavenumber relation can be approximately given by,

$$m^2(z) = \frac{N^2}{(c-u)^2} + \frac{U_{zz}}{(c-u)} - k^2 - \frac{1}{4H^2} \tag{6.1}$$

which characterizes the conditions required for the vertical propagation of GWs.

The vertical wavenumber profile as a function of height for the O(^{1}S) emission layer calculated from the available SABER temperature and wind profiles is shown in Figure 6.10(a). It is evident

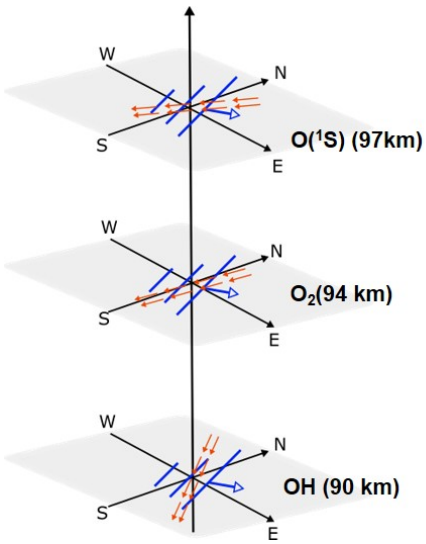


Figure 6.9: Schematic of the bore propagation direction and the resultant wind direction at different emission altitudes. The blue solid lines indicate the bore direction and orange arrows indicate the wind direction

that there is a region near 97 km where the m^2 is positive which means that GW propagation is allowed. This small region is bounded on the top and bottom by regions where the m^2 is negative otherwise called the regions of evanescence. This profile along with the temperature and stability profile supports our assumption that the duct that enabled the bore propagation was centered near the O(^{1}S) emission altitude.

Since the background wind consists of wind components of different horizontal and temporal scales, like tides and GW, we wanted to check the contribution of different forcings to the background wind. Figures 6.10(b) and (c) show the amplitudes of the zonal and meridional winds between 90 and 97 km and the FFT of the zonal and meridional winds. It can be very clearly seen that on the day of the observed event, there was a very clear enhancement in the winds compared to the days before and after. Looking at the individual components of the tides we found that in addition to the semi-diurnal tide, there was also a significant presence of an 8-hour tide in both the winds during the day of the event. This could mean that the presence of a significant 8-hour tidal component in addition to the semi-diurnal tide may have resulted in the enhancement of the winds leading to the bore generation (Smith et al., 2017; Hozumi et al., 2019).

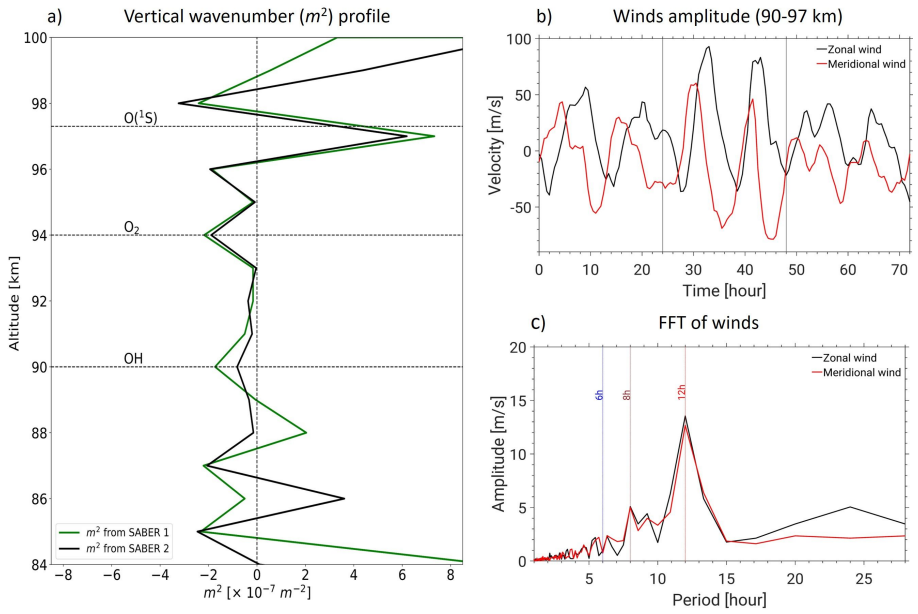


Figure 6.10: a) Profiles of m^2 derived from SABER 1 (green line), SABER 2 (black line), and the winds. b) Zonal and Meridional wind amplitudes between 90 and 97 km for days 15, 16, and 17th March 2021. The vertical line denotes the day of the observed undular bore event (16 March 2021). There is a clear increase in the amplitude of the winds during this time compared to the day before and after. c) FFT of the winds where the 6h, 8h, and 12h tides are marked by vertical dotted lines.

6.4 2D Direct Numerical Simulations of bore

One of the main facets that is explored in this thesis is investigating the instabilities using direct numerical simulations. This is accomplished by complementing the bore mentioned above observation with numerical simulation and seeing how well the simulations could reproduce the observation taking into account similar background conditions. As has been reported in plenty of literature, the presence of the thermal inversion layer is crucial for the formation of the bore since it acts as a channel in which the bore can propagate. While the presence of the wind shear may also play an important role in the formation of the bore (Fechine et al., 2009; Bageston et al., 2011; Smith et al., 2017), a first approximation was done to test the efficacy of thermal duct alone with background wind being constant. Since there is no considerable change in the structure of the bore to the horizontal extent, the dynamics assumed in the simulation of the bore were 2D and nonlinear, with periodic boundaries in the horizontal with rigid upper and lower boundaries. The upper and lower boundaries are defined by no-slip boundary conditions. The simulation domain employed a grid of 1,024 spectral modes in the horizontal and 512 modes in the vertical. It is well known that for the generation of undular bores, some form of ducting structure needs to be present (thermal or Doppler) to act as a guiding channel for their evolution and propagation

(Dewan and Picard, 1998; Smith et al., 2003). This ducting structure in the simulations is given in the form of an idealized stability profile (N^2) from which the background temperature profile can be obtained using 2.58. Following Seyler (2005), we let the buoyancy period at the maximum of the stability duct be our fundamental time scale (N^{-1}) and the half-width of the duct be the length scale. The values for the maximum value of the stability and the half-width of the duct in the simulations are taken from the observation data ($N^2 = 1 \times 10^{-3} s^{-2}$ and 1.5 km). The corresponding kinematic viscosity in the mesopause altitudes is around 10 m^2 s^{-1} (Hines, 1960) and when non-dimensionalized concerning the length and time scale yields a value of 0.001 (Seyler, 2005). We set $\nu = \kappa$ so that the Prandtl number is 1. This value of kinematic viscosity is large enough to affect the bore formation. The simulations are initialized with a sinusoidal waveform imposing the stream function and potential temperature perturbations. Since the vertical domain is bounded, the vertical wavelength is chosen to be comparable to the thickness of the duct in each case. The initial stream function and potential temperature (non-dimensional) perturbations are of the form,

$$\psi(x, z, 0) = Asin\left(\frac{2\pi(x - \frac{L_x}{2})}{L_x}\right) sin\left(\frac{n\pi z}{L_z}\right) * G(x) \tag{6.2}$$

$$\theta(x, z, 0) = -\frac{0.4\pi A}{L_z} Asin\left(\frac{2\pi(x - \frac{L_x}{2})}{L_x}\right) sin\left(\frac{n\pi z}{L_z}\right) * G(x) \tag{6.3}$$

$$G(x) = exp(-\frac{(x - L_x/2)^2}{L_x}) \tag{6.4}$$

where A is the non-dimensional amplitude of the initial perturbation, L_x and L_z are the non-dimensional horizontal and vertical wavelengths, respectively. These values are non-dimensionalized to the chosen length scale. The initial perturbations of the function and the potential temperature are multiplied by a Gaussian envelope function G(x), given by Equation 6.4, so that the initial perturbation is centered in the domain. In doing so, the initial perturbation becomes only a fraction of the horizontal extent of the simulated domain. This is in contrast to the approach employed by Seyler (2005) where the given initial perturbation was a long wavelength ducted GW over the entire horizontal domain. The initial perturbation and the background thermal ducts used are shown in Figure 6.11.

The results of this are shown in Figure 6.12 where the left side of the figure shows the time evolution of the undular mesospheric bore as captured from O(^{1}S) airglow imager and the right side shows the results from 2D DNS. The tracer lines indicate the brightness intensity where the time series were obtained by rotating the residual images by an azimuth angle of 14° in the anticlockwise direction from north and then taking the zonal average. The intensity traces are offset by a constant factor of 2 in the vertical for clarity. The lowest trace corresponds to time 21:30 UT and

the top trace to time 23:20 UT. Immediately apparent at 21:30 UT is the decrease and a subsequent increase in the brightness intensity at approximately 250-300 km. When a layer is pushed down adiabatically, the layer becomes warmer, and denser which leads to an increase in the brightness intensity (Dewan and Picard, 1998). The process that leads to the formation of a wavefront or a bore is the nonlinear interaction followed by a steepening of the wave to form a frontal structure. This is evident at time 21:48 UT where the wave exhibits a steepening behavior to form a sharp peak. As the wavefront propagates, one can see the appearance of a trailing wave at 22:05 UT. This process continues and more trailing waves start to appear as the bore propagates further on and finally at around 23:20 UT, no signature of the bore front or its undulation is seen which leads to the conclusion that the dissipation had taken place.

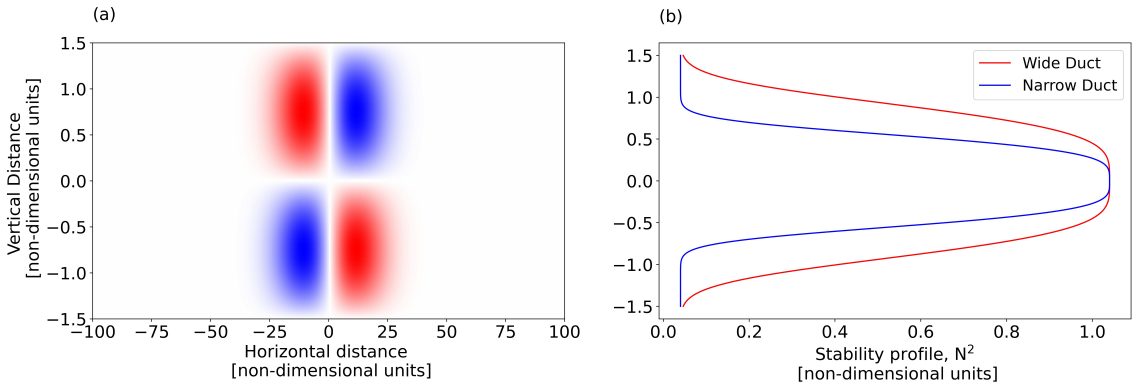


Figure 6.11: (a) Initial perturbation in the form of ducted gravity wave. (b) Thermal duct for two different cases simulated.

Figure 6.12(b) shows the result of a DNS with the background duct having a non-dimensional width of 2, an initial perturbation of amplitude, A 0.08, and a constant background wind. The line traces shown are shifted horizontally by removing the bore's phase velocity and are depicted in the frame of reference where the bore is stationary. The lowest trace corresponds to $T = 0$ s with subsequent traces offset in the vertical by a constant value for clarity. The time evolution shows the nonlinear evolution of the system when initialized with a sinusoidal waveform, which is the most efficient in forming bores (Seyler, 2005). At the time $T = 50$ s one can see that the initial sinusoidal wave undergoes nonlinear steepening which resembles the steepening of the wave as shown in Figure 6.10(a), as observed in the O(^1S) layer. As the bore evolves further, one can see the evolution of the wavefront into a sharp peak ($T = 74$s), the appearance of the first trailing undulation ($T = 110$ s) followed by more of them as the bore evolves. This is followed by the onset of the dissipation as the front of the bore starts losing its amplitude.

It is important to point out here that the nonlinear response that is shown in the above figure is very similar to that obtained by Seyler (2005) and Laughman et al. (2009). However, their studies

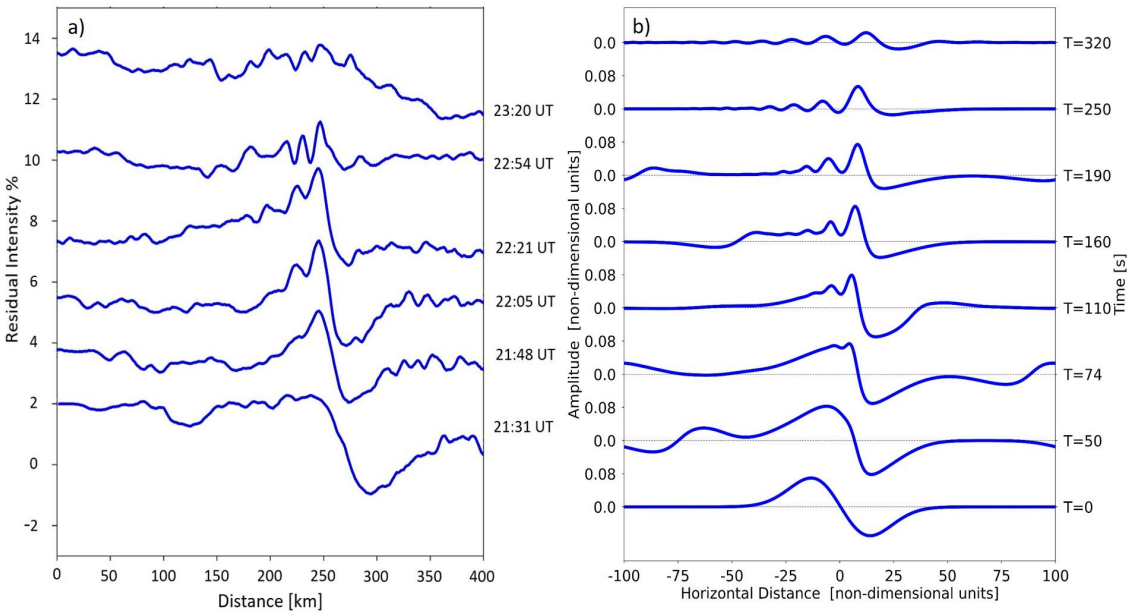


Figure 6.12: (a) Brightness intensity plot showing the temporal and spatial evolution of undular bore in O(^{1}S) 557.7 nm airglow emission. The lines are shifted vertically by an offset factor of 2 to represent the time evolution. The time series was obtained by rotating the residual images by an azimuth angle of 14° in the anti-clockwise direction from North and then taking a zonal average (i.e.) in the direction perpendicular to the bore propagation. (b) Potential temperature traces from DNS representing the undular bore evolution with initial amplitude, A $\approx$ 0.08 for wide duct with constant background wind. Figure taken from Ramachandran et al. (2023)

and the results presented here have one major quantitative difference. In the simulations carried out by Seyler (2005) and Laughman et al. (2009), the initial perturbation that led to the evolution of a bore was a long gravity wave in a ducted mode that covered the entire horizontal domain. In the case presented here, the nonlinear bore evolution resulted from an initial perturbation that was just a fraction of the horizontal domain simulated. As has been first stated by Dewan and Picard (1998) and further proved by Smith et al. (2003) and Smith et al. (2017), the loss of energy of the bore can be due to the energy being lost away from the duct. Or the wavefront loses its energy as more trailing waves are being added to the bore as the energy for the formation of the trailing wave comes from the wavefront itself. The initial DNS simulation with thermal duct and constant background wind shows that many of the features of the observed bore can be reproduced using an idealized 2D Boussinesq approach. Using a ducted gravity wave as an initial condition, the non-linear steepening of the observed wave is reproduced to a very good degree (See Figure6.12(a) and Figure6.12(b)). The initial ducted gravity wave has a non-dimensional horizontal wavelength of 60 which is at least 3 times smaller than the horizontal extent of the simulated domain. There is a good agreement between the airglow observation of the bore and the simulation in terms of the morphology of the bore like the non-linear process in the bore formation, and the number of

trailing undulations formed (3 in both cases). It should also be pointed out here that the simulations done by Seyler (2005) did not consider the diffusion terms in the numerical simulations thereby resulting in an unnatural number of trailing waves being formed ($>$8) which is very rarely observed since the typical undular bores has 4-5 trailing undulation (Smith et al., 2003; Smith et al., 2017). Furthermore, the rate of addition of the trailing waves is also an indicator of the dissipation rate of the bore (Dewan and Picard, 1998). In the present case, the waves are added at a rate of 2 waves per hour which is close to what has been reported before (Smith et al., 2003; Seyler, 2005; Smith et al., 2017).

To get a physical sense of the relation between the observation and the simulation, the DNS results are scaled back to the physical space where we set a length scale of $\approx$ 1.5 km which is approximately the half-width of the thermal duct near the O(^{1}S) emission altitude. With this, the horizontal wavelength of the longest undulation is $\approx$ 20 km (determined 3/4 of the way through the simulation) which agrees relatively well with the wavelength of the observed bore (Figure 6.12(a). Seyler (2005) and Laughman et al. (2009) also reported similar values of the horizontal wavelength of their bores. To calculate the time taken for the bore to dissipate, we set a timescale of $\approx$ 0.032 s^{-1} which is the maximum buoyancy frequency obtained from the temperature profile (see Figure 6.6). Then the time taken for the bore to dissipate in the simulation is close to 135 min which is approximately the lifetime of the observed undular bore.

Chapter 7

Direct numerical simulations of instabilities and bores: 2D and 3D DNS

In this chapter

7.1 Effect of the thermal duct and the amplitude of initial perturbation on the instability generation 74
7.2 Instability generation in dual ducts: Thermal and Doppler ducts . 82
7.3 Generation of instabilities in vertically displaced ducts 92
7.4 Effect of viscosity on instability formation 94
7.5 Effect of the inversion layer magnitude 98
7.6 Can bores form in only Doppler ducts? 104
7.7 Three-dimensional simulation of instabilities 106

In this chapter, results of two- and three-dimensional direct numerical simulations of kilometer-scale instabilities are presented. Encouraged by the qualitative agreement between the simulations and the observations presented in the previous chapter, further simulations were carried out to investigate the effects of different parameters on bore evolution. This included changing the width of the duct, the initial amplitude of perturbation, and the strength of the inversion layer. Furthermore, the influence of background wind shear in the form of the Doppler duct and the vertical displacement of the thermal and Doppler duct to one another on the bore formation was

also explored. In addition, the generation of secondary instabilities like the Kelvin-Helmholtz instability from a ducted gravity wave initial condition is also reported. The chapter concludes by presenting the results of the first three-dimensional simulations of undular mesospheric bores. Some parts discussed in this chapter have been published in Ramachandran et al. (2023)

7.1 Effect of the thermal duct and the amplitude of initial perturbation on the instability generation

Lighthill (1978) gives a very comprehensive treatment of the different salient parameters that control the formation of the undular bore. Among them, the amplitude of the initial perturbation (ducted wave) and the duct width play an important role in determining the bore evolution. To investigate this numerically, 2D DNS was run with only thermal duct and constant wind as a background for various initial amplitudes and duct widths. The extent of the initial perturbation and the different ducting conditions are shown in Figure 7.1. The different thermal ducting widths used in this thesis are given in table 7.1.

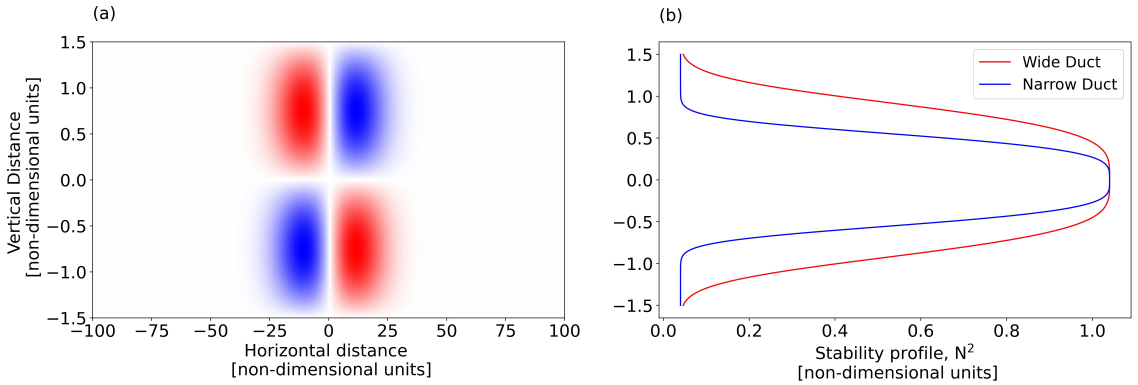


Figure 7.1: (a) XZ-cut of the simulation domain. The color contours represent the non-dimensional initial perturbation indicating ducted wave. The initial perturbation does not span the entire horizontal domain. (b) Background ducting profiles (N^2) used in the DNS. The wide duct (red) has a non-dimensional FWHM of ≈ 2.0 and a narrow duct (blue) has a value of ≈ 1.0. See Table 7.1 for more details.

Figure7.2 shows how the system responds to an initial amplitude of perturbation of A $\approx$ 0.10 (non-dimensional value) for two different ducting conditions. Plotted are the line traces of potential temperature that are used as a tracer to follow the bore evolution. The left side and the

Type	Full Width at Half Maximum (FWHM)
Case-1	1.0
Case-2	1.25
Case-3	1.5
Case-4	1.75
Case-5	2.0

Table 7.1: Different thermal duct widths that were used as a background condition in non-dimensional units.

right side of the figure show the evolution of an initial ducted wave for a narrow duct (Case-1) and a wider duct (Case-5), respectively. The propagation of the bore is from left to right and traces are plotted in the frame that is fixed to propagation so that the wavefront of the bore will appear to remain stationary. It becomes immediately apparent that the morphology of the bore has distinct differences between the two cases. Clear distinction of the bore characteristics such as the time taken for the initial peak formation, the steepening of the wavefront, the number of trailing undulations, and the dissipation can be seen. Both simulations are initialized with the same initial amplitude wave at $T = 0\ s$. Simulation results under Case-1 condition show that the initial peak formation at around $T = 50\ s$ results from the nonlinear steepening of the initial wave while at the same time, the system under Case-5 is still undergoing a nonlinear steepening process and results in a sharp peak only at time $T = 70\ s$. This is also evident in Figure 7.3 which shows the contours of the potential temperature perturbation evolution from an initial ducted gravity wave. At the time $T = 50\ s$, we can see for the narrow duct, the initial wave radiates much of its energy to the outside of the duct and a lone peak that has resulted from the initial wave while for the wide duct, the initial wave is still undergoing "distortion" with much of its energy still trapped inside the duct (Seyler, 2005; Laughman et al., 2009). It can also be seen in Figure 7.3 that the vertical extent of the bores is limited by the duct width as the bores in the wider duct system extend almost to the vertical boundaries while this is not the case for the narrow duct. Seyler (2005) reported this aspect of the bore formation that while the flow field can extend well beyond the duct layer, the bore perturbation will occur within the bounds of the duct. Moreover, the eventual peak amplitude obtained by the two systems is also affected by the duct width as is shown in Figure 7.2. Case-1(narrow duct) results in a much lower peak amplitude ($\approx$ 0.15) whereas for Case-5(wider duct) the maximum amplitude obtained is around $\approx$ 0.20. The dependence of the degree of bore undularity on the width of the duct has been theoretically explained by Lighthill (1978) and reported in the observation (Smith et al., 2003; Smith et al., 2017). Lighthill (1978) states that the significance of the nonlinearity to the dispersion of the wave depends on the parameter $a\lambda^2/h^3$, where *a* is the amplitude, λ the wavelength and *h* is the duct width. If this parameter is very large, which can happen either if the amplitude of the wave is large or the duct is very small, then the

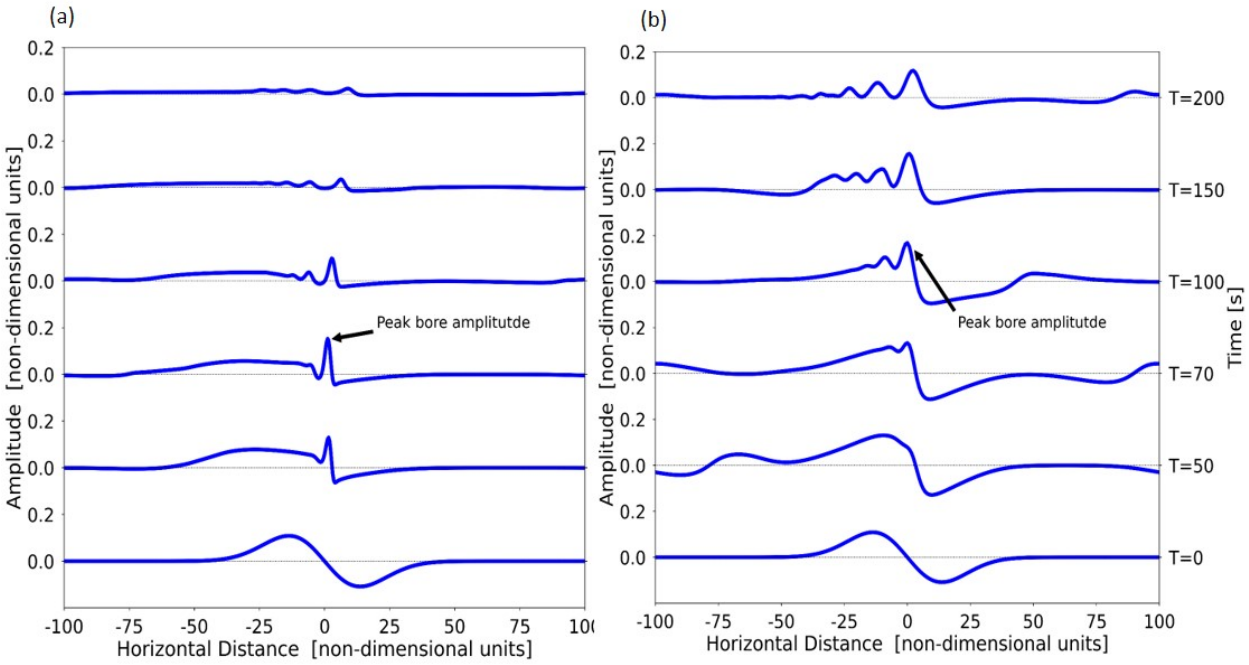


Figure 7.2: Time series of potential temperature line traces for (a) Case-1 and (b) Case-5. Both simulations were initialized with a non-dimensional amplitude of A ≈ 0.10. The inset text indicates peak bore amplitude. Each trace has been offset by a constant value for clarity.

nonlinear effects can proceed to steepen the wavefront of a wave much faster like in the case of hydraulic jump (Lighthill, 1978; Dewan and Picard, 1998). One could also see the apparent effect the duct width has on the bore dissipation in Figure 7.2. For Case-1(narrow duct) it can be seen that the loss of the energy of the bore front is much faster at an equivalent time than for Case-5(wider duct). The narrow duct yielded a total of 2 trailing undulations and the wider duct a total of 3 trailing undulations which are evident from Figures 7.2 and 7.3

According to the theory of bore proposed by Dewan and Picard (1998), the bore front loses energy in the following ways: the energy is leaked away from the duct to the surrounding flow due to reduced stability outside of the duct, energy lost from the front appears as trailing wave undulations or due to viscous attenuation. For the case of a narrow duct, the rate of loss of energy can be due to the combination of these factors as it can be seen in Figure7.2 (a) that the trailing undulations start to appear as the front loses its amplitude due to viscous damping. Additionally, due to the narrowness of the duct, it is also possible that the leakage of energy due to this is much higher than in a wider duct when all other parameters are the same. In Case-5 (wider duct), there is no hint of the dissipation of the energy at an equivalent time compared to Case-1. For example at time $T = 150\ s$, we can see that in Case-5, the initial ducted wave has fully evolved into a bore with

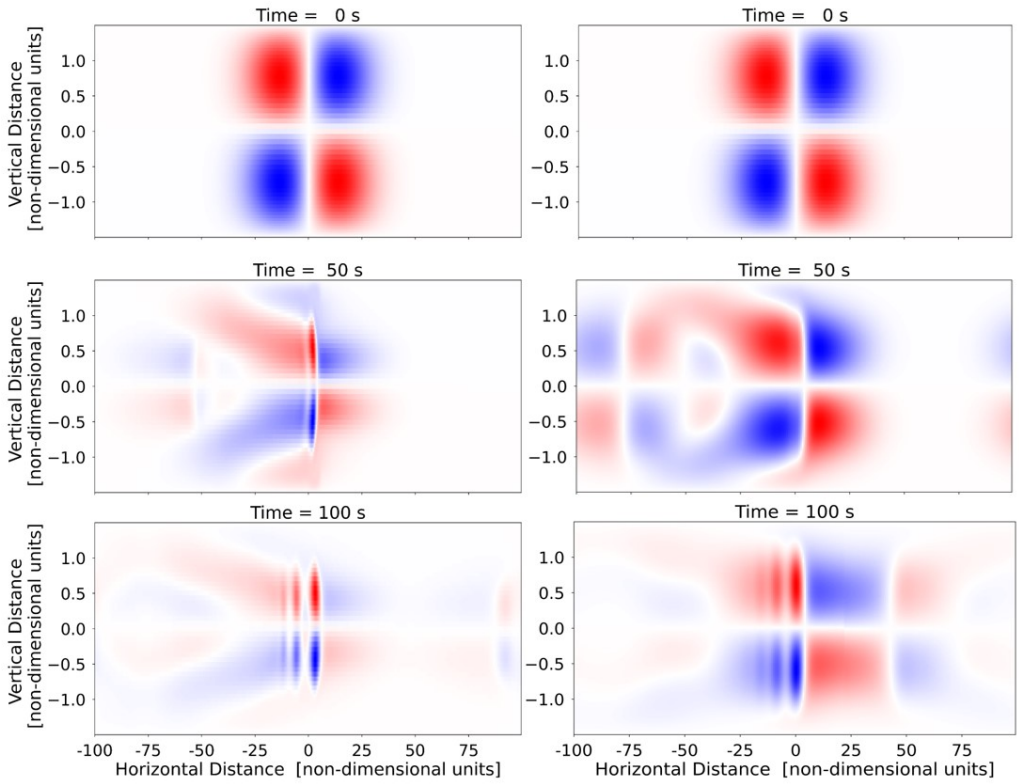


Figure 7.3: Contour plots of potential temperature evolution for Case-1 and Case-5 with a non-dimensional amplitude of A ≈ 0.10. Red is positive and blue is negative. Non-dimensional times are 0 s, 50 s, 100 s. Same as Figure 7.2

a well-established front and trailing waves whereas for Case-1(narrow duct), there are no distinguishing features that separate wavefront and those of the trailing waves. At the time $T = 200\ s$ one can still see the presence of the bore with the trailing waves for the wider duct but the bore has dissipated in the narrow duct. Also noticeable between the two systems is the difference in the wavelength of the leading wavefront which is smaller and narrower for the narrow duct while it is comparatively longer and broader for the wider duct. The trailing waves are phase-locked to the leading wavefront but their separation distance increases with time in both cases. This was also demonstrated by Seyler (2005) and Laughman et al. (2009).

Furthermore, as mentioned before, the nonlinearity of the bore is also related to the amplitude of the initial perturbation. So the effects of the amplitude on the nonlinearity of the bore evolution should be tested. To do this, the simulations were run for the above-mentioned duct widths but now the initial amplitude was doubled (i.e.) $A = 0.18$. The results are shown in Figure 7.4. Figure 7.4(a) shows the evolution when initialized with a narrow duct (Case-1) while on the right is the wider duct evolution (Case-5). It can be seen that when the amplitude of the initial perturbation is

the same, depending on the background ducting condition, the system yields different responses, a lone solitary wave in the case of a narrow duct and an undular bore structure for a winder duct. The sharp solitary peak shown in Figure7.4(a) is apparent at time $T = 40\ s$ which attains a peak amplitude at least 2.5 times that of the initial amplitude at around $T = 70\ s$ after which it rapidly dissipates. According to Drazin and Reid (2004), a flow is thought to be unstable if any distur-

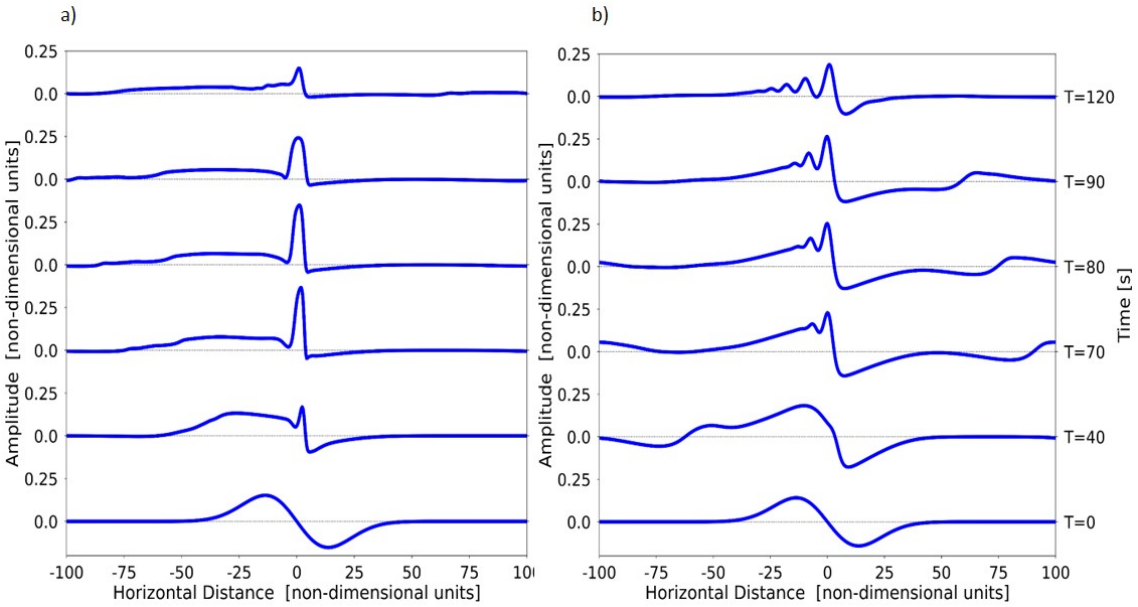


Figure 7.4: Time series of potential temperature line traces for (a) Case-1 and (b) Case-5. Both simulations were initialized with a non-dimensional amplitude of A ≈ 0.18. Each trace has been offset by a constant value to refer to the time evolution.

bance, which will have any noticeable effects on the flow itself, grows in amplitude rapidly. Figure 7.4 (b) shows that when the duct width is wider, the system yields an undular bore-like response. The nonlinear steepening of the initial wave, the formation of a sharp front (peak), and the formation of trailing undulations are all visible in this case as well at times $T = 40\ s, 70\ s$, and $90\ s$. In both the cases presented in Figures 7.2 and 7.4, for a narrow duct the steepening process of the initial wave leading to the formation of the sharp front is much more rapid than for a wider duct irrespective of whether the system's response is an undular bore type or a solitary wave. The contour plots in Figure 7.5(a) show a clear picture of the leakage of the energy away from the duct, the formation, and the persistence of the lone peak in the narrow duct at time $T = 50\ s$ while the wider duct in Figure 7.5(b) shows the evidence of the wave trapping at time $T = 50\ s$ leading to the subsequent formation of undular bore structure with at least 3 distinct trailing waves. Fritts et al. (2018) reported similar dynamics of wave trapping and instability formation inside different thermal ducts. Based on the evolution of the bores and solitary wave presented in Figures 7.2 and7.4, we can say that the loss of energy in a narrow duct is much faster compared to a wide duct.

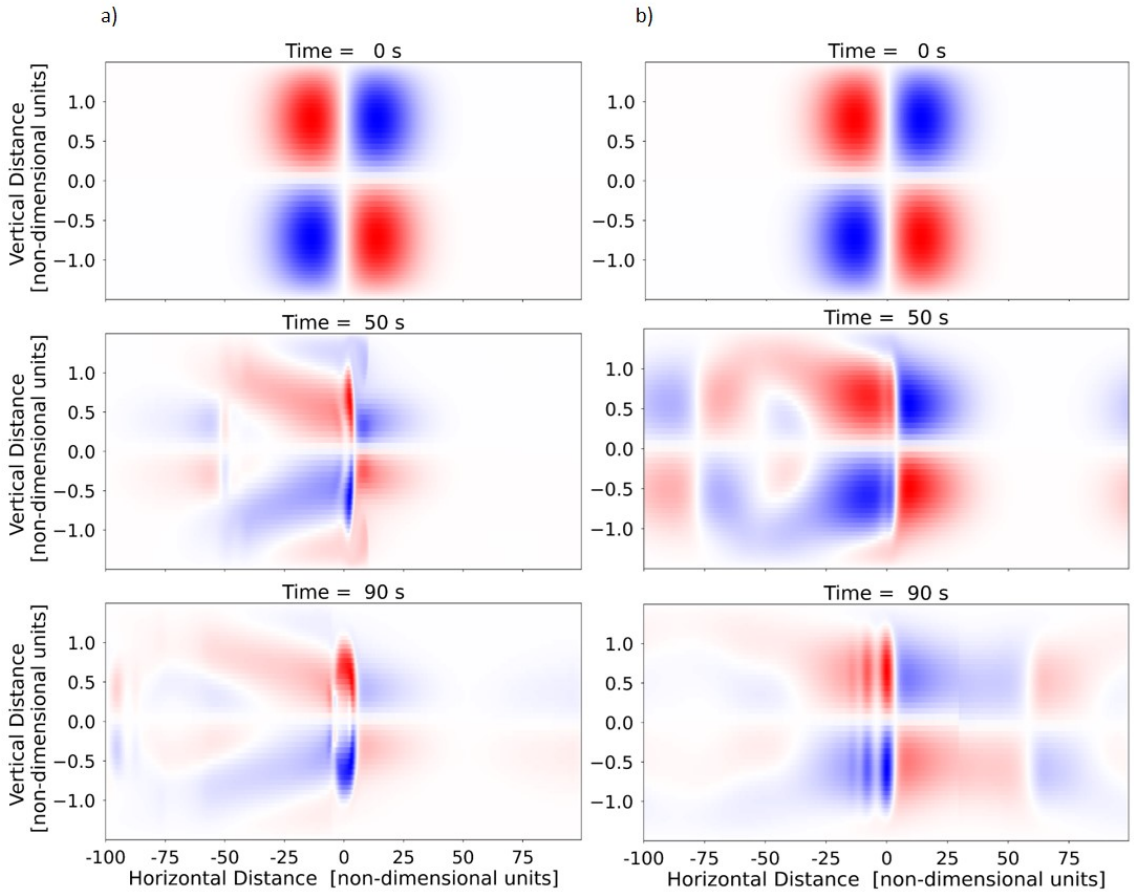


Figure 7.5: Contour plots of potential temperature evolution when initialized with an amplitude of 0.18 for (a) Case-1, and (b) Case-5. Red indicates a positive value and blue indicates a negative value. Non-dimensional times are 0 s, 50 s, 90 s. Same as Figure 7.4.

While these two cases present a valid argument on the importance of the duct thickness and the initial perturbation, it should be investigated if the system behaves consistently for various initial and background conditions within these two extreme ranges so that a comprehensive argument on the impact of the duct width and the initial perturbation can be made. Figure 7.7 displays the effect of different thermal ducting conditions and initial perturbations on the bore formation time, nonlinearity of bore evolution, and the dissipation of the bore.

Figure 7.6(a) shows the role of duct width on the formation time of the bore for different amplitudes of initial perturbation. As defined by Seyler (2005), bore formation time is the time for the emergence of the first dominant peak following the initialization of the wave. As the width of the duct increases, the time taken for the bore to form also increases. This behavior is consistent for all the simulated amplitudes of perturbations. This is due to the behavior of the narrow and wide

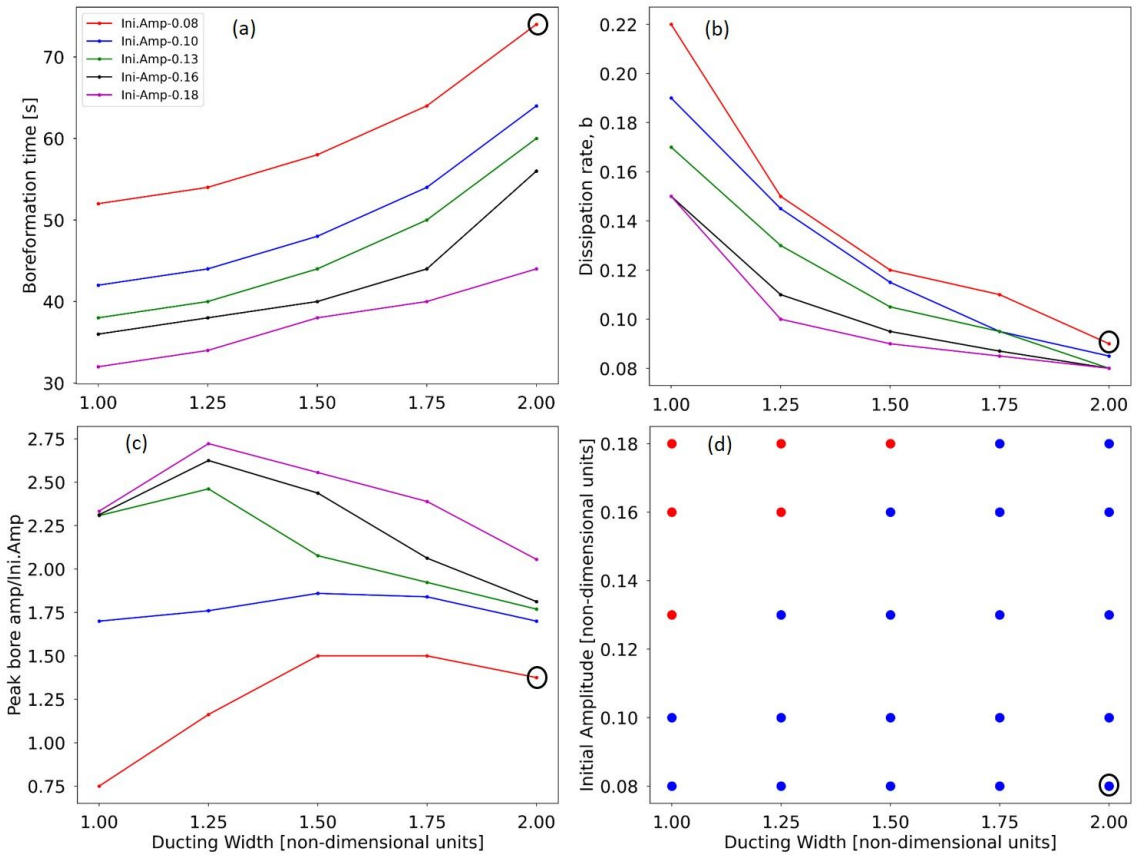


Figure 7.6: Effects of varying ducting conditions and initial perturbations. Figure taken from Ramachandran et al. (2023)

duct that was explained earlier and shows a consistent trend of the duct behavior on the bore evolution within these range of duct widths. From the point of view of constant duct width, if the amplitude of the initial perturbation is higher, then the bore formation time is lower. This makes sense since if the system is injected with more energy, then there is an increased nonlinear interaction of the flow leading to a more rapid formation of the bore. Also to be noted is that for low initial amplitudes, the time of bore formation very closely resembles an exponential increase with duct width while for high amplitudes, it varies more or less in a linear fashion. Laughman et al. (2009) also reported that the behavior of the bore was more nonlinear and the formation of the leading front of the bore was more rapid when narrowing the duct width.

Figure7.6(b) shows the effects of the duct width on the dissipation rate of the bore for different initial amplitudes. To calculate this, the bore amplitude as a function of time was determined and then an iterative process was implemented to determine the curve that best fit the data for each case. A system that was initialized with a wider duct takes a longer time to dissipate irrespective of the initial amplitude of perturbation. For a narrow duct, the loss of energy away from the duct

due to the flow interaction between the outside and the inside of the duct as a consequence of reduced stability away from the duct is more compared to when the duct is wider (Laughman et al., 2009; Fritts et al., 2018). Since the duct is a region of stability where the flow does not tend to develop instabilities, the narrower a duct is the larger the region of reduced instability away from the duct is. Conversely, for constant duct width, it is apparent that when the initial amplitude is higher then the dissipation time of the bore is longer since the higher the amplitude more the energy that is contained within the duct and hence it may take longer to dissipate. However, note that for the wider duct (Case-5) the difference in the dissipation rates between the different initial amplitudes is small compared to the narrow duct (Case-1).

The effect of the duct thickness on the nonlinearity of the bore evolution is shown in Figure 7.6(c). The amplitude ratio is defined as the ratio of the peak amplitude that the bore reaches to the initial amplitude of perturbation. It can be seen that there is a clear distinction between the response of low and high initial amplitude perturbations. The highest peak amplitude was obtained for simulations with high initial perturbation amplitude and a duct of FWHM $\approx$ 1.25 (Case-2, see table 7.1). Any further increase in the duct width resulted in a decrease in the peak bore amplitude for the simulation settings considered here. It should also be noted here that for the simulation amplitude, A $\approx$ 0.10, the peak amplitude obtained was roughly the same for all the duct widths considered here. This leads to the postulation that this amplitude may be considered a critical amplitude that is not affected by changes in the background ducting conditions for the simulation settings considered. For the lowest amplitude simulated, the response is such that there was an increase in the peak amplitude value with the duct width till a certain width, and then the peak amplitude starts to decrease.

Figure 7.6(d) shows the conditions for the formation of an undular bore and solitary wave. For the background conditions considered in the simulations, only the two low initial perturbation values (A $\approx$ 0.08,0.10) resulted in the formation of a bore for all the duct widths simulated, whereas for high initial amplitudes, depending on the duct width, the response of the system was either a solitary wave or a bore. Coincidentally, the solitary wave responses were obtained for the cases with higher initial amplitudes and narrow ducts. This could mean that the solitary wave response may depend on the strength of the system's nonlinearity. Laughman et al. (2009) also reported soliton-like responses for simulations under the conditions of high initial amplitude of perturbation and narrow duct which in their case was defined by a cosine profile in a deep domain where the vertical extent of the domain was at least 10 times larger than the one considered here. As mentioned before. the measure of nonlinearity of undular bores is given by the parameter $a\lambda^2/h^3$ (Lighthill, 1978; Dewan and Picard, 1998). This indicates that the degree of the nonlinearity of the system

depends inversely on the duct thickness. Hence this could explain the strong nonlinear responses obtained when the duct width was reduced indicating that the gradient of the stability profile plays an important role in supporting this behavior (Lighthill, 1978; Laughman et al., 2009).

7.2 Instability generation in dual ducts: Thermal and Doppler ducts

So far the bore generation investigation has focused on the thermal duct wherein the stability profile (N^2) is the background controlling parameter. But ducting is not governed only by N^2, however. The ducting conditions are governed by the dispersion relation for m^2 (Equation 2.27), of which N^2 is only one contribution. Also, observations by Fechine et al. (2009) and Bageston et al. (2011) have demonstrated the importance of velocity ducting for mesospheric bores. Additionally, Laughman et al. (2009) did a couple of numerical simulations using a single background velocity profile to understand the effects of velocity ducting on bore formation. Even though the results of Laughman et al. (2009) could not reproduce the structure of bores very clearly, it nevertheless served as a good demonstration of how the dynamics of the bore generation are affected due to background wind shear. The influence of the velocity ducting on bores and solitary wave

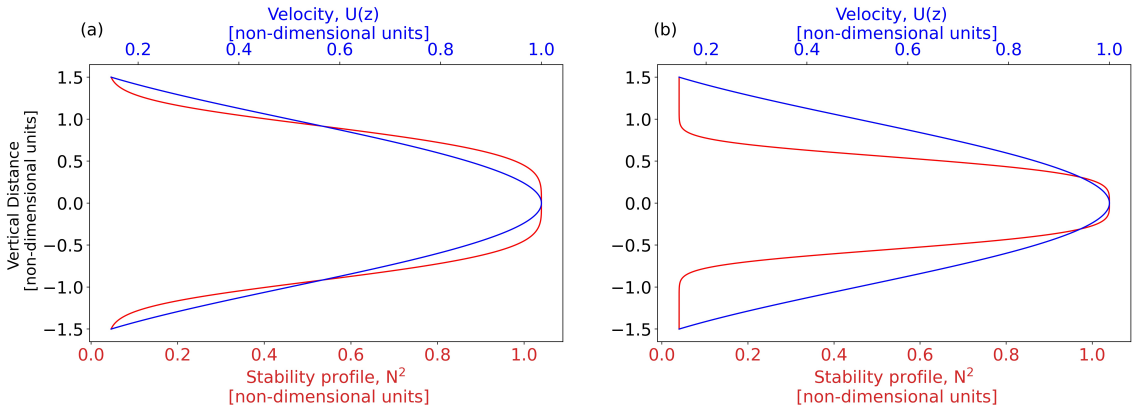


Figure 7.7: Dual Duct system where both Thermal (Red) and Doppler (Blue) ducts are present. (a) Thermal duct with FWHM ≈ 2.0 (Case-5), (b) Thermal duct with FWHM ≈ 1.0 (Case-1). Doppler duct is the same in both cases.

formation was investigated for many background velocity profiles, in addition to the already established background thermal duct. Figure 7.8 shows the comparison of the time evolution of the system with and without a Doppler duct. The left side of the figure shows the evolution of the bore when a constant wind background and thermal duct are applied while that on the right shows the same but when the simulation is also initialized with a velocity duct in addition to the

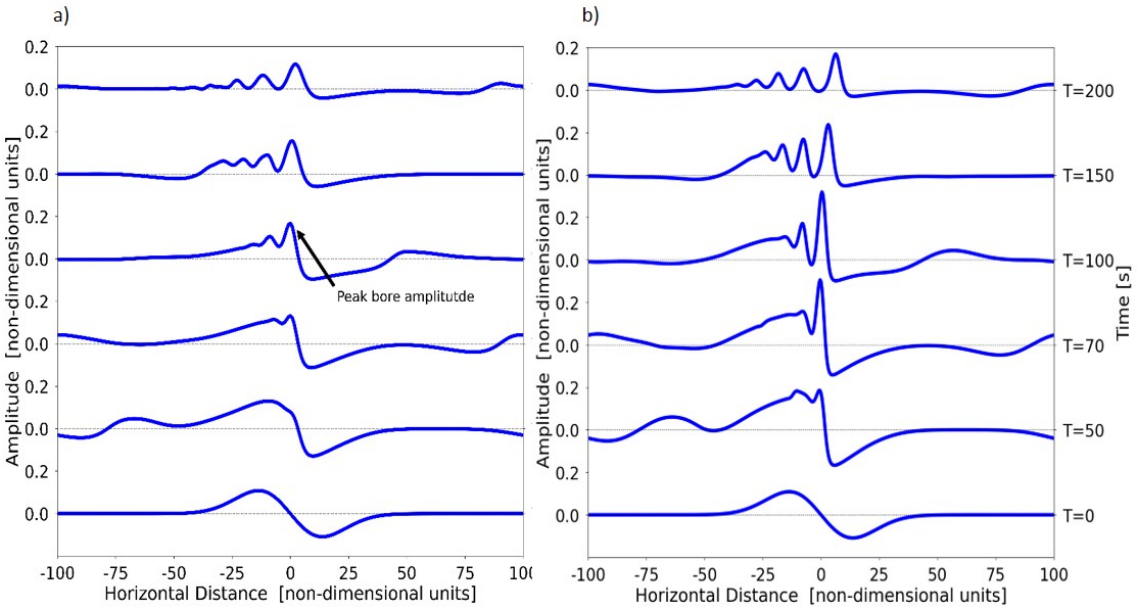


Figure 7.8: Time series of potential temperature traces for simulation cases for, a) Thermal-only duct (Case-5), and b) Thermal (Case-5) and Doppler duct shown in Figure 7.7(a)

thermal duct. In this section, this setting will be henceforth called a T+D simulation case. The thermal duct and the Doppler duct used are given in Figure 7.7(a). It becomes immediately apparent the effect the wind shear has on the bore morphology. Stark differences can be indeed seen concerning the nonlinear steepening, the time taken for the first peak of the wavefront to appear, the wavelength of the leading edge, the number of trailing undulations, and the dissipation of the entire bore structure. Both simulation settings had a ducted GW as initial perturbation with the same amplitude (A ≈0.10) at $T = 0\ s$. While the wave steepening, which takes place once the propagation has started, looks quite similar in both cases, some subtle differences in the wave structure can be quantified. For example, the steepness of the wavefront in the T+D simulation is higher than in the thermal-only case. This can be seen at time $T = 50\ s$ where both the simulations show a steepened wave, the T+D simulation also starts to display a hint of the peak formation of the wavefront which is the precursor to the bore formation. This peak formation occurs in the thermal-only case a little bit later ($T = 60\ s$, not shown).

Moreover, during the formative period of the bore, the wavelength of the leading wavefront is significantly different in the thermal-only case compared to the case where the Doppler duct is involved. We can also see that the leading edge of the wavefront is broader and has a longer wavelength in the thermal-only case. But it should also be noted here that as the bore evolves, the separation between the crests increases in both cases. Hence it can be said that the bore scales that arise are clearly dependant, in addition to the wavelength and the duct width, also on the back-

ground wind conditions. Moreover, the number of trailing undulations in the T+D simulation is noticeably more than (≈5) than in the thermal-only simulation (≈3). This presence of more trailing undulations could be because the wind shear which is given as a background condition also serves as an additional forcing to the system and this additional energy may help sustain more trailing waves. The peak amplitude attained by the bore after the initial nonlinear steepening in the T+D case is also much higher than in the thermal-only case. In the former case, the peak amplitude is close to 0.25 which is more than 2.5 times the initial amplitude and at least twice that of the peak amplitude obtained when the simulation is controlled by only a thermal duct. This again may be attributed to the Doppler duct acting as a forcing term which results in such high peak amplitude values. Not only does the Doppler duct affect the aforementioned parameters, but it also has an apparent effect on bore dissipation. At the time $T = 200\ s$, we can see that T+D case has at least twice the amplitude of the thermal-only case while nearing dissipation.

Figure 7.9 shows the contours of the flow field evolution of the thermal-only and T+D simulation. At time $T = 52\ s$, in the thermal-only case, the initial ducted wave is undergoing distortion while in the T+D case, the evolved peak of the wavefront is already evident. As the simulation proceeds, the formation of the trailing waves is evident in both cases while the separation between the crests is more apparent in the T+D case than in the thermal-only case. Besides this, the trailing waves in the T+D cases have a higher amplitude than in the thermal-only case which is noticeable in Figure 7.8. With time, more trailing waves are formed and they are phased-locked to the leading wavefront and start to drift away from the main wavefront. While Seyler (2005) reported the increase in the separation of the peaks with time in a thermal-duct simulation, which was also confirmed in our analysis, the same behavior is also observed when the Doppler duct is involved.

Chimonas and Hines (1986), Fritts and Yuan (1989), and Isler et al. (1997) have reported on the effects of the Doppler ducting mechanism in the MLT and how effective they are in trapping of GWs depending on their strength and the associated dynamics. By changing the magnitude of the background wind, in a way, we are also controlling the forcing due to wind shear on the bore formation and this can have significant effects on the bore and instability formation. Figure 7.10 shows the effects of changing the magnitude of the Doppler duct on the bore formation while keeping the thermal duct constant. Figures 7.10(a) and (b) show the evolution of the bore when the non-dimensional magnitude of the Doppler duct is around 1.0 and 0.5 which in physical dimensions is around $40\ m\ s^{-1}$ and $20\ m\ s^{-1}$. It is very clear how the different background wind shears affect the bore evolution in terms of bore peak amplitude and bore nonlinearity. At time $T = 40\ s$, the nonlinear steepening is observable in both cases but the wavefront has evolved to be steeper for the higher magnitude Doppler duct. It hence has resulted in a much narrower wavefront for the higher magnitude Doppler duct. The wavefront is, however, comparatively broader

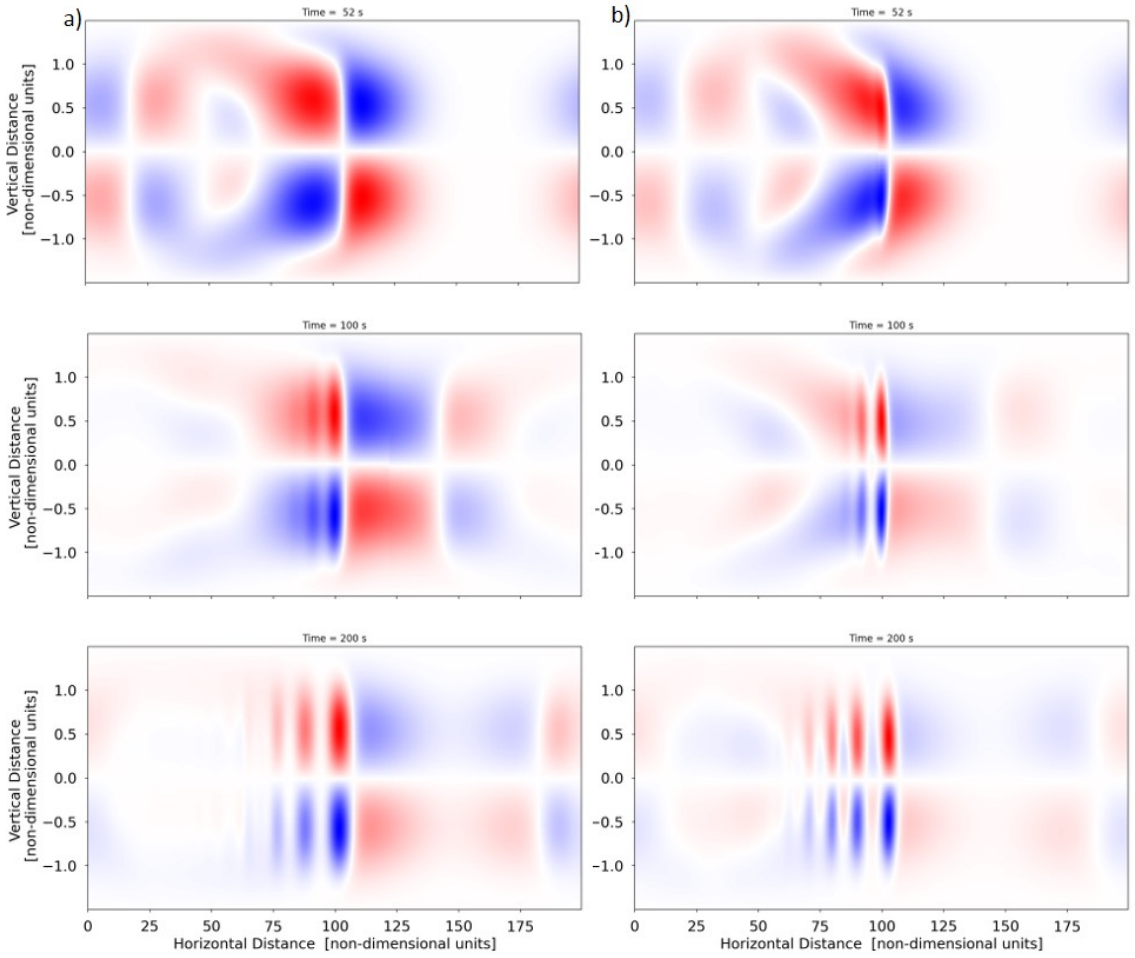


Figure 7.9: Contour plots of potential temperature evolution for a) Thermal-only duct, and b) Thermal and Doppler duct. Red indicates a positive value and blue indicates a negative value. Same as Figure 7.8.

for the lower magnitude Doppler duct. It is also interesting to note that no clear distinction can be made in terms of the horizontal wavelength of the main wavefront between the two cases. The trailing waves that were generated in the higher magnitude Doppler duct are more pronounced and hence more visible than the ones in the lower magnitude Doppler duct. This is established in the following time sequences: At time $T = 120\ s$, both cases have exactly one trailing wave following the main front but with different amplitudes. Then at time $T = 160\ s$ we see two well-defined trailing waves and at time $T = 200\ s$ there are three waves behind the main front for the higher magnitude case but only two for the lower magnitude case. Hence for a system with sufficient background wind shear, the bore can sustain itself for a longer time and subsequently result in more trailing waves than for a comparable system where the background wind shear is not strong (Fritts et al., 2020). Table 7.2 gives an overview of the effect of the initial amplitude

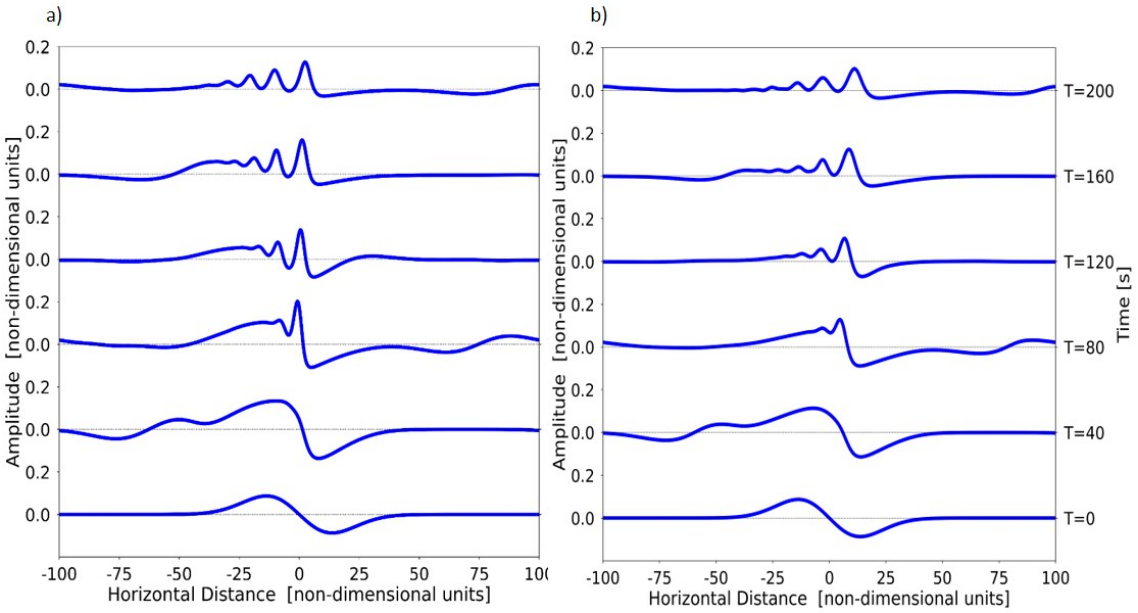


Figure 7.10: Time series of potential temperature traces showing the effects of the magnitude of the Doppler duct on the bore formation. (a) Doppler duct of magnitude of 1.0. (b) Doppler duct of magnitude of 0.5. Both the simulations have the wide thermal duct (Case-5)

of perturbation on formation time for thermal-only simulations and thermal and Doppler ducts. It can be inferred from the table that for simulations involving dual-ducting environments, the response time for the formation of the bore is much faster than for a thermal-only simulation for a particular amplitude. For higher amplitudes, this response becomes much faster as the time taken for the bore to form in a dual-ducting background is roughly half the time it would require for an equivalent bore formation in a thermal-only duct. Also shown in the table is the effect of initial amplitude on the nonlinearity, (i.e.) the peak bore amplitude. In both the thermal-only and dual-duct cases, the peak amplitude increases with the initial amplitude. But what is interesting is that the peak amplitudes in the dual-duct environment are at least twice that for the thermal-

Initial	Thermal duct		Thermal + Doppler duct	
Amplitude	Formation time (s)	Peak Amplitude	Formation time (s)	Peak Amplitude
0.08	74	0.11	54	0.22
0.10	64	0.17	46	0.32
0.13	60	0.23	34	0.41
0.16	56	0.27	30	0.6
0.18	48	0.37	26	0.62

Table 7.2: Simulation results showing bore formation time and the bore peak amplitude for different initial amplitudes of perturbation. The ducting profiles used are shown in Figure 7.7(a)

only case for all the simulated cases. This indicates that the response in a dual-duct system is more complex and strongly nonlinear leading to a stronger coupling and transfer of energy between the ducts (Laughman et al., 2009). This has been substantiated enough above (see Figures 7.8-7.10

7.2.1 Formation of secondary instabilities in dual ducts

So far, in the case of Doppler duct simulation, the associated thermal duct was chosen such that there was a definitive formation of the bore, As was previously investigated with thermal-only duct, the width of the thermal duct was reduced to match the conditions of solitary wave formation while retaining the Doppler duct. The profiles of the stability and background wind profiles are shown in Figure 7.7(b). In doing so, the resulting dynamics did not yield bores but rather a complicated system of bores, solitary waves, and associated secondary instabilities like the KHI. While the observations of mesospheric undular bores have been fairly reported in the literature ((Fritts et al., 2020) and the references within), related studies by Walterscheid et al. (1999), Walterscheid and Hickey (2011), Snively and Pasko (2003), and Snively and Pasko (2008) demonstrated the potential for GWs impinging on thermal or Doppler ducts to become trapped and exhibit instabilities like the KHI, secondary GWs, depending on the duct and GW parameters. Fritts et al. (2020) reported a recent observation of a twin mesospheric bore in the polar mesospheric clouds at an altitude of around 82 km. Both the bores were accompanied by a series of small-scale instability structures at the front and rear of the bores. They identified these structures as KHI billows with their orientation along the bore direction and their formation triggered by the GW breaking. Figure 7.11 shows the evolution of the system with a narrow thermal duct and a Doppler duct as shown in Figure 7.7(b) and a ducted initial wave. The vertical domain has been extended to exclude the effects of boundaries on the flow evolution. Immediately after the initialization, at time $T = 20\ s$ we can see the rapid evolution of the initial wave forming a sharp "tilted" front in comparison to the straight fronts in the previous cases. The trailing end of this front gives rise to an overturning vortex resembling a KHI billow that is advected upwards from the main front and is cut off from the wavefront. As the wavefront further evolves, at time $T = 56\ s$, we see that primary KHI has dissipated and the wavefront has intensified leading to a secondary front. This secondary front initiates the formation of additional billows that are larger than the primary instability structure. The horizontal scales of these billows are about 10 km with the vertical scale being close to 3 km which corresponds to the instability structures reported by Fritts et al. (2020) and Chau et al. (2020). The billow instability structures have advected behind as the primary wavefront further propagates. The horizontal and vertical scales of the secondary billows at time $T = 68\ s$ have reduced considerably implying dissipation of the structures. Small-scale

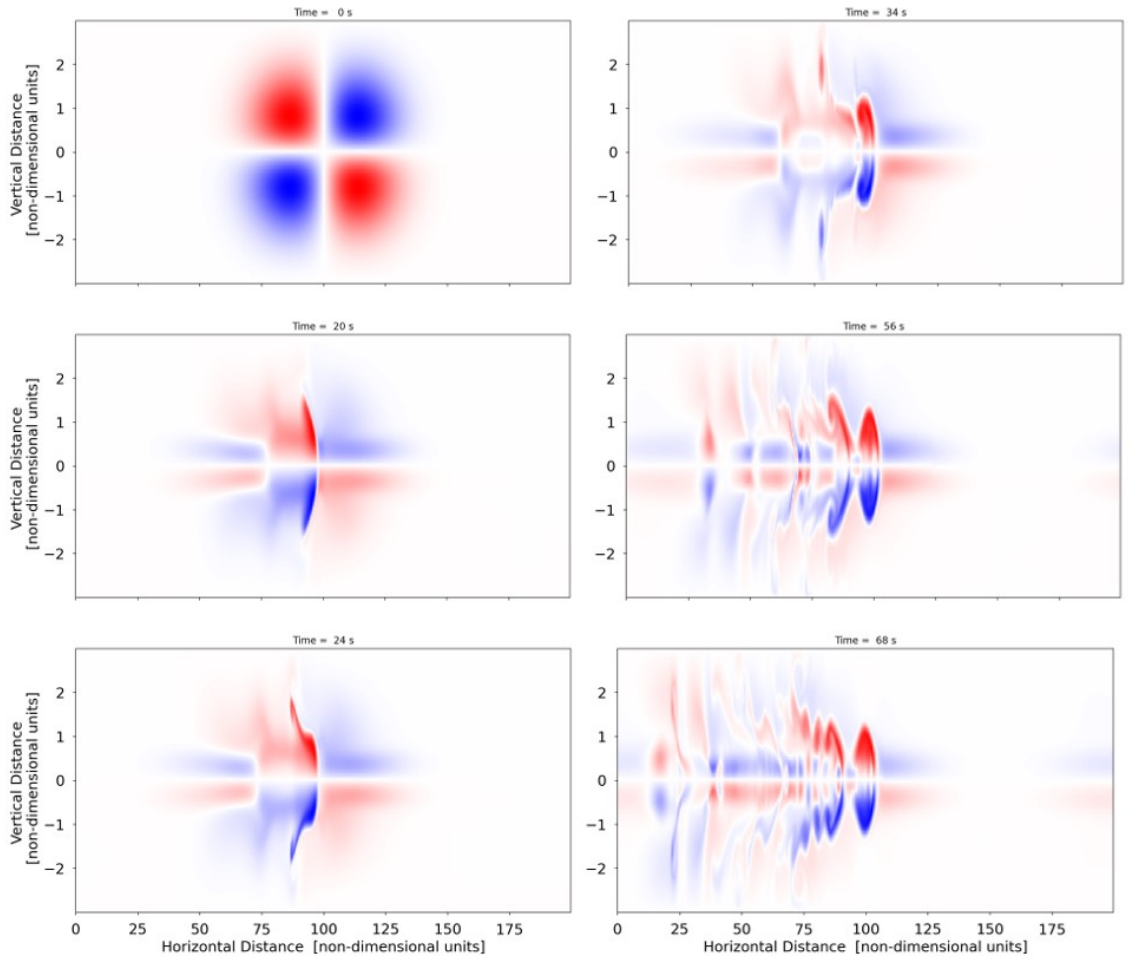


Figure 7.11: Contour plots showing the formation of secondary instabilities in a thermal Doppler system shown in Figure 7.7 (b).

turbulent structures fill the far field of the flow domain indicating the breaking of the GWs and billow structures (Fritts et al., 2020). Several of the reported features of this simulation closely resemble the observations like The generation of the small-scale KHI billows at the leading and the trailing edge of the bore, the scales of the billows, and a reduction in their scales with time (Fritts et al., 2020). The above response of instabilities accompanying the bores could be the result of the reduced stability (narrow thermal duct) away from the duct center. However, a narrow thermal duct alone did not lead to the formation of instabilities in the case of constant background wind (See Figure 7.4). Hence what could cause the instability dynamics reported here? The answer is the addition of a Doppler duct in a way that its influence dominates that of the thermal duct. If the Doppler duct overlaps the thermal duct, as shown in Figure 7.7(a), then the stability of the duct provided by the thermal duct inhibits the generation of instabilities (Fritts et al., 2018; Fritts et al., 2020; Fritts et al., 2023). The time evolution shown in Figures 7.8 and 7.10 imply that such a sys-

tem results in undular bore formation. However, if the Doppler duct lies outside of the influence of the thermal duct as shown in Figure 7.7(b), the resulting evolution is a complex environment that is characterized by multi-scale dynamics of instabilities and bores. Hence for instabilities to form along with bores, the background conditions should be controlled by both temperature and wind.

7.2.2 Formation of solitary waves in dual ducts

It was discussed in the preceding section on the formation of secondary instabilities accompanying the bores when the thermal duct width was reduced to be narrow with background wind shear. However, the background conditions considered did not yield a pure solitary wave response like the ones we obtained in the pure thermal duct condition which is shown in Figure 7.4. Hence, we investigated further under which background conditions, both thermal and Doppler duct, could solitary waves be generated. Figure 7.12 shows two background conditions that were investigated where the thermal duct is narrow and the Doppler ducts have two different magnitudes. The Doppler ducts in this particular case were chosen to be fully enveloped with the thermal duct so that the flow inside the duct may not be affected by instabilities. The reason for this investigation

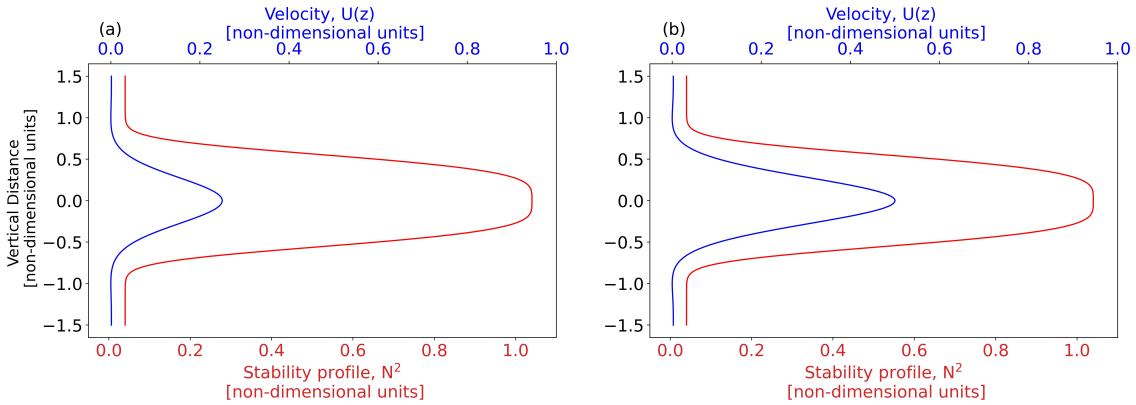


Figure 7.12: Dual Duct system where both Thermal (red) and Doppler (blue) ducts are present. The Doppler ducts are fully enveloped inside the thermal duct. Two different Doppler ducts with different magnitudes were investigated. Thermal duct considered is a narrow duct (Case-1).

is due to the motivation to understand the formation and eventual dynamics of a one-of-a-kind observation that was reported by Chau et al. (2021). They concluded, based on the horizontal and vertical spatial structures of their observation, that it showed characteristics that resemble a solitary wave behavior in varicose mode. In their observation, there was also the presence of at least two small trailing undulations when this extreme event was observed. Due to the absence of any

temperature or density data available at the time of the observation, they could not comment on the presence of a thermal duct. However, the availability of the wind data shows that a strong wind shear of at least 20 m/s was present during the event. Hence it is clear that the wind shear may have had a role in the extreme event (Chau et al., 2021). Since it was already established that a duct of narrow width with an initial perturbation of sufficient amplitude will result in a solitary wave formation, it needs to be investigated as to whether a wind shear background condition will alleviate or mitigate this.

Figure 7.13 shows the traces of potential temperature evolution that has resulted from the background conditions with a narrow thermal duct and Doppler ducts fully bounded with the thermal duct and an initial amplitude of perturbation, A $\approx$ 0.16. This is the same amplitude initial perturbation that resulted in a solitary wave in the narrow thermal duct simulation. It can be seen that both the systems retain the formation of the solitary wave in the case where both thermal and Doppler ducts are considered although with noticeable differences between the two setups. It is apparent, in both cases a single high-amplitude peak is formed at time $T = 40\ s$ which is reminiscent of the sharp peak that was also obtained in the solitary wave case of the thermal-only duct (see Figure 7.4). The higher magnitude case (0.5) shown in Figure 7.13(b) has a more rapid and stronger response at this time than the lower magnitude case (0.25). The higher magnitude case also shows signatures of a trailing wave at time $T = 40\ s$ which is absent in the lower magnitude case. The peak amplitudes of the solitary waves are $\approx$ 0.5 (Doppler duct magnitude 0.5) and 0.38 (Doppler duct magnitude 0.25), respectively. The rapid response and the higher peak amplitude of the system are clearly due to the stronger background wind. As in the case of undular bore formation, the peak amplitude is higher for the Doppler duct having a higher magnitude. As the evolution proceeds, in both cases we see the formation of very small-scale trailing undulations at times $T = 70\ s, 80\ s, 90\ s$, following the main peak which was completely absent in the thermal-only case. Once the wavefront reaches its peak amplitude and starts losing its energy, the trailing waves also start dissipating its energy and eventually disappear. It is interesting to note that the trailing undulations in both the simulated cases above, move independently as a separate wave packet from the main wavefront (see at time $T = 120\ s$). The distance between the trailing waves, however, is roughly constant while they drift away from the main wavefront. This is also clearly evident in Figure 7.14 which shows the contours of the flow field evolution for these two simulated cases. The formation of a peak followed by trailing waves at $T = 110\ s$ which then move independently away from the main wavefront with different wavelengths can be readily quantified in Figure 7.14. This soliton behavior is different from what we have observed before in the cases of undular bores where the trailing waves are phase-locked to the leading wavefront. Consequently, we can infer that despite the presence of trailing waves, their dynamics do not align with the anticipated behavior of an undular bore; rather, they align more closely with that of a soliton.

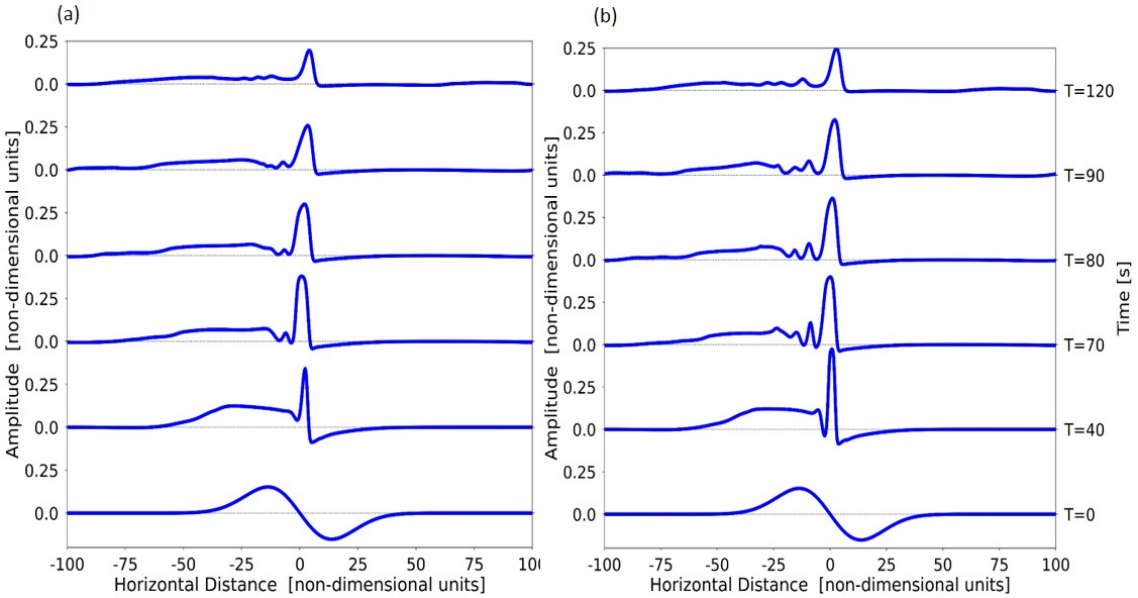


Figure 7.13: Time series of potential temperature traces for simulation cases with both thermal and Doppler ducts shown in Figure 7.12. Doppler ducts have magnitudes of 0.25 and 0.5

Nevertheless, these two cases prove that under certain conditions when the background is influenced by both thermal and Doppler ducts, the morphology of the resulting system resembles that of what was reported by Chau et al. (2021).

Table 7.3 shows the results of the simulations for different initial amplitudes with thermal-only (narrow duct) and dual-duct shown in Figure 7.12. Since these profiles yielded solitary wave responses for certain initial amplitudes of perturbation, we wanted to investigate how the nonlinearity is affected upon including the background wind shear. In this case, as with the wide duct case, there is a clear difference in the time taken for the bore to form and the peak amplitude between the thermal-only and dual-duct environments. The dual ducting environment results in a faster response of the initial wave steepening as is shown in Figures 7.13-7.14. It is interesting to note that the difference in the bore formation time between the two ducting environments decreases as the initial amplitude increases. Furthermore, a clear distinction in the peak amplitude of the bore between the two cases can also be seen. For low amplitude perturbation cases ($A \approx 0.08, 0.10$), the peak bore amplitude in the dual-duct cases is roughly twice that of the thermal-only case whereas for the higher amplitude cases, the values are in the same order of magnitude, albeit still higher for dual-duct cases. This indicates that in the limit of high amplitude GW, even though there is not a substantial difference in how the system reacts to the two ducting cases, the dual-ducting environment may give rise to even more complicated dynamics due to the interplay and stronger coupling between the two ducts as was shown in Figure 7.14-7.16 (Lighthill, 1978;

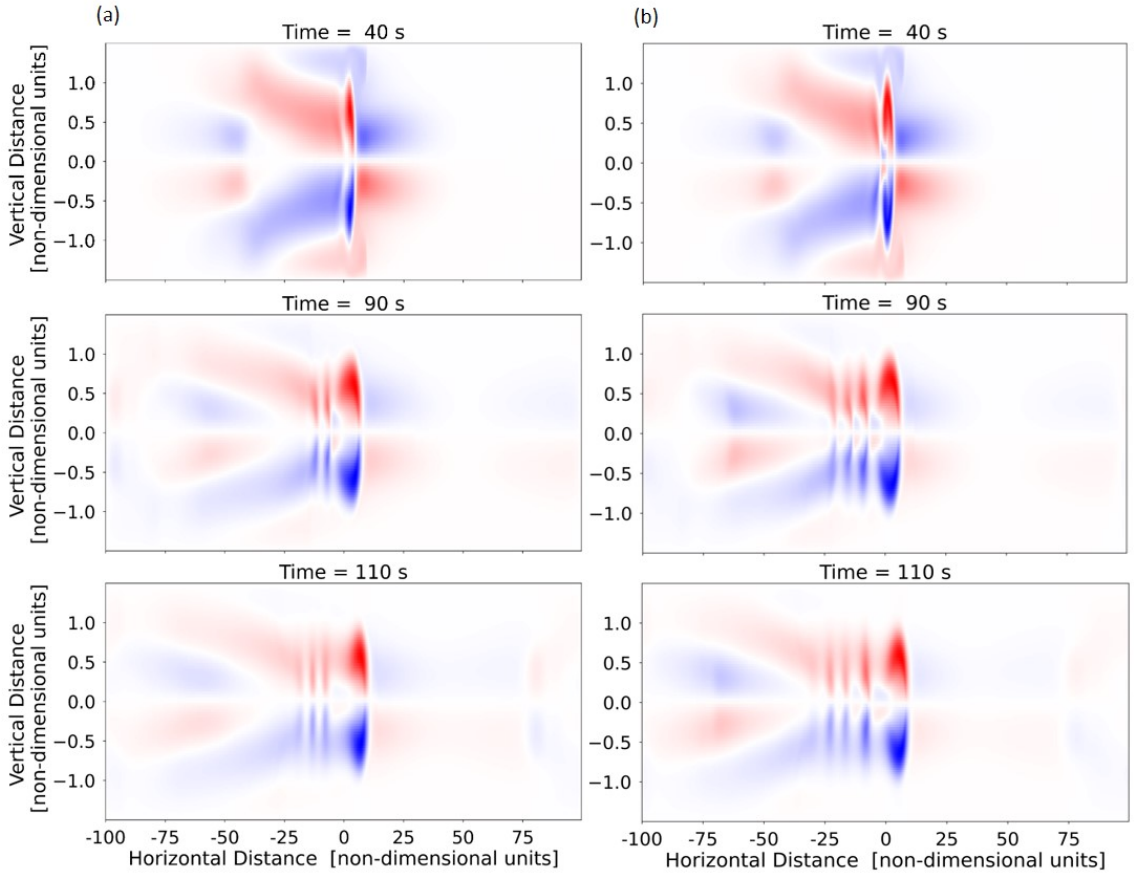


Figure 7.14: Contour plots of potential temperature on the solitary wave formation with thermal and Doppler ducts shown in Figure 7.12. Same as Figure 7.13

Fechine et al., 2009; Laughman et al., 2009).

7.3 Generation of instabilities in vertically displaced ducts

In the MLT, the likely ducting environments are significantly induced by the GW motions and result in significant velocity and stability variation across the GW phase (Laughman et al., 2009). These results in potential Doppler and thermal ducts that may have relative vertical displacements that depend on the orientation of the perturbation and such systems can exhibit radically different behavior from single isolated ducts or even overlapped ducts (Fechine et al., 2009). We examine here the cases of background conditions where the two superpose ducts have varying degrees of separation. Since two ducts do not envelope one another, it should be expected that the response

Initial	Thermal duct		Thermal + Doppler duct	
Amplitude	Formation time (s)	Peak Amplitude	Formation time (s)	Peak Amplitude
0.08	52	0.06	36	0.14
0.10	42	0.17	32	0.30
0.13	38	0.31	28	0.40
0.16	36	0.37	26	0.45
0.18	32	0.41	24	0.49

Table 7.3: Simulation results showing bore formation time and the bore peak amplitude for different initial amplitudes of perturbation. The ducting profiles used are shown in Figure 7.12(b)

of the resulting system is more asymmetric which is different from the cases mentioned earlier which are symmetrical.

Figure 7.15 shows the result of the simulation where the thermal and Doppler ducts were vertically displaced from one another. The nonlinear process of distortion of the initial wave (wave steepening) at time $T = 10\ s$ is entirely different from the previous cases as the initial response is very asymmetrical with the phase shift of their peaks. This is to be expected since the ducts do not overlap which will lead to a more asymmetric response. As the simulation progresses at time $T = 30\ s$, we can see the formation of peaks resembling the wavefront in both the upper and lower layers about the center of the domain. The structure in the upper layer extends vertically to a greater degree than the corresponding one in the lower layer with the formed peak clearer in the upper layer. This could be due to the predominance of the Doppler duct in the upper half of the domain and being negligible in the lower half. At later times $T = 70\ s, 100\ s$, the formation of a clear front is visible with the formation of trailing waves. However, due to the nature of the placement of the Doppler duct, there are additional structures that are present in the upper domain that are absent in the lower part of the domain.

These resemble overturning structures with their horizontal scales equivalent to that of the front and they exist outside of the thermal duct. Since a part of the Doppler duct, which is more of a dynamic background condition, lies outside of the thermal duct this may lead to the interaction of the background flow with the wave yielding these unstable structures. The trailing waves that start to form appear also to possess more intensity in the upper layer compared to the lower layer due to the relative position of the ducts. The stronger response in the upper layer could also be due to the stronger coupling between the two ducts hence allowing for more energy transfer between them than in the lower layer (Laughman et al., 2009; Fritts et al., 2020). Fechine et al. (2009) and Bageston et al. (2011) have reported observational evidence of mesospheric undular bores in thermal-Doppler ducts where the thermal and Doppler ducts are displaced vertically from one

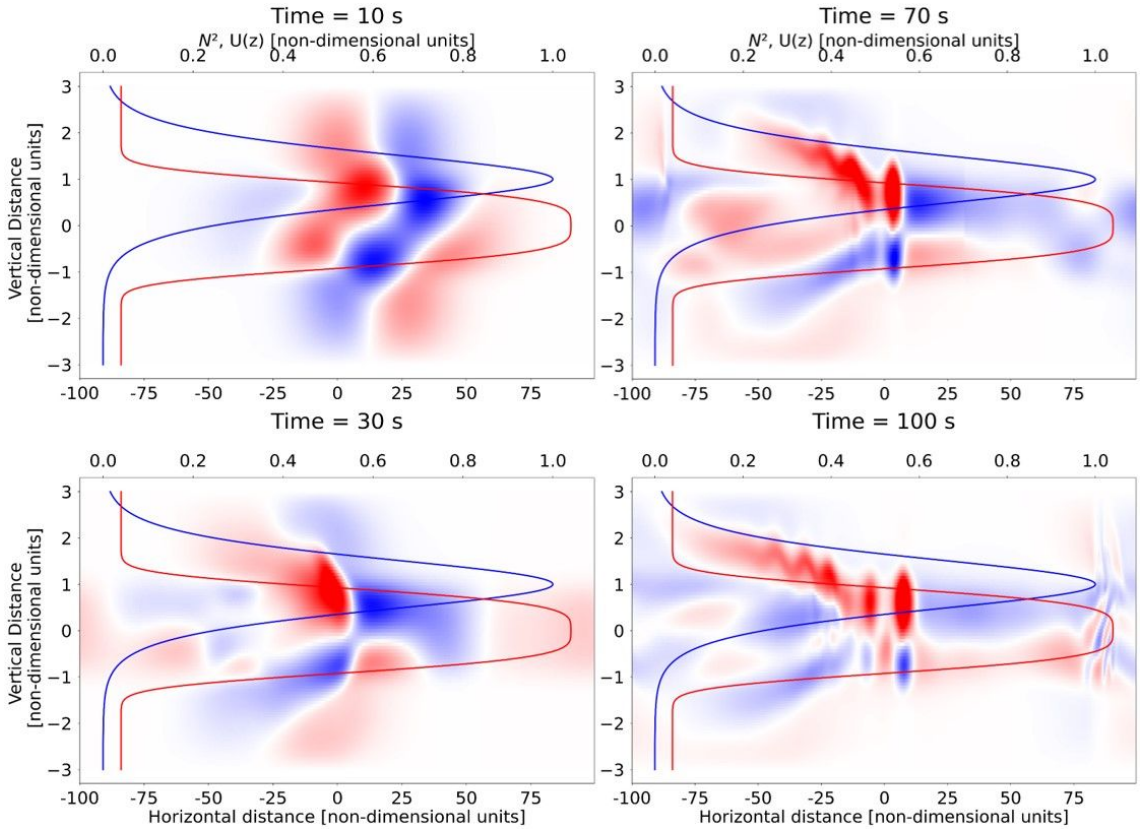


Figure 7.15: Contour plots of potential temperature evolution for the vertically displaced dual duct system. The red and the blue lines indicate the thermal and the Doppler ducts, respectively. The Doppler duct has been vertically displaced by a factor of 1 with respect to the thermal duct. The initial perturbation is centered around the thermal duct.

another and have different strengths. These potential thermal-Doppler ducts arise due to the GW motions that induce significant velocity and stability variation as they propagate. The results presented above indicate that for adjacent ducting structures, the response is highly nonlinear and variable in space and time and departs in significant respects from the responses arising due to simpler ducting structures and they may not always be readily observed even if their occurrence is frequent (Laughman et al., 2009).

7.4 Effect of viscosity on instability formation

According to the bore theory of Dewan and Picard, the loss of energy from the bore is either of the following processes; The energy lost by the bore will reappear in the form of trailing undulations,

the energy is removed by viscosity or the energy is radiated away from the duct due to reduced duct stability. We have seen evidence of energy loss due to trailing wave formation in the previous sections. The rate at which the bore loses its energy can be obtained by calculating the rate at which trailing waves appear. However, the effects of viscosity are always predominant and cannot be neglected. Walterscheid and Hickey (2011) calculated the kinematic viscosity as a function of altitude and found its exponential increase in the MLT region. This further tells us that even if we consider a small altitude region, the effects of viscosity and diffusion are so significant that they cannot be neglected. The first numerical modeling effort of Seyler (2005), although included the effects of viscosity, did not include the diffusion process in the energy equation. This poses a problem when one considers the coupled system of equations where the potential temperature is coupled with the vertical velocity in the Navier-Stokes equation and the vertical velocity, *w* is multiplied with the Brunt frequency in the energy equation. If we use the potential temperature as a passive scalar which does not have any influence on the flow itself, then the approach taken by Seyler (2005) to model the bores can be justified. However, we have already established the effects of stability and consequently, the temperature on the bore formation. Hence the approach that includes both viscosity and diffusion in our modeling attempt is also justified. The effect of viscosity on the bore formation was tested for cases with constant background wind and Doppler duct.

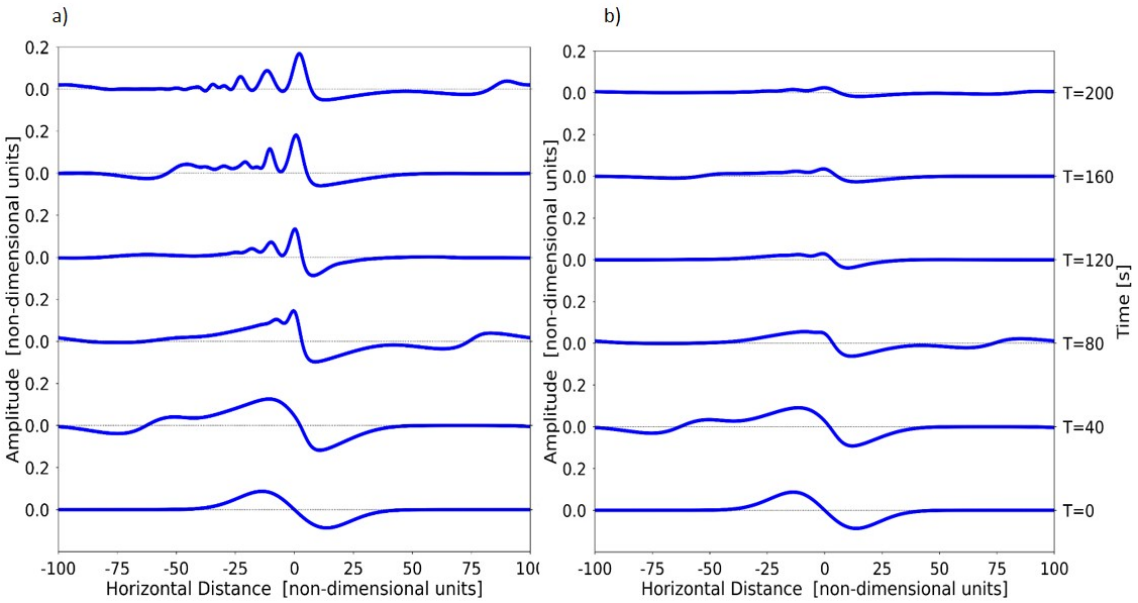


Figure 7.16: Time series of potential temperature traces for simulation cases for thermal-only duct (Case-5) with a) Viscosity of $5\ m/s^2$, b) Viscosity of $15\ m/s^2$

.

Figure 7.16 shows the effects of the viscosity on the bore formation for an initial amplitude of ≈

0.10, under thermal duct and constant background wind conditions. The thermal duct considered is a wide duct, Case-5. Figure 7.16(a) is the low viscosity ($5\ m/s^2$) and Figure 7.16(b) is the high viscosity ($15\ m/s^2$) simulation. The viscosity values that were considered were around the values that one would find in the altitude range of 80-90 km and this is also the region where most of the bore observations have been reported. For a high viscosity value, there does not seem to be a hint of any formation of the bore even though the nonlinear steepening process which is a precursor to the bore is evident at time $T = 40\ s$. It is interesting to see that even though there is no stark difference in the amplitude of the wave during the nonlinear steepening for different viscosities, it seems that the response of the system after this initial process is determined by the viscosity, on whether it leads to bore formation or simply the energy being removed from the system. Viscous damping has attenuated the peak amplitude significantly. The peak amplitude attained in the high viscosity case is less than the initial amplitude of perturbation. When the viscosity is high, after the initial nonlinear process although there is a formation of a wavefront ($T = 120\ s$), it is not a well-defined sharp peak and there is also no hint of any presence of the trailing undulations. Even at later times, one could see that the wavefront itself has lost its energy and this loss in energy is not translated into additional trailing undulations. This means that the viscosity is removing the energy at a rate faster than for the bore to lose its energy via the formation of more trailing waves (Seyler, 2005). Concurrently, it was already established in Figure 7.6, that if the amplitude of initial perturbation is higher then it will result in a higher peak amplitude. Hence it can be said that even if the viscosity is acting to remove the energy thereby inhibiting the peak formation, if the amplitude of the initial perturbation is sufficient enough, then it may result in a stronger bore response.

In contrast, for simulations involving lower viscosity value (Figure 7.16(a)), there is a noticeable difference in the peak bore amplitude, number of trailing undulations, and dissipation. Here, we can very clearly see the nonlinear steepening of the initial wave that evolves into a wavefront between times $T = 40\ s$ and $T = 80\ s$ and trailing waves start to form behind the main wavefront. The amplitude of the leading wavefront is significantly larger (at least 3 times) than the higher viscosity simulation. Small wave-like fluctuating structures develop at time $T = 200\ s$ which could be the result of turbulent motions starting to develop due to viscosity not being sufficient to dampen these fluctuations. The spatial scale of these structures is very small compared to the dominant bore front and its trailing waves and they are incoherent in their morphology.

The behavior of the system in the presence of background wind shear (i.e.) Doppler duct (Doppler duct given in Figure 7.7(a), follows a similar pattern concerning bore formation as above which is shown in Figure 7.17. Both cases result in the apparent nonlinear steepening at time $T = 40\ s$,

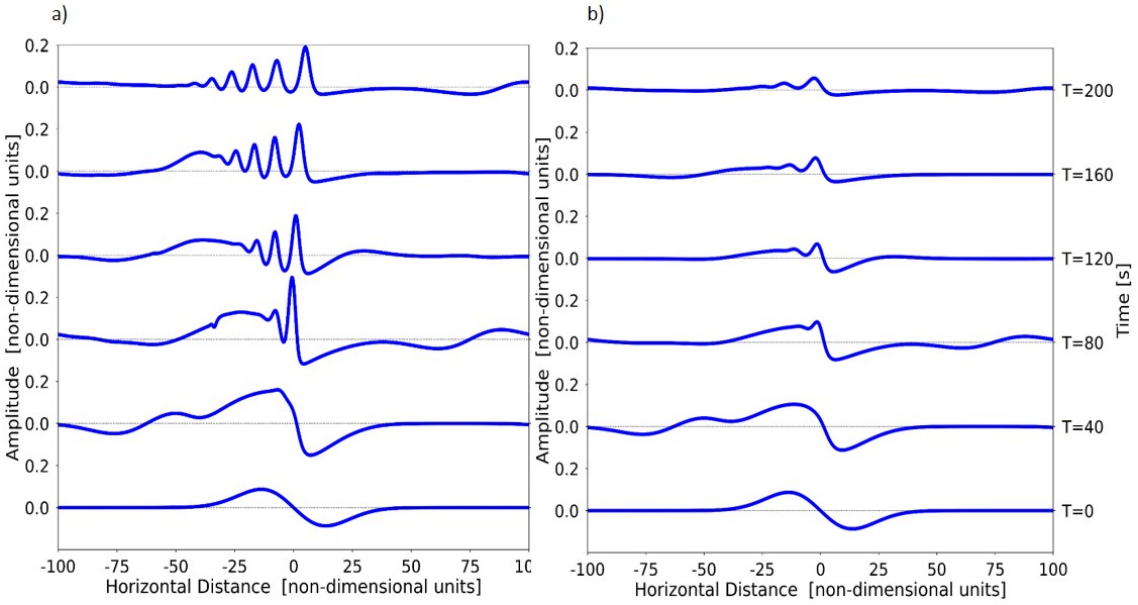


Figure 7.17: Sequence of line traces of potential temperature for simulation cases in the dual-duct system shown in Figure 7.7(a) with a) Viscosity of $5\ m\ s^{-2}$, and b) Viscosity of $15\ m\ s^{-2}$

with the response being stronger for the low-viscosity simulation. However, compared to the constant wind background, the high viscosity case which is shown in Figure 7.17(b), also yields a bore response which can be attributed to the wind shear acting as a forcing rather than viscosity being ineffective when background wind is variable. We can also see at least one trailing wave being formed being the main wavefront, at time $T = 160\ s$, which is not present in the constant background case. The peak amplitude of the wavefront is roughly the same as the initial amplitude (A $\approx$ 0.11). Hence, it means that even though nonlinear steepening does not result in an increased peak amplitude, the background wind shear acts to induce trailing waves. When the viscosity is lower (Figure 7.17(a)), the formation of the sharp peak following the nonlinear process is rather rapid compared to when the viscosity is higher. This means that, in the limit of low viscosity, the nonlinear process that gives rise to the wave steepening, and the process of transferring energy due to this nonlinear process is more rapid yielding a faster formation of the bore. Moreover, for simulation runs with low viscosity, there is also an increase in the number of trailing undulations. Since viscosity is a major factor in removing the energy from the flow, in the case of negligible viscosity, the available energy that is present that would have been otherwise dissipated, results in the formation of more trailing waves. The contour plots in Figure 7.18 show the formation of trailing wave crests and is phase-locked to the main wavefront. They span the entire layer of the duct and are also much sharper and narrower (also see Figure 7.17(a)).

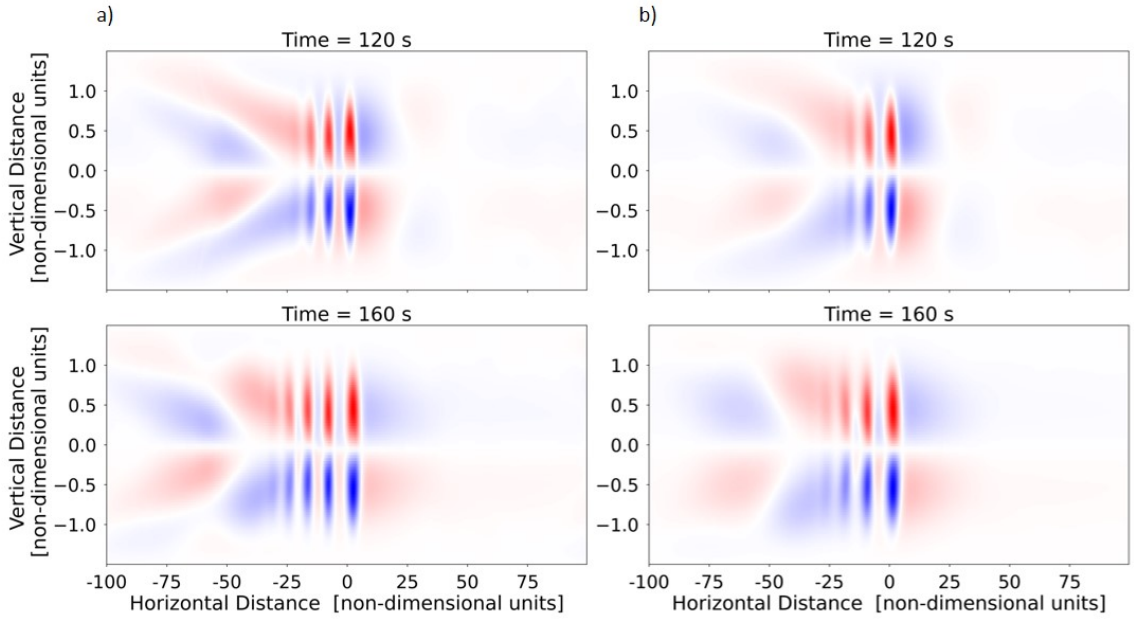


Figure 7.18: Contour plots of the effects of viscosity on bore evolution with both thermal and doppler ducts a) Viscosity of $5\ m\ s^{-2}$, and b) Viscosity of $15\ m\ s^{-2}$. Same as Figure 7.17

7.5 Effect of the inversion layer magnitude

It has been well-established here and in the literature, the effects of the thermal duct on bore formation (Dewan and Picard, 1998; Smith et al., 2003; Smith et al., 2017). The thermal duct is formed due to the presence of a temperature inversion layer, which occurs when the decreasing temperature with altitude has a local minimum and inverts and increases with height for a certain altitude range. Fritts et al. (2018) investigated the effects of the mesospheric inversion layer and the effects of upwards propagating GWs encountering it. They concluded that the inversion layers can cause large-amplitude GWs to yield instabilities and turbulence while the smaller-amplitude waves, although might not lead to instabilities and turbulence, do exhibit partial reflection and transmission. Fritts et al. (2018) also reported the effects of the strength of the inversion layer on the trapping of GWs where a stronger inversion layer led to the full trapping of the GWs with minimal transmission or reflection while a weaker inversion layer tends to allow for greater transmission of waves with only a fraction of the GW energy being trapped inside the inversion layer. Since the initial simulation setting considered in this thesis is already a GW that is trapped inside the duct that may evolve into a bore, by controlling the strength of the background stability profile (its magnitude value), we can investigate the effects of the inversion layer strength on the bore formation. The stability profiles used here are shown in Figure 7.19 where the magnitude of one of the stability profiles is a quarter of the other one. Since the ducts may exist as coupled systems

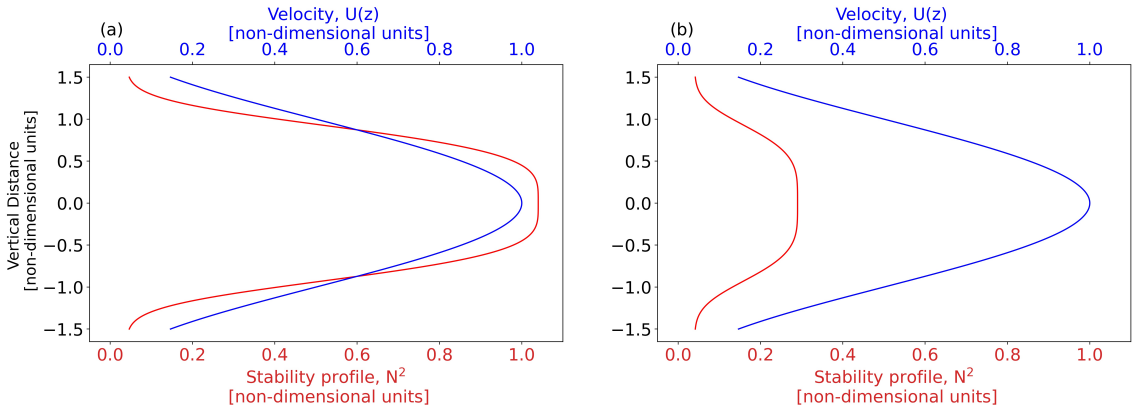


Figure 7.19: Profiles of Doppler duct and a) Thermal duct of magnitude 1.0, b) Thermal duct of magnitude 0.25

with thermal and velocity ducts (Fechine et al., 2009; Laughman et al., 2009), this investigation was done under both constant and variable wind backgrounds by including a Doppler duct.

Figure 7.20 shows the evolution of the two systems which were initialized with stability profiles of two different magnitudes and constant background wind. Both the simulation cases were initialized with the same amplitude gravity wave in ducted mode. There is a fundamental difference in how the system evolves depending on how strong the inversion layer is. Figure 7.20(a) shows the evolution of a system for a maximum background stability value of 1.0 while Figure 7.20(b) is for a value of 0.25. The state of the system evolution in both cases follows the theory of bores where the initial wave follows the nonlinear wave-steepening process before forming a sharp peak wavefront. But what is interesting is the time it takes for this wavefront to form in both cases. For the low stability profile case, the steepening of the initial wave and the subsequent formation of the dominant sharp peak happens between $T = 80\ s$ and $T = 100\ s$ whereas, in the high stability case, the nonlinear steepening is almost immediate at time $T = 40\ s$ with the traces of dominant peak starting to be seen at around time $T = 80\ s$. In addition to the effects that the background stability profile has on the nonlinearity and the formation of the wavefront, it also has a considerable impact on the peak bore amplitude, the wavelength of the undulations, and the number of trailing undulations. In the case of low stability simulation, the number of trailing undulations that were present approximately 2/3 through the simulation run was just one whereas in the high stability case, there are already two well-established trailing waves at the same time with traces of more forming. Moreover, the peak amplitude of the bore that was obtained in the high-stability (A $\approx$ 0.11) case was at least twice the value of the low-stability case (A $\approx$ 0.06). Since the horizontal wavelength also depends on the nonlinear steepening process (Lighthill, 1978; Laughman et al., 2009) and we have already established that the low stability case is not strongly nonlinear compared to the high stability case, it follows naturally that the horizontal wavelength of the longest

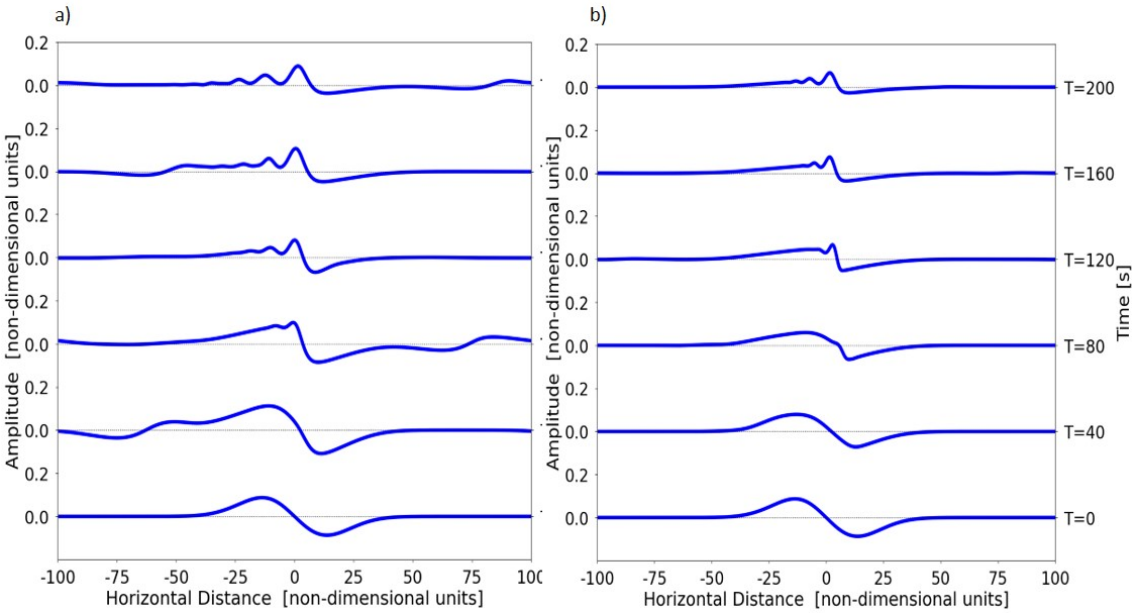


Figure 7.20: Sequence of line traces of potential temperature for simulation cases initialized with constant background wind for (a) Thermal duct of magnitude 1.0 and (b) Thermal duct of magnitude 0.25.

undulation is less than for high stability case. The horizontal wavelength was determined approximately 2/3 through the way of the simulation once the system reached a steady state. The reason for the difference in the morphology of the bores between the two cases could lie in the fact that for a weaker inversion layer, the amount of GW energy that is trapped by the inversion layer is not sufficient for the bore to form, due to the leakage of wave energy away from the duct (Fritts et al., 2018). The flow field evolution of the potential temperature shown in Figure 7.21 shows how the trapping of the GW inside the duct results in bore formation which follows the results reported by Fritts et al. (2018). For a higher stability duct which is shown in Figure 7.21(a), at time $T = 80\ s$, we can see the trapped GW that is already showing the signature of peaks while in the lower stability duct, at the same time, the initial wave is undergoing distortion and radiating away the energy from the duct. At later times, $T = 120\ s, 160\ s$, the bore in the higher stability duct is already well-defined with a well-formed wavefront and trailing waves are also evident while radiating away little of its energy away from the duct. At an equivalent time, the lower stability duct indicates the formation of the wavefront and at the later time shows the formation of one trailing wave with much of its energy being radiated away to the surrounding.

In the discussion above on the inversion layer strength on the bore formation, the background wind was taken to be constant. To emulate realistic atmospheric conditions, the background should be taken to represent varying wind conditions and to that effect, the Doppler duct was

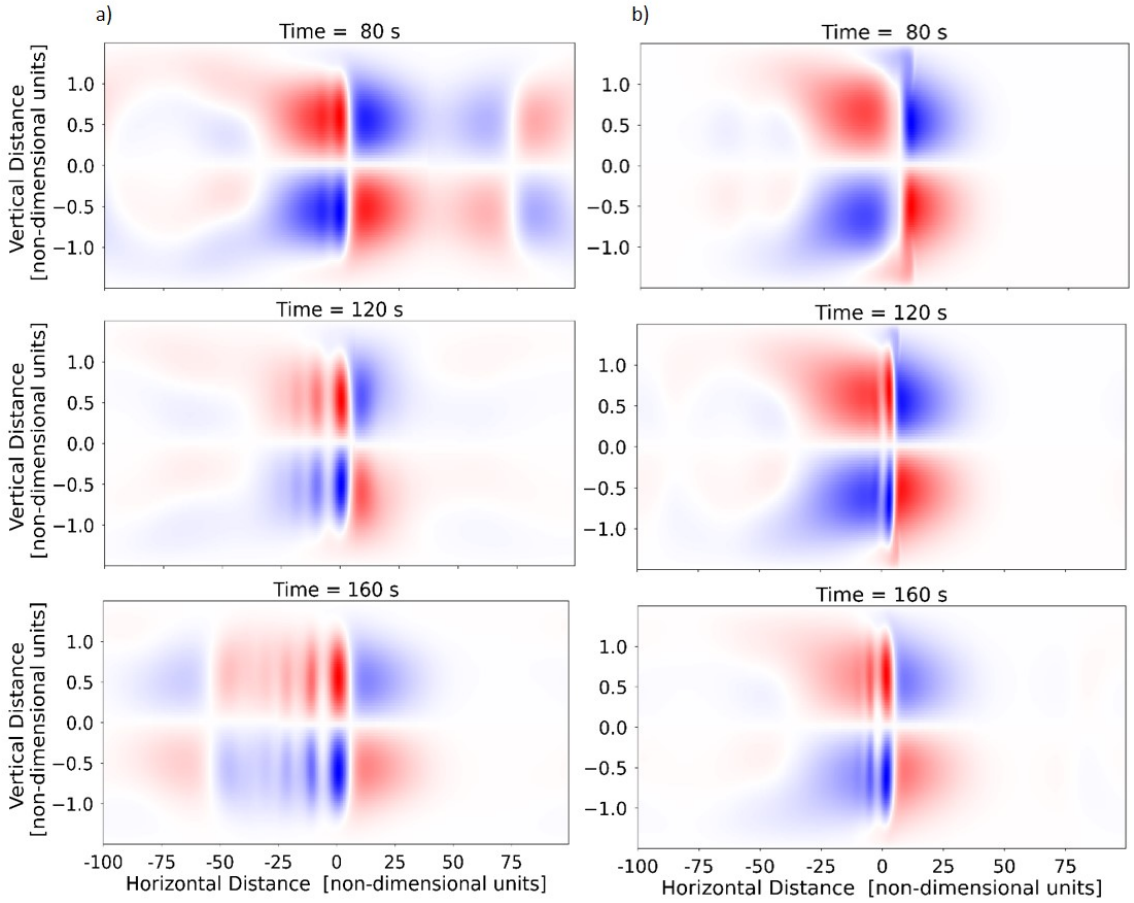


Figure 7.21: Contour plots of potential temperature evolution for constant background wind and a) Thermal duct of magnitude 1.0 and b) Thermal duct of magnitude 0.25. Red indicates a positive value and blue indicates a negative value. Same as Figure 7.20

added to the already existing thermal ducting condition (See Figure 7.19). As a result, the system is initialized with a ducted gravity wave in an environment that is controlled by a complex ducting structure involving both varying temperature and wind profiles. Figure 7.22 shows the evolution of the system in the presence of both thermal and Doppler ducts. Distinct differences can be seen in how the system evolves in this case compared to when the background is controlled by only temperature. The system with the higher stability profile, Figure 7.22(a) does result in a nice formation of the wavefront resulting from the nonlinear process at time $T = 50\ s$ and the subsequent formation of the trailing undulations. The distance between the successive crests also increases with time as the bore evolves which is consistent with the results of Seyler (2005) and Laughman et al. (2009). On the other hand, the low stability profile case, Figure 7.22(b), yields interesting dynamics. While there is a clear formation of a peak formation in the low stability case at time $T = 50\ s$, the similarity of the morphology with the high stability case and other reported

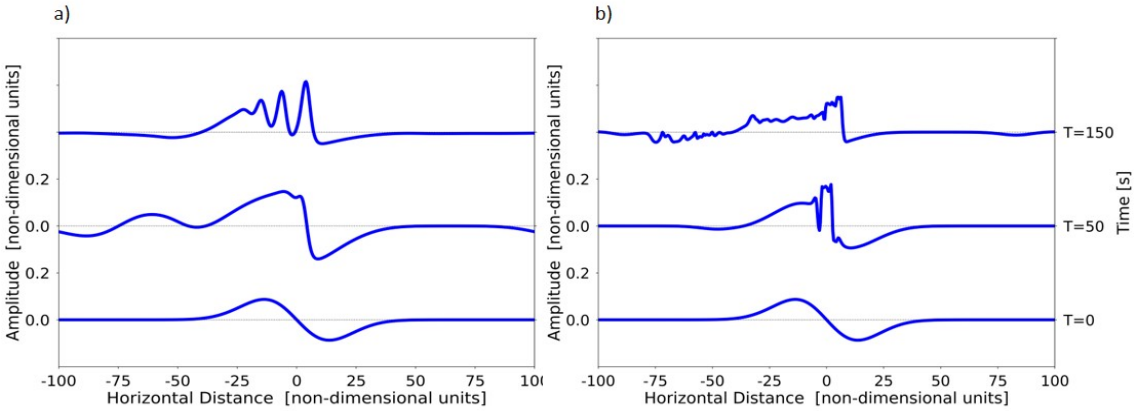


Figure 7.22: Sequence of line traces of potential temperature for simulation cases with Doppler duct and a) Thermal duct of strength 1.0 and b) Thermal duct of strength 0.25 as shown in Figure 7.19.

bore cases ends here. No clear trailing undulations or consistent solitary behavior in the presence of Doppler ducts that were reported earlier were observed. In contrast, there is a clear presence of small-scale fluctuations that are reminiscent of turbulent structures which seem to dominate the entire flow field at time $T = 150\ s$.

To investigate these fluctuating structures, we looked into how the entire flow field evolves. Figure 7.23 shows the evolution of the two-dimensional flow field from the initial ducted condition under (a) high and (b) low stability conditions. The simulation settings are such that the propagation direction is from left to right and the horizontal boundary conditions are periodic so that the wave that goes out of the right boundary emerges from the left boundary. In order to show the propagation in the moving frame of reference, (i.e.) the frame of reference of the moving bore, the bore speed has been removed from the flow field to portray the bore stationary. The high stability case (Figure 7.23(a)) indicates the formation of the peak wavefront at time $T = 50\ s$ followed by the trailing undulations and the process of peak formation is continuous with the trailing wave crests separating from the main wavefront. Displayed on the right side of the figure is the low-stability simulation case (Figure 7.23(b)). The initial stage of the evolution is similar where the initial wave distorts to form the peak wavefront. While the peak wavefront in the high stability cases looks definite, the one that is formed in the low stability case resembles an overturning structure, like KHI billow. And after his initial process, the low stability system evolves in a way that does not resemble the bore or solitary wave morphology. Instead, the system's response yields features of small-scale instabilities that are not very coherent and evolve into more turbulent structures later on. This shows that there is a fundamental qualitative and quantitative difference in the evolution of the flow field depending on the background stability condition. The reason for this could be twofold: In an environment that is controlled by a stronger inversion layer, the waves

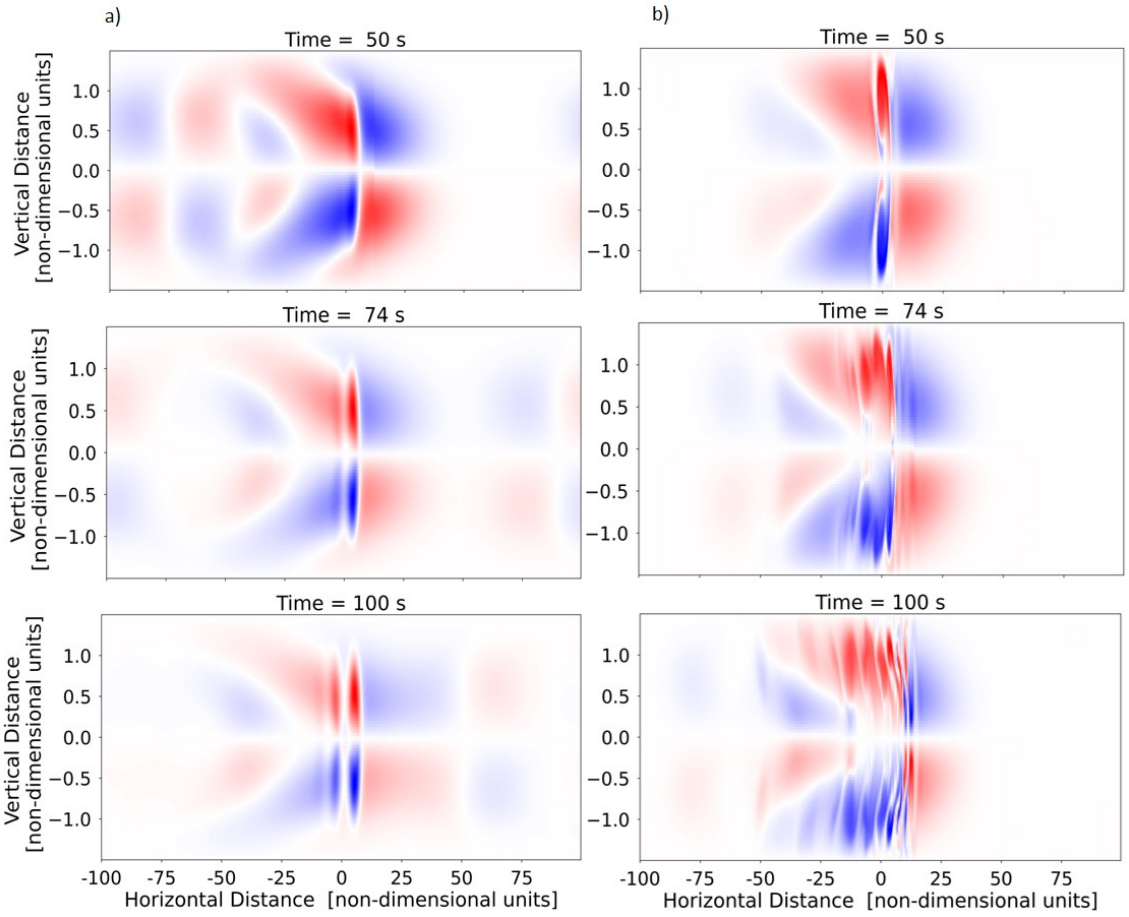


Figure 7.23: Contour plots of potential temperature evolution for simulation cases with Doppler duct and a) Thermal duct of magnitude 1.0 and b) Thermal duct of magnitude 0.25. Red indicates a positive value and blue indicates a negative value. Same as Figure 7.22

that have more energy are trapped and thereby can necessitate the bore formation. Meriwether and Gerrard (2004) and Fritts et al. (2018) reported that the weaker inversion layers lead to more transmission and not trapping of gravity waves implying that such inversion layers cannot trap large-amplitude gravity waves that may yield bores or other instabilities. Since inversion layers are regions of stability, any wave with a sufficient amplitude that is trapped could evolve into a bore or a solitary wave as we have demonstrated before. The other possibility is that the strength of the Doppler duct in relation to the thermal duct also determines how strong the duct is for the bore to form and propagate (Smith et al., 2017). In the two cases presented here, the bore was formed for the case where the stability was strong enough to induce a bore response. In the low stability case, the influence of the Doppler duct was more compared to the thermal duct which led to the ducted initial wave showing an unstable response resulting in instabilities and eventually, developing turbulence. Since variable wind shear is a more dynamic background condition, in the

absence of strong static stability, it can act as an additional forcing to the flow thereby yielding a stronger response that is composed of many small-scale structures that are more unstable (Fritts et al., 2014; Fritts et al., 2018; Fritts et al., 2020).

7.6 Can bores form in only Doppler ducts?

In the above sections, the effects of a thermal duct and the combination of a thermal and Doppler duct, which is considered a dual duct system, on the bore formation have been well-established. Moreover, the relation of the thermal duct strength to the Doppler duct was also numerically investigated. To further extend this investigation to see whether only a Doppler duct can yield bore formation, simulations were performed in which the background is controlled only by wind shear with a constant stability profile. Laughman et al. (2009) already performed simulations with the Doppler duct with a background temperature gradient resembling a thermal duct to prevent the leakage of wave energy away from the duct. However, the results presented were not conclusive as one could not see the nonlinear steepening of the wavefront of the initial wave that later forms a bore. Nor was there clear evidence of the presence of trailing waves if one uses the terminology *undular* bore. Nevertheless, it was the first attempt to simulate mesospheric bores under velocity ducting conditions. Fechine et al. (2009) reported the first observation of a mesospheric undular bore in a Doppler duct. Although the Doppler duct was the more prominent background condition in their observation, the thermal duct was non-zero implying that their observation of the undular bore could have been due to a dual-ducting structure rather than an isolated Doppler duct. It has not been established numerically in the literature whether the formation of the bore is possible with only a Doppler duct with no thermal duct being present. We wanted to investigate this by considering background conditions involving only a Doppler duct with no thermal duct (i.e.) a stability profile being zero, and constant stability throughout the domain.

Figure 7.24(a) shows the behavior of the system when the background conditions are controlled by the duality of a Doppler duct and a constant stability profile, (i.e.) Brunt-Vaisala frequency does not change with altitude. Quite a few things happen during this process. Foremost is the evident process of the nonlinear steepening of the initial wave similar to what we have reported earlier in other cases with either a thermal or a dual system of thermal and Doppler ducts. At the time, $T = 150\ s$, we can also see the formation of the wavefront and the subsequent generation of the trailing waves as the bore front evolves. These trailing waves are phase-locked with the leading bore front and span the entire vertical domain. Even though there is no thermal duct to constrain

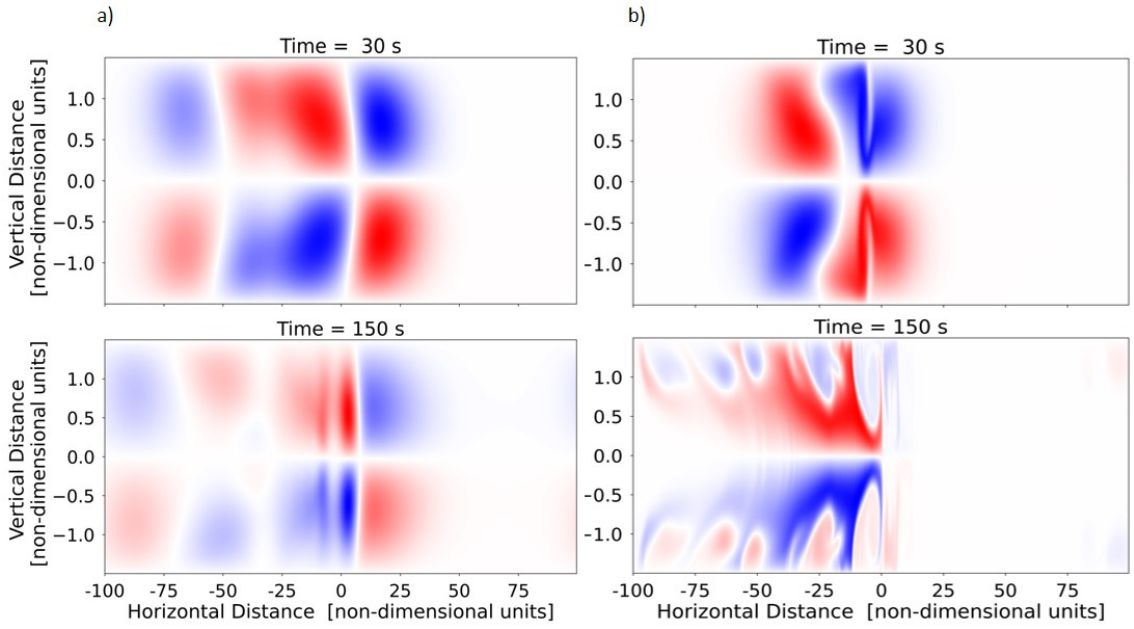


Figure 7.24: Contour plots of potential temperature evolution for simulation cases with background Doppler duct and a) Stability profile of constant magnitude 1.0 and b) Stability profile of constant magnitude 0. Red indicates a positive value and blue indicates a negative value.

the wave, the non-zero stability condition allows for the entrapment of the wave energy which along with the Doppler duct could have resulted in the bore being formed.

Figure 7.24(b) shows the simulation where the background stability profile was taken to be zero. This means that the background is controlled only by the Doppler duct. There is a lack of any semblance of wavefront formation or any trailing waves. The nonlinear steeping process that is important in the formation of bores or solitary waves does not happen. Instead of the generation of bores, at time $T = 150\,s$, we see a pattern of waves that resemble 'fishbone structures' that were reported by Vadas et al. (2018). Generally, the "fishbone" structure results from the interaction of secondary GWs that are generated due to the breaking of primary waves, in the limit of high background wind shear (Vadas et al., 2018; Vadas and Becker, 2018). In this case, the stability is zero and the background is controlled only by wind shear, the wave energy cannot be trapped effectively as in the other case (Isler et al., 1997). As a result, the ducted GW can interact freely with the background wind resulting in patterns that have not been observed before. Hence we can confidently say that for bores or solitary waves to form, the stability condition is an important controlling parameter than the wind shear that determines how the system will behave under a given initial condition.

7.7 Three-dimensional simulation of instabilities

With the available literature on the mesospheric bores, one can think of the morphology of the undular mesospheric bores as two-dimensional since all of them have a very straight wavefront with little to very little variation along the meridional direction (Smith et al., 2017). However, it should be kept in mind that the atmosphere is three-dimensional, and reducing one of the degrees of freedom will result in a loss of understanding of the full dynamics. The reported PMSE observation of extreme vertical velocities by Chau et al. (2020) indicated expected regions of large local horizontal wind convergence (divergence) accompanying the vertical divergence (convergence) near the central altitude of their observation (i.e.) at the midpoint where two layers are pushed up and down. Furthermore, the mesospheric double bore observation of Fritts et al. (2020) hypothesized motions resembling horizontal (vertical) convergence (divergence) ahead of their undular bore and horizontal (vertical) divergence (convergence) behind the bore. These regions of convergence and divergence infer the variable motion of the flow inferring the multiple crests of the undular bores in the initial theoretical studies of Dewan and Picard (1998) and Dewan and Picard (2001) and modeling studies of Seyler (2005), Laughman et al. (2009), and Ramachandran et al. (2023). Furthermore, the Kelvin-Helmholtz instabilities reported by Chau et al. (2020) and Hysell and Larsen (2021) indicated the formation of striations in the direction transverse to the billow orientation. These observations were the first to report the three-dimensionality of Kelvin-Helmholtz instabilities. Hence to understand the different responses of bore and associated instabilities in the MLT altitudes, three-dimensional modeling should be undertaken. Here, we present some results of the 3D simulations of bores and instabilities.

Figure 7.25 shows the 3D evolution of a system initialized with both a thermal duct (narrow) and a Doppler duct. The vertical domain has been considered in such a way that the flow evolution occurs far from it and is not affected by the vertical boundaries. The initial perturbation is centered near both the ducts. We see the distortion of the ducted gravity wave accommodating itself within the bounds of the ducts resulting in the formation of wavefront. After the initial distortion of the wave, we can see tendrils evolving off of the wavefront's trailing end. This morphology of the flow evolution where the main wavefront gives rise to secondary structures is reminiscent of what we already reported in the 2D simulations under the thermal-Doppler duct(see Figure 7.10. This secondary structure later evolves into an overturning vortex as the main wavefront propagates further away from it. This overturning of the secondary overturning occurs outside of the thermal duct and within the bounds of the Doppler duct. At a later time, the main wavefront continues to evolve, and positions itself fully within the thermal duct. At the same time, the overturning structures resembling KHI billows continue to evolve, advecting rearward, resulting in a complete mixing and turbulence of the resulting structure. The instability and the associated turbulence occur

in the flow domain which has reduced stability away from the center of the duct and is influenced more by the strong wind shear. The horizontal scale of the resulting KHI structure is ≈ 8 km which is close to the scales of the observed structures in the MLT altitudes (Baumgarten and Fritts, 2014; Fritts et al., 2020; Hysell and Larsen, 2021). As the simulation progresses, the overturning KHI continues to evolve in such a way that exhibits a mixing of the structure. Subsequently, during the final stages of mixing the primary KHI structure, additional small-scale structures with reduced horizontal scales start to develop that separate from the primary KHI. Such formation of small-scale instability structures resulting from the breaking of the primary instability has been routinely observed (Baumgarten and Fritts, 2014; Hysell and Larsen, 2021). Furthermore, along the spanwise direction, we can also see striations developing around the billow core after the onset of the primary instability. These striations are much smaller in size (≈ 3 km) compared to the main billow in the streamwise direction and orient themselves locally without a coherent pattern. The spanwise structures give rise to multi-scale dynamics where we see structures of different scales interacting leading to the billow formation in the direction transverse to the direction of the propagation. The apparent continuous occurrence of KHI accompanying the bores is not typical of the observed mesospheric undular bores (Fritts et al., 2020). In the 2D and 3D cases described above, they are a result of a coupled system where the background stability and wind shear play a role in initiating such dynamic responses. Our results indicating the occurrence of instabilities, not just in the propagation direction, but also in the transverse direction especially show the potential impact they may have on the bore formation as the dynamics involving their generation are likely to be widespread in the MLT. As illustrated here, bores involve strong local instabilities and mixing potentially exerting a more substantial influence on energy and momentum distribution across the atmosphere than previously recognized (Smith et al., 2005; Fritts et al., 2020).

While in the above segments, we have presented the formation of bores and the associated instabilities in 3D, the topic of a pure bore generation still remains an open question. To answer this question, the simulation settings that have resulted in the definite generation of bores in 2D were considered and extended to 3D. The background conditions for this simulation setting are shown in Figure 7.7. The 3D simulation domain along with the initial ducted wave is illustrated in Figure 7.26

The initial wave has been extended in the streamwise direction to replicate the ducted GW in 3D. We can see the distortion of the initial wave in the spanwise direction which is the result of the nonlinear process leading to the wave steepening which was also observed in the 2D cases. Additionally, the trailing waves are also evident at a later time. The streamwise plot shows the XY

orientation of the leading wavefront of the formed bore. There is little to no characteristic variation of the flow in the streamwise direction. The leading wavefront has an initial horizontal wavelength of $\approx$ 15 km during its formation which increases as the bore propagates. This is consistent with the other observations that have been reported in the MLT and a total of 3 trailing waves have been generated (Smith et al., 2017; Fritts et al., 2020). While the extension of the bore in the direction transverse to the propagation direction can be several hundred kilometers, the available literature on the bore observation indicates that in the majority of the reported cases, there is little to no change in its spatial structure in the transverse direction (Dewan and Picard, 1998). Several other observations of undular mesospheric bores made in recent years have affirmed this morphology where the leading wavefront of the bore has no undulations or shows dissimilarity in their structure along the transverse direction (Smith et al., 2003; Smith et al., 2005; Medeiros et al., 2005; Bageston et al., 2011; Smith et al., 2017; Fritts et al., 2020). The structure of the 3D simulated bore reported above is similar to those of the observations with many similarities in terms of spatial scales and associated secondary structures.

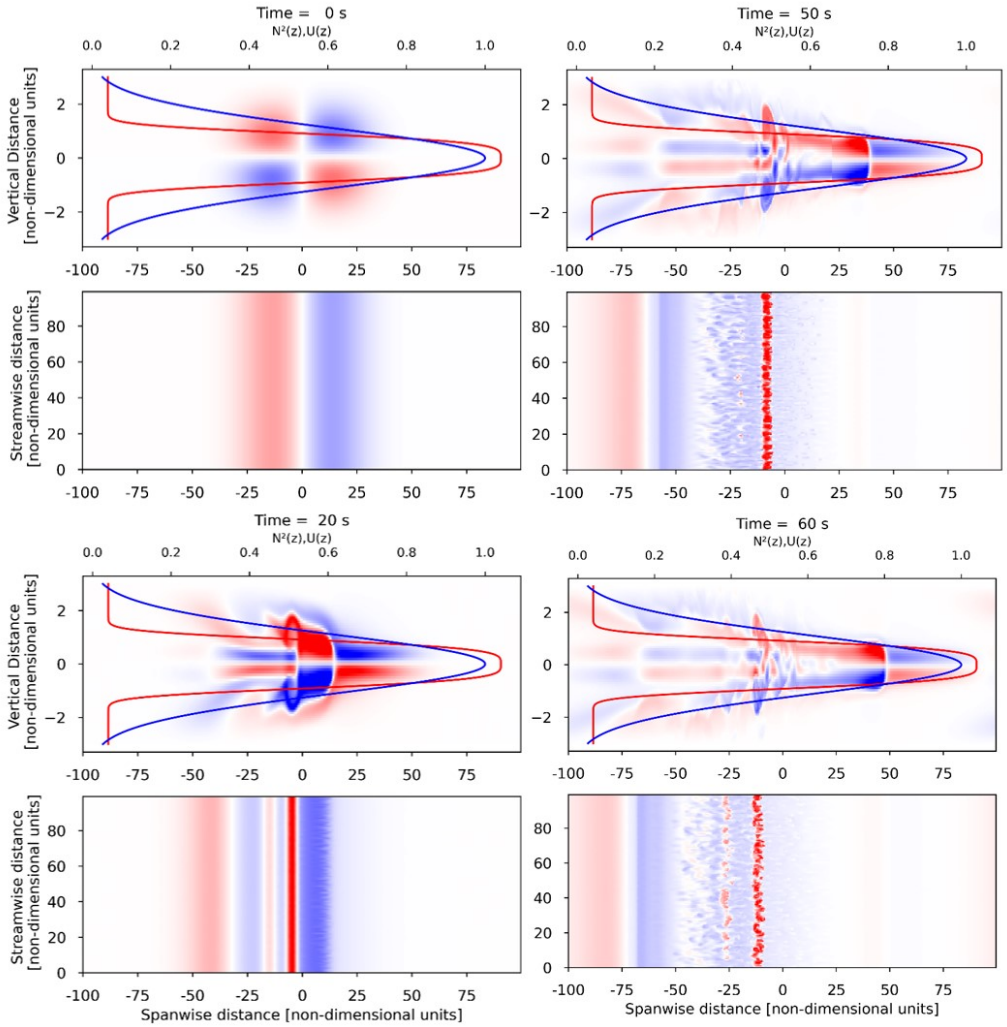


Figure 7.25: Contour plots showing the formation of wavefront and associated KH instability. The spanwise direction is the direction of propagation (X-direction) and the streamwise direction is the meridional direction (Y-direction). The blue and the red curves indicate the Doppler and thermal ducts, respectively.

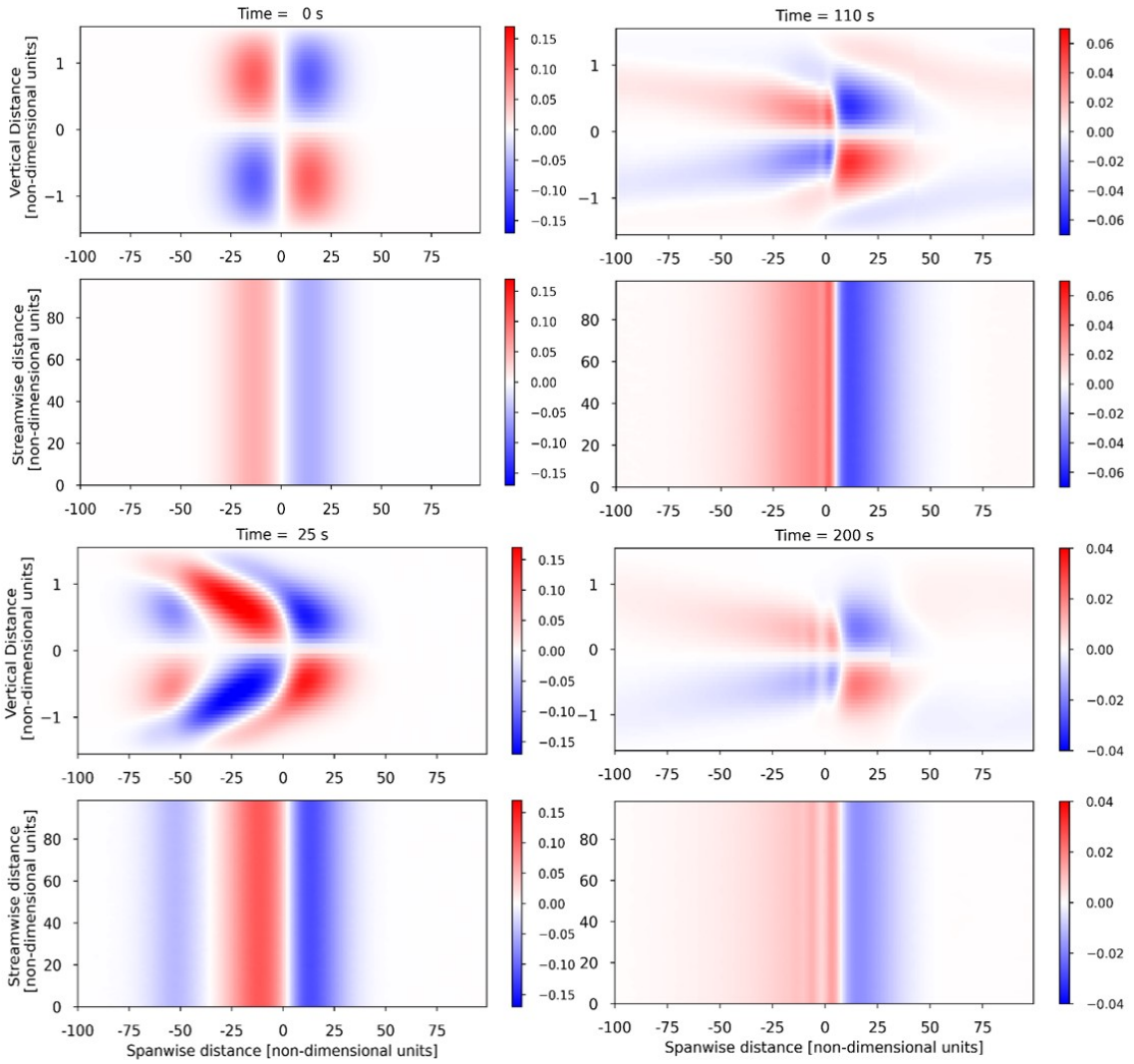


Figure 7.26: Contour plots showing 3D DNS of undular bores in the dual-duct system. The spanwise direction is the direction of propagation. Observed are the nonlinear steepening process a $T = 25\ s$, formation of trailing waves, and eventual dissipation. Notice that there is no variation of the structure in the streamwise direction

Chapter 8

Summary and Outlook

In this work, the dynamics of kilometer-scale instabilities in the mesosphere using airglow observations and DNS has been investigated. In particular, the observation of a bright mesospheric bore that occurred over northern Germany on the night of 16 March 2021 near 97 km has been presented. This bore was characterized by trailing undulations and a rapid dissipation under 20 mins within the FOV of the airglow imager. A multi-instrument investigation of this observation, combining satellite and radar, led to the determination of the presence of a strong thermal and Doppler duct between 94 and 97 km that may have aided the bore generation and propagation. The analysis of the brightness intensity of the different layers suggests that this bore event could have been caused by the nonlinear interaction of upward propagating GWs with the ducting layers. Initial 2D DNS was able to capture many of the characteristics of the observed bore by using a small-scale initial perturbation (relative to the horizontal domain) under the condition of a thermal Doppler duct. The phase-locked behavior of the trailing undulation with the wavefront, the increase of separation between the wave crests as the bore propagates, the number of trailing undulations, and the dissipation of the bore are all well captured in the simulations. Furthermore, the DNS results also showed that the bore morphology depends on the initial perturbation and duct width since for a narrow duct width and high amplitude initial perturbation, the system resulted in a solitary wave formation. This morphologically resembles the extreme event reported by Chau et al. (2021), thereby implying that the dynamics of bores, kilometer-scale instabilities, and extreme events may be closely related and more work is needed to understand their dynamics.

Upon investigating the influence of the dual ducting background, thermal and Doppler duct, on forming bores, solitary waves, and other kilometer-scale instabilities it was found that the

Doppler duct accentuated the nonlinearity of the bore. It also affected the dissipation of the bore, the number of trailing undulations, and formation time. Under the condition of a narrow thermal duct and a strong wind shear, for high amplitude initial perturbation, the system's response yielded solitary waves resembling the ones that were simulated in the thermal-only case. Since the Doppler duct is more of a dynamic background condition compared to the thermal duct which characterizes regions of static stability, it is to be expected that the system will not only yield bores and solitary waves but also other small-scale instabilities (Chau et al., 2020; Fritts et al., 2020). The system yielded either bores or solitary waves for overlapping thermal and Doppler ducts depending on the initial perturbation and duct width. However, for cases where the Doppler duct predominantly lay outside of the thermal duct, the system evolution led to secondary instabilities accompanying the bore or solitary waves. The dynamics of secondary instabilities evolving from and accompanying the bores have been previously reported in the observations (Fritts et al., 2020). Upon vertically shifting the Doppler duct concerning the thermal duct the resulting bore generation exhibited greater asymmetry in its morphology with the area where the Doppler duct held prominence producing a significantly stronger and more nonlinear response with additional small-scale structures following the main wavefront (Laughman et al., 2009).

Fritts et al. (2018) already demonstrated how the magnitude of the inversion layer affects the energy of the GWs trapped inside a duct. Accordingly, the DNS results show that the thermal duct which is formed as a consequence of the inversion layer has to be of a certain magnitude for it to affect the bore formation. If the thermal duct is significantly weaker than the Doppler duct, then the resulting dynamics involve the generation of secondary instabilities due to the predominance of the Doppler duct over the thermal duct (Fritts et al., 2018). While the generation of bores is guaranteed under purely thermal duct and constant background wind conditions the simulations involving a background Doppler duct and no thermal duct did not yield bore formation but rather the system evolved into a turbulence state instantly. Hence, it can be concluded that the background stability of sufficient magnitude and thereby a thermal duct is necessary for the trapping of the GW energy inside the duct for the generation of bores and solitary waves (Fritts et al., 2014; Fritts et al., 2020).

Initial results from 3D DNS show that the instabilities develop not just in the direction of propagation of the bore but also in the transverse direction. The trailing edge of the wavefront gives rise to overturning structures resembling KH instability that propagate downstream. In the streamwise orientation, overturning billows with horizontal scales less than the primary billows were seen confirming the evolution of structures similar to what has been reported in the observations (Chau et al., 2020; Hysell and Larsen, 2021). These overturning secondary billows also play a role in

the dissipation of the energy of the primary bore by transferring the energy to much smaller scales (Fritts et al., 2020; Fritts et al., 2023). The 3D simulations also yielded pure-bore-like structures without any accompanying instabilities but with a straight wavefront without any horizontal variation of the primary wavefront. The nonlinear process of wave steepening and the subsequent formation of the initial wavefront were also captured. The spatial separation of the crests increases with time which corroborates the already established dynamics in 2D (Seyler, 2005; Laughman et al., 2009).

In this thesis, the generation of kilometer-scale instabilities arose from deterministic conditions where the background and the initial conditions are defined a priori (Seyler, 2005). One cannot always expect such conditions to be present in the atmosphere. Due to the interplay of waves and the background, the background conditions may evolve in a way that is reminiscent of the ducting condition that is important for the bore generation and propagation (Dewan and Picard, 2001; Seyler, 2005; Smith et al., 2017). We have attempted to answer some of the long-standing questions such as the uncertainties related to bore behavior on the environmental and initial conditions, the complexity of the responses that arise from dual-ducting structures, and a need for the trapping of wave energy inside ducts. Other open questions like the potential sourcing mechanisms, nonlinear interaction of vertically-propagating GWs encountering an inversion layer (Chimonas and Hines, 1986; Snively and Pasko, 2008), breaking of GWs resulting in the generation of additional waves and turbulence leading to bore generation (Fritts and Alexander, 2003; Snively and Pasko, 2003), and local body forcing accompanying the bore and solitary wave generation(Dewan and Picard, 2001; Smith et al., 2005; Feraco et al., 2018) still need to be resolved to gain a complete understanding of the dynamics of kilometer-scale instabilities. As a part of future work, the above-mentioned processes can be investigated in a stochastic manner wherein the background is allowed to evolve to a state that comprises waves and turbulence replicating the realistic parameters of the MLT and then injecting perturbations into the flow. The perturbation can be in the form of upward propagating GW encountering a background controlled by dual-duct or multiple ducts (Walterscheid and Hickey, 2011).Hartisch et al. (2023) recently reported on the observation of kilometer-scale instabilities in the PMSE resembling varicose-mode waves that exhibit interesting characteristics similar to extreme vertical drafts and mesospheric bores. A coupled investigation into these events by complementing them with DNS can prove to be beneficial for furthering the understanding of the dynamics of kilometer-scale instabilities.

Other kilometer-scale neutral instabilities have been recently observed in the MLT but are yet to be fully investigated (Hysell and Larsen, 2021; Bui et al., 2023; Fritts et al., 2023). Recently, by using radar imaging Hysell and Larsen (2021) and Bui et al. (2023) reported that the speed and

the presence of turning shears that accompany KH instabilities are conducive to the occurrence of other neutral instabilities. A particular type of this turning shear instability is the Ekman-type instability. They are, like the more common KH instabilities, inflection-point instabilities associated with turning shears resulting in convective rolls aligned to the mean wind direction with accompanying secondary structures that are perpendicular to the primary structures (Bui et al., 2023). The attempt to simulate Ekman-type instability will involve the background being controlled not just by shear in direction and amplitude but also by rotation. Observations of such instabilities in the MLT region are extremely limited in general despite the critical importance of the region. The atmospheric boundary layer is known to exhibit a variety of similar instabilities. Although the causes of the flows are very different in the MLT and atmospheric boundary layers, the similarity of the dynamics of such instabilities invites an investigation. The upwelling and the overturning of the Ekman instabilities can lead to the vertical transport of momentum and energy between the different layers which is important in the context of the vertical coupling of the atmosphere. Aided by the improvements in observational techniques and the availability of state-of-the-art computational resources, we are gaining more and more insights into the dynamics of kilometer-scale instabilities that are important for understanding the dynamics of the whole MLT region.

Appendix A

List of peer-reviewed publications

The work carried out in this thesis led to the peer-reviewed publication

- **K. Ramachandran**, M. Sivakandan J. L. Chau, J.M. Urco, M. Gerding, S. Grundmann, S.M. Smith. Investigation of a Dissipating Mesospheric Bore Using Airglow Imager and Direct Numerical Simulation. *JGR Space Physics*, 2023.

Appendix B

Boussinesq Approximation

The Boussinesq approximation is a way to solve nonisothermal flow, such as natural convection problems, without having to solve for the full compressible formulation of the Navier-Stokes equations. The approximation is accurate when density variations are small as this reduces the nonlinearity of the problem. It assumes that variations in density have no effect on the flow field, except that they give rise to buoyancy forces. To derive the Boussinesq equations, we begin by writing the balance laws for mass, momentum, and thermal energy

Conservation of Mass

$$\frac{1}{\rho}\frac{\partial \rho}{\partial t} + \nabla \cdot \mathbf{u} = 0 \tag{B.1}$$

Since the Boussinesq assumption states that the density variations are small, the magnitude of $1/\rho(\partial\rho/\partial t)$ is small with respect to the velocity gradient $\nabla \cdot \mathbf{u}$. Hence it follows that $\boxed{\nabla \cdot \mathbf{u} = 0}$

Conservation of Momentum

The incompressible form of the equation is given by,

$$\rho\frac{\partial \mathbf{u}}{\partial t} + \mathbf{u}\cdot\nabla\mathbf{u} = -\nabla p + \rho\mathbf{g} + \mu\nabla^2\mathbf{u} \tag{B.2}$$

For each state variable q let q_0 represent the background stratified state in hydrostatic balance and q' is any deviation (fluctuation) from the background state, such that,

$$q = q_0 + q'\rho = \rho_0 + \rho', p = p_0(z) + p' \tag{B.3}$$

The hydrostatic balance is given by $dp_0/dz = -\rho_0 g$. Now equation mom1 can be rewritten using pert as follows

$$(\rho_0 + \rho')\frac{\partial \mathbf{u}}{\partial_t} + \mathbf{u}\cdot\nabla\mathbf{u} = -\nabla(p_0 + p') + (\rho_0 + \rho')\mathbf{g} + \mu\nabla^2\mathbf{u} \tag{B.4}$$

Using the hydrostatic balance, we can subtract the terms ∇p_0 and $\rho_0\mathbf{g}$ which leads to the following relation

$$(1 + \frac{\rho'}{\rho_0})\frac{\partial \mathbf{u}}{\partial t} + \mathbf{u}\cdot\nabla\mathbf{u} = -\frac{\nabla p'}{\rho_0} + \frac{\rho'}{\rho_0}\mathbf{g} + \nu\nabla^2\mathbf{u} \tag{B.5}$$

where $\nu := \frac{\mu}{\rho_0}$ is the kinematic viscosity. Then, according to the Boussinesq assumption of $\rho' << \rho_0$, we get

$$\frac{\partial \mathbf{u}}{\partial t} + \mathbf{u}\cdot\nabla\mathbf{u} = -\frac{\nabla p'}{\rho_0} + \frac{\rho'}{\rho_0}\mathbf{g} + \nu\nabla^2\mathbf{u} \tag{B.6}$$

Thermal Energy

The energy balance equation is given by

$$\rho\frac{de}{dt} + p\nabla\cdot\mathbf{u} = -\nabla\cdot\mathbf{q} \tag{B.7}$$

where e is the internal energy and $\mathbf{q} = -\kappa\nabla T$. One can simplify each term in the above equation using ideal gas relations $e = c_v T$, $p = \rho R T$, and $c_p - c_v = R$.

$$\rho\frac{de}{dt} = \rho c_v\frac{dT}{dt} \tag{B.8}$$

and using $lnP = ln\rho + lnT$, we get

$$p\nabla \cdot \mathbf{u} = -p\frac{d\left(ln\rho\right)}{dt} = p\frac{d\left(lnT - lnp\right)}{dt} = \rho R\frac{dT}{dt} - \frac{dp}{dt} \tag{B.9}$$

In equation thermal, we have made use of the mass conservation relation from equation mass. Using thermal and b8, energybalance can be written as,

$$\rho c_p \frac{dT}{dt} = \kappa\nabla^2 T \tag{B.10}$$

Furthermore, $d\ln p = d\ln\rho + d\ln T\frac{p}{p0} = \frac{\rho}{\rho_0} + \frac{T}{T_0}$. From this relation $T = \left(-\frac{T_0}{\rho_0}\right)\left(\rho - \frac{\rho_0}{p_0}p\right)$ One can use this relation to rewrite the thermal balance equation (thermal) in terms of density perturbations as follows

$$d_t\left(\rho - \frac{\rho_0}{p_0}\right) = \kappa\nabla^2\left(\rho - \frac{\rho_0}{p_0}\right) \tag{B.11}$$

Following $q = q_0 + q'$, we get

$$\partial_t\left(\rho' - \frac{\rho_0}{p_0}p'\right) + \mathbf{u}\cdot\mathbf{z}\underbrace{\partial_z\left(\rho - \frac{\rho_0}{p_0}p\right)}_{-b} = \kappa\nabla^2\left(\rho' - \frac{\rho_0}{p_0}p'\right) \tag{B.12}$$

Ignoring the effect of pressure derivatives, and Laplacian terms, we finally get

$$\partial_t\rho' - b\mathbf{u}\cdot\mathbf{z} = \kappa\nabla^2\rho' \tag{B.13}$$

In the above equation, we have made use of the partial derivative instead of full derivative since $\frac{d}{dt} = \frac{\partial}{\partial_t} + \mathbf{u}\cdot\nabla$.

The full set of Boussinesq equations is then mass, mom, and energy,

$$\nabla\cdot\mathbf{u} = 0 \tag{B.14}$$

$$\partial_t\mathbf{u} + \mathbf{u}\cdot\nabla\mathbf{u} = -N^2\theta\mathbf{z} - \nabla p + \nu\nabla^2\mathbf{u} \tag{B.15}$$

$$\partial_t\theta + \mathbf{u}\cdot\nabla\theta = \mathbf{u}\cdot\mathbf{z} + \kappa\nabla^2\theta \tag{B.16}$$

The density have been replaced by potential temperature following, $\frac{\theta'}{\theta} = \frac{\rho'}{\rho}$.

Symbols and Acronyms

x	scalar
x	vector
θ	potential temperature
ρ	density
ψ	streamfunction
μ	dynamic viscosity
ν	kinematic viscosity
$[\kappa]$	thermal diffusivity
$[A, B]$	Jacobian Matrix
ζ	Vorticity
N	Brunt–Väisälä frequency
∇	Laplacian operator
Γ	Background adiabatic lapse rate
Γ_d	dry adiabatic lapse rate
g	acceleration due to gravity
c_p	specific heat at constant pressure
c_v	specific heat at constant volume
Φ	Geopotential
MLT	Mesosphere and Lower Thermosphere
GW	Gravity Waves
DNS	Direct Numerical Simulations
KHI	Kelvin-Helmholtz Instability

List of Figures

1.1 Schematic representing the vertical structure of the atmosphere. The four main layers are illustrated. Figure taken from (Sutherland, 2010) 3

1.2 Theoretical horizontal and vertical kinetic energy spectrum diagram describing the scales of motion in which regimes are dominated by Rossby Waves, gravity waves, and isotropic turbulence. The X-axis (log scale) represents the wavenumber while the Y-axis represents the energy content. Figure adapted from (Urco Cordero, 2020) 4

1.3 (Left) 2D cuts of PMSE images of KHI with spanwise and streamwise orientation. Figure taken from (Chau et al., 2020) (Right) PMSE observation of extreme vertical velocities in the order of 50 m/s in up and downdrafts. Figure taken from (Chau et al., 2021). In both the figures, red indicates positive (upwards) velocity, and blue indicates negative (downwards) velocity. 6

2.1 A schematic of atmospheric gravity waves. Figure from (Hines, 1974) 10

2.2 An illustration of a two-dimensional wave with its corresponding horizontal and vertical components. The wavefronts are perpendicular to the wave vector. Figure from (Nappo, 2013) 12

2.3 A cross-section of a wave showing the effects of wave dispersion at early and later times. 16

2.4 An illustration to describe the conditions of stability of a displaced dry air parcel in the atmosphere. a) Positive static stability $\Gamma > \Gamma_d$, b) Negative static stability $\Gamma < \Gamma_d$ 20

3.1 Schematic of the background velocity profile for Kelvin-Helmholtz instability . . 28

3.2 Time evolution of Kelvin-Helmholtz instability from high resolution (512×512) direct numerical simulations for a (Left) Reynolds number of 1000, (Right) Reynolds number of 5000 29

3.3 Schematic diagram to illustrate the Ekman Spiral in a column of fluid. The black solid arrows indicate the direction of the flow at each layer of the column. The red dotted arrows at the bottom of the column indicate the projection of the formed spiral 32
3.4 Time evolution of Rayleigh-Benard instability in a highly stratified fluid from high resolution (512 × 512) DNS. 33
3.5 Left: Tidal bore in the Severn river in the UK. Right: Turbulent tidal bore in Qiantang River in China. Images taken from *https://noc.ac.uk* 35
3.6 Sequence of all-sky CCD images showing the first reported observation of mesospheric undular bore. Shown on the left are images from the OI(557.7nm) emission and on the right are the airglow images from OH emission. Adapted from Taylor et al. (1995) 36
3.7 a) Schematic diagram of the oscillating duct. The dashed line indicates the center of the duct. The solid black and red colors indicate the airglow layer being pushed up and down leading to dark and bright bore, respectively. b) Sketch of the inversion layer and the associated thermal duct. c) Complementary effects observed in airglow images based on the Dewan and Picard (1998) model, O_2 layer shows a propagating dark bore and OH layer a propagating bright bore. 37
3.8 Complementary effects predicted by the linear model of Dewan and Picard (1998). Red represents the bright bore and black represents the dark bore. The solid black arrow indicates the direction of the bore propagation. 38
3.9 Complementary effects not predicted by the linear model of Dewan and Picard (1998). Red represents the bright bore and black represents the dark bore. The solid black arrow indicates the direction of the bore propagation. 39
3.10 b) Distribution and occurrence of propagating mesospheric bores captured by Visible and near Infrared Spectral Imager (VISI). c)-f) Rate of occurrence of the bores as a function of latitude and seasons. Figure taken from Hozumi et al. (2019) 40
3.11 Sketch of the highly idealized density profile used by Dewan and Picard (1998). . 41

4.1 (a) Airglow as viewed from the International Space Station. The altitude of this emission is between the mesosphere and thermosphere. Image taken from *https://eol.jsc.nasa.gov* (b) A sketch of different mesospheric airglow layers and their peak emission altitudes. 44
4.2 a) Snapshots of NLC exhibiting small-scale structures with an intermix of waves and turbulence. b) Mesospheric front exhibiting soliton-like behavior. The white arrows indicate the position of the soliton. Taken from Dalin et al. (2013). 46

4.3 65 × 65 km horizontal coverage of the composite FOV imaging showing the bore evolution at ∼ 82 km and propagation at a higher spatial and temporal resolution of ∼ 50 m, and 2.5 min, respectively. Figure taken from Fritts et al. (2020) 46
4.4 MAARSY radar system located at Andoya, Norway 48
4.5 Example of the application of MIMO technique to study the KH instability. . . . 49

5.1 Different basis grids in Dedalus. The Fourier grid is evenly spaced. The Chebyshev and Legendre basis grids cluster near the ends of a finite interval. The Compound basis concatenates other bases on adjacent segments. 52
5.2 Block diagram showing the steps to set up a simulation in Dedalus. 52
5.3 Panel plot showing the tracer evolution of KH instability for different resolutions with Re = 10^5. All the simulations are well resolved with small differences in the lower resolution. 54
5.4 Plot showing the evolution of the flow field under (a) double Fourier domain and (b) Fourier-Chebyshev domain. 54
5.5 Contour plots showing the effect of vertical boundaries on flow field evolution. . 55

6.1 A sequence of O(^{1}S) 557.7 nm airglow images over northern Germany on March 16, 2021. A front-like structure appeared on the southwestern edge of the image at around 21:30 UT and propagated northeast in the consecutive images followed by trailing waves. The yellow arrow points in the direction of propagation. Figure taken from Ramachandran et al. (2023) 59
6.2 A sequence of O($_2$) airglow images over northern Germany on March 16, 2021. A front-like structure appeared in the southwestern edge of the image at around 21:30 UT and propagated northeast in the consecutive images followed by trailing waves. The yellow arrow points in the direction of propagation. Figure taken from Ramachandran et al. (2023) 60
6.3 A sequence of OH airglow images over northern Germany on March 16, 2021. A front-like structure appeared in the southwestern edge of the image at around 21:30 UT and propagated northeast in the consecutive images followed by trailing waves. The yellow arrow points in the direction of propagation.Figure taken from Ramachandran et al. (2023) 61
6.4 Keogram brightness plot of different airglow layers. a) O(^{1}S) airglow emission, b) O_2 airglow emission, and c) OH airglow emission. The solid black oval indicates the structure of the undular bore in the airglow. 62

6.5 (a–d) The magenta, green, and blue solid lines in each panel depict the intensity variation of O(^{1}S), O_2, and OH airglow emissions at constant time, respectively along their line of propagation. The black arrow indicates the propagation direction. Figure taken from Ramachandran et al. (2023) 63
6.6 (a) SABER-1 (23:58 UT, 50.10°N, 9.57°E) and (b) SABER-2 (23:59 UT, 51.06°N, 15.47°E) represents the vertical profile of temperature from SABER (blue line) and the corresponding squared Brunt-Väisälä frequency (N 2) profile (red line) at two different locations on 16 March 2021. The horizontal solid lines indicate the peak emission altitudes of O(1S), O2, and OH airglow emissions on 16 March 2021. The vertical red dashed lines point to zero values in the stability profile. A persistent inversion layer is visible between 95 and 97 km. Figure taken from Ramachandran et al. (2023) 64
6.7 Volumetric emission rate of different airglow layer on 16 March 2021 65
6.8 (a) The zonal, (b) the meridional winds on 15 and 16 March 2021. The horizontal dotted lines indicate the peak emission altitudes of O(^{1}S), O_2, and OH airglow emissions on 16 March 2021. The two vertical dotted lines indicate the time limit of the bore event on 16 March 2021. 66
6.9 Schematic of the bore propagation direction and the resultant wind direction at different emission altitudes. The blue solid lines indicate the bore direction and orange arrows indicate the wind direction 67
6.10 a) Profiles of m^2 derived from SABER 1 (green line), SABER 2 (black line), and the winds. b) Zonal and Meridional wind amplitudes between 90 and 97 km for days 15, 16, and 17th March 2021. The vertical line denotes the day of the observed undular bore event (16 March 2021). There is a clear increase in the amplitude of the winds during this time compared to the day before and after. c) FFT of the winds where the 6h, 8h, and 12h tides are marked by vertical dotted lines. 68
6.11 (a) Initial perturbation in the form of ducted gravity wave. (b) Thermal duct for two different cases simulated. 70
6.12 (a) Brightness intensity plot showing the temporal and spatial evolution of undular bore in O(^{1}S) 557.7 nm airglow emission. The lines are shifted vertically by an offset factor of 2 to represent the time evolution. The time series was obtained by rotating the residual images by an azimuth angle of 14° in the anti-clockwise direction from North and then taking a zonal average (i.e.) in the direction perpendicular to the bore propagation. (b) Potential temperature traces from DNS representing the undular bore evolution with initial amplitude, A $\approx$ 0.08 for wide duct with constant background wind. Figure taken from Ramachandran et al. (2023) 71

7.1 (a) XZ-cut of the simulation domain. The color contours represent the non-dimensional initial perturbation indicating ducted wave. The initial perturbation does not span the entire horizontal domain. (b) Background ducting profiles (N^2) used in the DNS. The wide duct (red) has a non-dimensional FWHM of $\approx$ 2.0 and a narrow duct (blue) has a value of $\approx$ 1.0. See Table 7.1 for more details. 74
7.2 Time series of potential temperature line traces for (a) Case-1 and (b) Case-5. Both simulations were initialized with a non-dimensional amplitude of A $\approx$ 0.10. The inset text indicates peak bore amplitude. Each trace has been offset by a constant value for clarity. 76
7.3 Contour plots of potential temperature evolution for Case-1 and Case-5 with a non-dimensional amplitude of A $\approx$ 0.10. Red is positive and blue is negative. Non-dimensional times are 0 s, 50 s, 100 s. Same as Figure 7.2 77
7.4 Time series of potential temperature line traces for (a) Case-1 and (b) Case-5. Both simulations were initialized with a non-dimensional amplitude of A $\approx$ 0.18. Each trace has been offset by a constant value to refer to the time evolution. 78
7.5 Contour plots of potential temperature evolution when initialized with an amplitude of 0.18 for (a) Case-1, and (b) Case-5. Red indicates a positive value and blue indicates a negative value. Non-dimensional times are 0 s, 50 s, 90 s. Same as Figure 7.4. 79
7.6 Effects of varying ducting conditions and initial perturbations. Figure taken from Ramachandran et al. (2023) 80
7.7 Dual Duct system where both Thermal (Red) and Doppler (Blue) ducts are present. (a) Thermal duct with FWHM ≈ 2.0 (Case-5), (b) Thermal duct with FWHM ≈ 1.0 (Case-1). Doppler duct is the same in both cases. 82
7.8 Time series of potential temperature traces for simulation cases for, a) Thermal-only duct (Case-5), and b) Thermal (Case-5) and Doppler duct shown in Figure 7.7(a) 83
7.9 Contour plots of potential temperature evolution for a) Thermal-only duct, and b) Thermal and Doppler duct. Red indicates a positive value and blue indicates a negative value. Same as Figure 7.8. 85
7.10 Time series of potential temperature traces showing the effects of the magnitude of the Doppler duct on the bore formation. (a) Doppler duct of magnitude of 1.0. (b) Doppler duct of magnitude of 0.5. Both the simulations have the wide thermal duct (Case-5) 86
7.11 Contour plots showing the formation of secondary instabilities in a thermal Doppler system shown in Figure 7.7 (b). 88

7.12 Dual Duct system where both Thermal (red) and Doppler (blue) ducts are present. The Doppler ducts are fully enveloped inside the thermal duct. Two different Doppler ducts with different magnitudes were investigated. Thermal duct considered is a narrow duct (Case-1). 89
7.13 Time series of potential temperature traces for simulation cases with both thermal and Doppler ducts shown in Figure 7.12. Doppler ducts have magnitudes of 0.25 and 0.5 91
7.14 Contour plots of potential temperature on the solitary wave formation with thermal and Doppler ducts shown in Figure 7.12. Same as Figure 7.13 92
7.15 Contour plots of potential temperature evolution for the vertically displaced dual duct system. The red and the blue lines indicate the thermal and the Doppler ducts, respectively. The Doppler duct has been vertically displaced by a factor of 1 with respect to the thermal duct. The initial perturbation is centered around the thermal duct. 94
7.16 Time series of potential temperature traces for simulation cases for thermal-only duct (Case-5) with a) Viscosity of $5\ m/s^2$, b) Viscosity of $15\ m/s^2$ 95
7.17 Sequence of line traces of potential temperature for simulation cases in the dual-duct system shown in Figure 7.7(a) with a) Viscosity of $5\ m\ s^{-2}$, and b) Viscosity of $15\ m\ s^{-2}$ 97
7.18 Contour plots of the effects of viscosity on bore evolution with both thermal and doppler ducts a) Viscosity of $5\ m\ s^{-2}$, and b) Viscosity of $15\ m\ s^{-2}$. Same as Figure 7.17 98
7.19 Profiles of Doppler duct and a) Thermal duct of magnitude 1.0, b) Thermal duct of magnitude 0.25 99
7.20 Sequence of line traces of potential temperature for simulation cases initialized with constant background wind for (a) Thermal duct of magnitude 1.0 and (b) Thermal duct of magnitude 0.25. 100
7.21 Contour plots of potential temperature evolution for constant background wind and a) Thermal duct of magnitude 1.0 and b) Thermal duct of magnitude 0.25. Red indicates a positive value and blue indicates a negative value. Same as Figure 7.20 101
7.22 Sequence of line traces of potential temperature for simulation cases with Doppler duct and a) Thermal duct of strength 1.0 and b) Thermal duct of strength 0.25 as shown in Figure 7.19. 102
7.23 Contour plots of potential temperature evolution for simulation cases with Doppler duct and a) Thermal duct of magnitude 1.0 and b) Thermal duct of magnitude 0.25. Red indicates a positive value and blue indicates a negative value. Same as Figure 7.22 103

7.24 Contour plots of potential temperature evolution for simulation cases with background Doppler duct and a) Stability profile of constant magnitude 1.0 and b) Stability profile of constant magnitude 0. Red indicates a positive value and blue indicates a negative value. 105
7.25 Contour plots showing the formation of wavefront and associated KH instability. The spanwise direction is the direction of propagation (X-direction) and the streamwise direction is the meridional direction (Y-direction). The blue and the red curves indicate the Doppler and thermal ducts, respectively. 109
7.26 Contour plots showing 3D DNS of undular bores in the dual-duct system. The spanwise direction is the direction of propagation. Observed are the nonlinear steepening process a $T = 25\ s$, formation of trailing waves, and eventual dissipation. Notice that there is no variation of the structure in the streamwise direction 110

List of Tables

7.1 Different thermal duct widths that were used as a background condition in non-dimensional units. 75
7.2 Simulation results showing bore formation time and the bore peak amplitude for different initial amplitudes of perturbation. The ducting profiles used are shown in Figure 7.7(a) 86
7.3 Simulation results showing bore formation time and the bore peak amplitude for different initial amplitudes of perturbation. The ducting profiles used are shown in Figure 7.12(b) 93

Bibliography

Akmaev, R. A., T. J. Fuller-Rowell, F. Wu, J. M. Forbes, X. Zhang, A. F. Anghel, M. D. Iredell, S. Moorthi, and H.-M. Juang (Feb. 2008). "Tidal variability in the lower thermosphere: Comparison of Whole Atmosphere Model (WAM) simulations with observations from TIMED". In: *Geophysical Research Letters* 35.3. DOI: 10.1029/2007gl032584.

Allen, Leanne and Thomas J. Bridges (May 2003). "Hydrodynamic stability of the Ekman boundary layer including interaction with a compliant surface: a numerical framework". In: *European Journal of Mechanics - B/Fluids* 22.3, pp. 239–258. DOI: 10.1016/s0997-7546(03)00036-0.

Bageston, J. V., C. M. Wrasse, R. E. Hibbins, P. P. Batista, D. Gobbi, H. Takahashi, V. F. Andrioli, J. Fechine, and C. M. Denardini (Jan. 2011). "Case study of a mesospheric wall event over Ferraz station, Antarctica (62° S)". In: *Annales Geophysicae* 29.1, pp. 209–219. DOI: 10.5194/angeo-29-209-2011.

Batista, Paulo P, Barclay R Clemesha, Dale M Simonich, Michael J Taylor, Hisao Takahashi, Delano Gobbi, Inez S Batista, Ricardo A Buriti, and Amauri F de Medeiros (Aug. 2002). "Simultaneous lidar observation of a sporadic sodium layer, a "wall" event in the OH and OI5577 airglow images and the meteor winds". In: *Journal of Atmospheric and Solar-Terrestrial Physics* 64.12-14, pp. 1327–1335. DOI: 10.1016/s1364-6826(02)00116-5.

Baumgarten, Gerd and David C. Fritts (2014). "Quantifying Kelvin-Helmholtz instability dynamics observed in noctilucent clouds: 1. Methods and observations". In: *Journal of Geophysical Research: Atmospheres* 119.15, pp. 9324–9337. DOI: https://doi.org/10.1002/2014JD021832.

Brown, L. B., A. J. Gerrard, J. W. Meriwether, and J. J. Makela (2004). "All-sky imaging observations of mesospheric fronts in OI 557.7 nm and broadband OH airglow emissions: Analysis of frontal structure, atmospheric background conditions, and potential sourcing mechanisms". In: *Journal of Geophysical Research D: Atmospheres* 109 (19). DOI: 10.1029/2003JD004223.

Bui, Michelle X., David L. Hysell, and Miguel F. Larsen (2023). "Midlatitude Sporadic E-Layer Horizontal Structuring Modulated by Neutral Instability and Mixing in the Lower Thermosphere". In: *Journal of Geophysical Research: Space Physics* 128.2. e2022JA030929 2022JA030929, e2022JA030929. DOI: https://doi.org/10.1029/2022JA030929.

Burns, Keaton J., Geoffrey M. Vasil, Jeffrey S. Oishi, Daniel Lecoanet, and Benjamin P. Brown (2020). "Dedalus: A flexible framework for numerical simulations with spectral methods". In: *Phys. Rev. Research* 2 (2), p. 023068. DOI: 10.1103/PhysRevResearch.2.023068.

Chau, J L, R Marino, F Feraco, J M Urco, G Baumgarten, F.-J. Lübken, W K Hocking, C Schult, T Renkwitz, and R Latteck (2021). "Radar Observation of Extreme Vertical Drafts in the Polar Summer Mesosphere". In: *Geophysical Research Letters* 48 (16). DOI: 10.1029/2021GL094918.

Chau, J L, J M Urco, V Avsarkisov, J P Vierinen, R Latteck, C M Hall, and M Tsutsumi (2020). "Four-Dimensional Quantification of Kelvin-Helmholtz Instabilities in the Polar Summer Mesosphere Using Volumetric Radar Imaging". In: *Geophysical Research Letters* 47 (1). DOI: 10.1029/2019GL086081.

Chimonas, G and C O Hines (1986). "Doppler ducting of atmospheric gravity waves". In: *Journal of Geophysical Research* 91 (D1), p. 1219. DOI: 10.1029/JD091iD01p01219.

Conte, J. Federico, Jorge L. Chau, Juan M. Urco, Ralph Latteck, Juha Vierinen, and Jacobo O. Salvador (Feb. 2021). "First Studies of Mesosphere and Lower Thermosphere Dynamics Using a Multistatic Specular Meteor Radar Network Over Southern Patagonia". In: *Earth and Space Science* 8.2. DOI: 10.1029/2020ea001356.

Dalin, P., M. Connors, I. Schofield, A. Dubietis, N. Pertsev, V. Perminov, M. Zalcik, A. Zadorozhny, T. McEwan, I. McEachran, J. Grønne, O. Hansen, H. Andersen, S. Frandsen, D. Melnikov, V. Romejko, and I. Grigoryeva (2013). "First common volume ground-based and space measurements of the mesospheric front in noctilucent clouds". In: *Geophysical Research Letters* 40.24, pp. 6399–6404. DOI: 10.1002/2013gl058553.

Dewan, E M and R H Picard (Mar. 1998). "Mesospheric bores". In: *Journal of Geophysical Research: Atmospheres* 103 (D6), pp. 6295–6305. DOI: 10.1029/97JD02498.

— (Feb. 2001). "On the origin of mesospheric bores". In: *Journal of Geophysical Research: Atmospheres* 106 (D3), pp. 2921–2927. DOI: 10.1029/2000JD900697.

Dong, Wenjun, David C Fritts, Gary E Thomas, and Thomas S Lund (July 2021). "Modeling Responses of Polar Mesospheric Clouds to Gravity Wave and Instability Dynamics and Induced Large-Scale Motions". In: *Journal of Geophysical Research: Atmospheres* 126 (13). DOI: 10.1029/2021JD034643.

Drazin, P. G. and W. H. Reid (2004). *Hydrodynamic Stability*. 2nd ed. Cambridge Mathematical Library. Cambridge University Press.

Dubos, T., C. Barthlott, and P. Drobinski (July 2008). "Emergence and Secondary Instability of Ekman Layer Rolls". In: *Journal of the Atmospheric Sciences* 65.7, pp. 2326–2342. DOI: 10.1175/2007jas2550.1.

Fechine, J, A F Medeiros, R A Buriti, H Takahashi, and D Gobbi (2005). "Mesospheric bore events in the equatorial middle atmosphere". In: *Journal of Atmospheric and Solar-Terrestrial Physics* 67 (17-18), pp. 1774–1778. DOI: 10.1016/j.jastp.2005.04.006.

Fechine, J, C M Wrasse, H Takahashi, A F Medeiros, P P Batista, B R Clemesha, L M Lima, D Fritts, B Laughman, M J Taylor, P D Pautet, M G Mlynczak, and J M Russell (2009). "First observation of an undular mesospheric bore in a Doppler duct". In: *Annales Geophysicae* 27 (4), pp. 1399–1406. DOI: 10.5194/angeo-27-1399-2009.

Feraco, F., R. Marino, L. Primavera, A. Pumir, P. D. Mininni, D. Rosenberg, A. Pouquet, R. Foldes, E. Lévêque, E. Camporeale, S. S. Cerri, H. Charuvil Asokan, J. L. Chau, J. P. Bertoglio, P. Salizzoni, and M. Marro (July 2021). "Connecting large-scale velocity and temperature bursts with small-scale intermittency in stratified turbulence". In: *EPL (Europhysics Letters)* 135.1, p. 14001. DOI: 10.1209/0295-5075/135/14001.

Feraco, F., R. Marino, A. Pumir, L. Primavera, P. D. Mininni, A. Pouquet, and D. Rosenberg (Sept. 2018). "Vertical drafts and mixing in stratified turbulence: Sharp transition with Froude number". In: *EPL (Europhysics Letters)* 123.4, p. 44002. DOI: 10.1209/0295-5075/123/44002.

Forbes, J. M., X. Zhang, S. Palo, J. Russell, C. J. Mertens, and M. Mlynczak (Feb. 2008). "Tidal variability in the ionospheric dynamo region". In: *Journal of Geophysical Research: Space Physics* 113.A2, n/a–n/a. DOI: 10.1029/2007ja012737.

Fritts, David C. (1984). "Gravity wave saturation in the middle atmosphere: A review of theory and observations". In: *Reviews of Geophysics* 22.3, p. 275. DOI: 10.1029/rg022i003p00275.

Fritts, David C. and M. Joan Alexander (Mar. 2003). "Gravity wave dynamics and effects in the middle atmosphere". In: *Reviews of Geophysics* 41.1. DOI: 10.1029/2001rg000106.

Fritts, David C., Gerd Baumgarten, P.-Dominique Pautet, James H. Hecht, Bifford P. Williams, Natalie Kaifler, Bernd Kaifler, C. Bjorn Kjellstrand, Ling Wang, Michael J. Taylor, and Amber D. Miller (May 2023). "Kelvin Helmholtz Instability "Tube" &amp "Knot" Dynamics, Part I: Expanding Observational Evidence of Occurrence and Environmental Influences". In: *Journal of the Atmospheric Sciences*. DOI: 10.1175/jas-d-22-0189.1.

Fritts, David C., Gerd Baumgarten, Kam Wan, Joseph Werne, and Tom Lund (Aug. 2014). "Quantifying Kelvin-Helmholtz instability dynamics observed in noctilucent clouds: 2. Modeling and interpretation of observations". In: *Journal of Geophysical Research: Atmospheres* 119.15, pp. 9359–9375. DOI: 10.1002/2014jd021833.

Fritts, David C., Natalie Kaifler, Bernd Kaifler, Christopher Geach, C. Bjorn Kjellstrand, Bifford P. Williams, S. D. Eckermann, Amber D. Miller, Markus Rapp, Glenn Jones, Michele Limon, Jason Reimuller, and Ling Wang (2020). "Mesospheric Bore Evolution and Instability Dynamics Observed in PMC Turbo Imaging and Rayleigh Lidar Profiling Over Northeastern Canada on 13 July 2018". In: *Journal of Geophysical Research: Atmospheres* 125 (14). DOI: 10.1029/2019JD032037.

Fritts, David C., Brian Laughman, Ling Wang, Thomas S. Lund, and Richard L. Collins (2018). "Gravity Wave Dynamics in a Mesospheric Inversion Layer: 1. Reflection, Trapping, and Instability Dynamics". In: *Journal of Geophysical Research: Atmospheres* 123 (2). DOI: 10.1002/2017JD027440.

Fritts, David C. and Prabhat K. Rastogi (Nov. 1985). "Convective and dynamical instabilities due to gravity wave motions in the lower and middle atmosphere: Theory and observations". In: *Radio Science* 20.6, pp. 1247–1277. DOI: 10.1029/rs020i006p01247.

Fritts, David C. and Li Yuan (1989). "An analysis of gravity wave ducting in the atmosphere: Eckart's resonances in thermal and Doppler ducts". In: *Journal of Geophysical Research* 94.D15, p. 18455. DOI: 10.1029/jd094id15p18455.

García-Comas, M., M. López-Puertas, B. T. Marshall, P. P. Wintersteiner, B. Funke, D. Bermejo-Pantaleón, C. J. Mertens, E. E. Remsberg, L. L. Gordley, M. G. Mlynczak, and J. M. Russell III (2008). "Errors in Sounding of the Atmosphere using Broadband Emission Radiometry (SABER) kinetic temperature caused by non-local-thermodynamic-equilibrium model parameters". In: *Journal of Geophysical Research: Atmospheres* 113.D24. DOI: https://doi.org/10.1029/2008JD010105.

Gerding, Michael, Gerd Baumgarten, Marius Zecha, Franz-Josef Lübken, Kathrin Baumgarten, and Ralph Latteck (June 2021). "On the unusually bright and frequent noctilucent clouds in summer 2019 above Northern Germany". In: *Journal of Atmospheric and Solar-Terrestrial Physics* 217, p. 105577. DOI: 10.1016/j.jastp.2021.105577.

Hartisch, Jennifer, Jorge L. Chau, Ralph Latteck, Toralf Renkwitz, and Marius Zecha (Sept. 2023). "Observations of Polar Mesospheric Summer Echoes Resembling Kilometer-Scale Varicose-Mode Flows". In: DOI: 10.5194/egusphere-2023-1856.

Hauchecorne, A., M. L. Chanin, and R. Wilson (1987). "Mesospheric temperature inversion and gravity wave breaking". In: *Geophysical Research Letters* 14 (9). DOI: 10.1029/GL014i009p00933.

Hines, C. O. (1960). "Internal atmospheric gravity waves at ionospheric heights". In: *CaJPh* 38 (11), p. 1441. DOI: 10.1139/P60-150.

— (1974). "The upper atmosphere in motion". In: *The Upper Atmosphere in Motion*. American Geophysical Union, pp. 14–93. DOI: 10.1029/gm018p0014.

Hozumi, Yuta, Akinori Saito, Takeshi Sakanoi, Atsushi Yamazaki, and Keisuke Hosokawa (2018). "Mesospheric bores at southern midlatitudes observed by ISS-IMAP/VISI: A first report of an undulating wave front". In: *Atmospheric Chemistry and Physics* 18 (22). DOI: 10.5194/acp-18-16399-2018.

Hozumi, Yuta, Akinori Saito, Takeshi Sakanoi, Atsushi Yamazaki, Keisuke Hosokawa, and Takuji Nakamura (2019). "Geographical and Seasonal Variability of Mesospheric Bores Observed from the International Space Station". In: *Journal of Geophysical Research: Space Physics* 124 (5), pp. 3775–3785. DOI: 10.1029/2019JA026635.

Hysell, D. L. and M. F. Larsen (May 2021). "VHF Imaging Radar Observations and Theory of Banded Midlatitude Sporadic iE/i Ionization Layers". In: *Journal of Geophysical Research: Space Physics* 126.5. DOI: 10.1029/2021ja029257.

Isler, Joseph R., Michael J. Taylor, and David C. Fritts (1997). "Observational evidence of wave ducting and evanescence in the mesosphere". In: *Journal of Geophysical Research Atmospheres* 102 (22). DOI: 10.1029/97jd01783.

Jaen, Juliana, Toralf Renkwitz, Jorge Chau, Maosheng He, Peter Hoffmann, Yosuke Yamazaki, Christoph Jacobi, M. Tsutsumi, Vivien Wendt, and Chris Hall (Jan. 2022). "Long-term studies of mesosphere and lower-thermosphere summer length definitions based on mean zonal wind features observed for more than one solar cycle at middle and high latitudes in the Northern Hemisphere". In: *Annales Geophysicae* 40, pp. 23–35. DOI: 10.5194/angeo-40-23-2022.

Kjellstrand, C. Bjorn, David C. Fritts, Amber D. Miller, Bifford P. Williams, Natalie Kaifler, Christopher Geach, Shaul Hanany, Bernd Kaifler, Glenn Jones, Michele Limon, Jason Reimuller, and Ling Wang (2022). "Multi-Scale Kelvin-Helmholtz Instability Dynamics Observed by PMC Turbo on 12 July 2018: 1. Secondary Instabilities and Billow Interactions". In: *Journal of Geophysical Research: Atmospheres* 127.18. e2021JD036232 2021JD036232, e2021JD036232. DOI: https://doi.org/10.1029/2021JD036232.

Kjellstrand, Carl Bjorn, Glenn Jones, Christopher Geach, Bifford P. Williams, David C. Fritts, Amber Miller, Shaul Hanany, Michele Limon, and Jason Reimuller (Aug. 2020). "The PMC Turbo Balloon Mission to Measure Gravity Waves and Turbulence in Polar Mesospheric Clouds: Camera, Telemetry, and Software Performance". In: *Earth and Space Science* 7.8. DOI: 10.1029/2020ea001238.

Latteck, R., W. Singer, M. Rapp, B. Vandepeer, T. Renkwitz, M. Zecha, and G. Stober (Jan. 2012). "MAARSY: The new MST radar on Andøya-System description and first results". In: *Radio Science* 47.1, n/a–n/a. DOI: 10.1029/2011rs004775.

Laughman, B., D. C. Fritts, and J. Werne (2009). "Numerical simulation of bore generation and morphology in thermal and doppler ducts". In: *Annales Geophysicae* 27 (2). DOI: 10.5194/angeo-27-511-2009.

Lecoanet, Daniel, Michael McCourt, Eliot Quataert, Keaton J. Burns, Geoffrey M. Vasil, Jeffrey S. Oishi, Benjamin P. Brown, James M. Stone, and Ryan M. O'Leary (2015). "A Validated Nonlinear Kelvin-Helmholtz Benchmark for Numerical Hydrodynamics". In: DOI: 10.48550/ARXIV.1509.03630.

Lehmacher, G.A., L. Guo, E. Kudeki, P.M. Reyes, A. Akgiray, and J.L. Chau (Jan. 2007). "High-resolution observations of mesospheric layers with the Jicamarca VHF radar". In: *Advances in Space Research* 40.6, pp. 734–743. DOI: 10.1016/j.asr.2007.05.059.

Li, Feng, Gary R Swenson, Alan Z Liu, Michael Taylor, and Yucheng Zhao (Feb. 2007). "Investigation of a "wall" wave event". In: *Journal of Geophysical Research* 112 (D4), p. D04104. DOI: 10.1029/2006JD007213.

Li, Qiang, Jiyao Xu, Jia Yue, Xiao Liu, W. Yuan, B. Ning, Sai Guan, and J. Younger (Mar. 2013). "Investigation of a mesospheric bore event over northern China". In: *Annales Geophysicae* 31, pp. 409–418. DOI: 10.5194/angeo-31-409-2013.

Lighthill, M. J. (1978). "Waves in fluids". In: *Cambridge University Press*. DOI: 10.1002/cpa.3160200204.

Lilly, Douglas K. (Sept. 1966). "On the Instability of Ekman Boundary Flow". In: *Journal of the Atmospheric Sciences* 23.5, pp. 481–494. DOI: 10.1175/1520-0469(1966)023<0481:otioeb>2.0.co;2.

Lübken, F.-J., U. von Zahn, A. Manson, C. Meek, U.-P. Hoppe, F.J. Schmidlin, J. Stegman, D.P. Murtagh, R. Rüster, G. Schmidt, H.-U. Widdel, and P. Espy (Oct. 1990). "Mean state densities, temperatures and winds during the MAC/SINE and MAC/EPSILON campaigns". In: *Journal of Atmospheric and Terrestrial Physics* 52.10-11, pp. 955–970. DOI: 10.1016/0021-9169(90)90027-k.

Lübken, F.-J. (1999). "Thermal structure of the Arctic summer mesosphere". In: *Journal of Geophysical Research: Atmospheres* 104.D8, pp. 9135–9149. DOI: https://doi.org/10.1029/1999JD900076.

Martinis, C., J. Baumgardner, J. Wroten, and M. Mendillo (2018). "All-sky-imaging capabilities for ionospheric space weather research using geomagnetic conjugate point observing sites". In: *Advances in Space Research* 61.7, pp. 1636–1651. DOI: https://doi.org/10.1016/j.asr.2017.07.021.

McEwan, A. D. (Dec. 1971). "Degeneration of resonantly-excited standing internal gravity waves". In: *Journal of Fluid Mechanics* 50.3, pp. 431–448. DOI: 10.1017/s0022112071002684.

— (Apr. 1973). "Interactions between internal gravity waves and their traumatic effect on a continuous stratification". In: *Boundary-Layer Meteorology* 5.1-2, pp. 159–175. DOI: 10.1007/bf02188317.

Medeiros, A., J. Fechine, R. Buriti, Hisao Takahashi, C. Wrasse, and D. Gobbi (Dec. 2005). "Response of OH, O 2 and OI5577 airglow emissions to the mesospheric bore in the equatorial region of Brazil". In: *Advances in Space Research - ADV SPACE RES* 35, pp. 1971–1975. DOI: 10.1016/j.asr.2005.03.075.

Medeiros, A., I. Paulino, M. Taylor, J. Fechine, Hisao Takahashi, R. Buriti, Lourivaldo Lima, and C. Wrasse (Jan. 2016). "Twin mesospheric bores observed over Brazilian equatorial region". In: *Annales Geophysicae* 34, pp. 91–96. DOI: 10.5194/angeo-34-91-2016.

Meriwether, John and Andrew Gerrard (2004). "Mesosphere inversion layers and stratosphere temperature enhancements". In: *Rev. Geophys* 42. DOI: 10.1029/2003RG000133.

Mesquita, Rafael L. A., Miguel F. Larsen, Irfan Azeem, Michael H. Stevens, Bifford P. Williams, Richard L. Collins, and Jintai Li (Aug. 2020). "In Situ Observations of Neutral Shear Instability in the Statically Stable High-Latitude Mesosphere and Lower Thermosphere During Quiet

Geomagnetic Conditions". In: *Journal of Geophysical Research: Space Physics* 125.8. DOI: 10.1029/2020ja027972.

Mondal, S., M. Sivakandan, S. Sarkhel, M. V. Sunil Krishna, Martin G. Mlynczak, James M. Russell, and G. Bharti (2021). "A case study of a thermally ducted undular mesospheric bore accompanied by ripples over the western Himalayan region". In: *Advances in Space Research* 68 (3). DOI: 10.1016/j.asr.2021.03.026.

Nappo, C J (2013). *An introduction to atmospheric gravity waves*. 2nd ed. Elsevier.

Narayanan, V. Lakshmi, S. Gurubaran, and K. Emperumal (2009). "A case study of a mesospheric bore event observed with an all-sky airglow imager at Tirunelveli (8.7°N)". In: *Journal of Geophysical Research Atmospheres* 114 (8). DOI: 10.1029/2008JD010602.

Peterson, Alan W. and Gene W. Adams (1983). "OH airglow phenomena during the 5–6 July 1982 total lunar eclipse". In: *Applied Optics* 22 (17). DOI: 10.1364/ao.22.002682.

Ramachandran, Kesava, Mani Sivakandan, Jorge L. Chau, Juan M. Urco, Michael Gerding, Sven Grundmann, and Steven M. Smith (2023). "Investigation of a Dissipating Mesospheric Bore Using Airglow Imager and Direct Numerical Simulation". In: *Journal of Geophysical Research: Space Physics* 128.4. e2022JA031114 2022JA031114, e2022JA031114. DOI: https://doi.org/10.1029/2022JA031114.

Rapp, M. and F.-J. Lübken (Dec. 2004). "Polar mesosphere summer echoes (PMSE): Review of observations and current understanding". In: *Atmospheric Chemistry and Physics* 4.11/12, pp. 2601–2633. DOI: 10.5194/acp-4-2601-2004.

Rayleigh (1908). "Note on tidal bores". In: *Proceedings of the Royal Society of London. Series A, Containing Papers of a Mathematical and Physical Character* 81 (549). DOI: 10.1098/rspa.1908.0102.

Sarkhel, Sumanta, Gunter Stober, Jorge L Chau, Steven M Smith, Christoph Jacobi, Subarna Mondal, Martin G Mlynczak, and James M Russell III (Mar. 2022). "A case study of a ducted gravity wave event over northern Germany using simultaneous airglow imaging and wind-field observations". In: *Annales Geophysicae* 40 (2), pp. 179–190. DOI: 10.5194/angeo-40-179-2022.

Seyler, C. E. (2005). "Internal waves and undular bores in mesospheric inversion layers". In: *Journal of Geophysical Research D: Atmospheres* 110 (9). DOI: 10.1029/2004JD004685.

She, C. Y., Tao Li, Bifford P. Williams, Tao Yuan, and R. H. Picard (2004). "Concurrent OH imager and sodium temperature/wind lidar observation of a mesopause region undular bore event over Fort Collins/Platteville, Colorado". In: *Journal of Geophysical Research D: Atmospheres* 109 (22). DOI: 10.1029/2004JD004742.

Smith, Anne K. (June 2012). "Global Dynamics of the MLT". In: *Surveys in Geophysics* 33.6, pp. 1177–1230. DOI: 10.1007/s10712-012-9196-9.

Smith, R. K. (1988). "Travelling waves and bores in the lower atmosphere: the 'morning glory' and related phenomena". In: *Earth-Science Reviews* 25 (4), pp. 267–290. DOI: 10.1016/0012-8252(88)90069-4.

Smith, S. M, J. Friedman, S. Raizada, C. Tepley, J. Baumgardner, and M. Mendillo (2005). "Evidence of mesospheric bore formation from a breaking gravity wave event: simultaneous imaging and lidar measurements". In: *Journal of Atmospheric and Solar-Terrestrial Physics* 67.4, pp. 345–356. DOI: 10.1016/j.jastp.2004.11.008.

Smith, S. M., Gunter Stober, Christoph Jacobi, Jorge L. Chau, Michael Gerding, Martin G. Mlynczak, James M. Russell, Jeffrey L. Baumgardner, Michael Mendillo, Monica Lazzarin, and Gabriel Umbriaco (2017). "Characterization of a Double Mesospheric Bore Over Europe". In: *Journal of Geophysical Research: Space Physics* 122 (9). DOI: 10.1002/2017JA024225.

Smith, Steven M., Michael J. Taylor, Gary R. Swenson, Chiao-Yao She, Wayne Hocking, Jeffrey Baumgardner, and Michael Mendillo (2003). "A multidiagnostic investigation of the mesospheric bore phenomenon". In: *Journal of Geophysical Research: Space Physics* 108.A2. DOI: 10.1029/2002ja009500.

Snively, Jonathan B. and Victor P. Pasko (2003). "Breaking of thunderstorm-generated gravity waves as a source of short-period ducted waves at mesopause altitudes". In: *Geophysical Research Letters* 30.24. DOI: https://doi.org/10.1029/2003GL018436.

— (2008). "Excitation of ducted gravity waves in the lower thermosphere by tropospheric sources". In: *Journal of Geophysical Research: Space Physics* 113.A6. DOI: https://doi.org/10.1029/2007JA012693.

Sutherland, Bruce R. (2010). *Internal Gravity Waves*. Cambridge University Press.

Swenson, G R and P J Espy (Oct. 1995). "Observations of 2-dimensional airglow structure and Na density from the ALOHA, October 9, 1993 'storm flight'". In: *Geophysical Research Letters* 22 (20), pp. 2845–2848. DOI: 10.1029/95GL02795.

Swenson, Gary R and Chester S Gardner (Mar. 1998). "Analytical models for the responses of the mesospheric OH* and Na layers to atmospheric gravity waves". In: *Journal of Geophysical Research: Atmospheres* 103 (D6), pp. 6271–6294. DOI: 10.1029/97JD02985.

Taylor, M. J. and M. A. Hapgood (1990). "On the origin of ripple-type wave structure in the OH nightglow emission". In: *Planetary and Space Science* 38 (11). DOI: 10.1016/0032-0633(90)90117-9.

Taylor, M. J., D. N. Turnbull, and R. P. Lowe (1995). "Spectrometric and imaging measurements of a spectacular gravity wave event observed during the ALOHA-93 Campaign". In: *Geophysical Research Letters* 22 (20). DOI: 10.1029/95GL02948.

Urco, Juan M., Jorge L. Chau, Marco A. Milla, Juha P. Vierinen, and Tobias Weber (May 2018). "Coherent MIMO to Improve Aperture Synthesis Radar Imaging of Field-Aligned Irregularities: First Results at Jicamarca". In: *IEEE Transactions on Geoscience and Remote Sensing* 56.5, pp. 2980–2990. DOI: 10.1109/tgrs.2017.2788425.

Urco, Juan Miguel, Jorge Luis Chau, Tobias Weber, and Ralph Latteck (Feb. 2019). "Enhancing the spatiotemporal features of polar mesosphere summer echoes using coherent MIMO and

radar imaging at MAARSY". In: *Atmospheric Measurement Techniques* 12.2, pp. 955–969. DOI: 10.5194/amt-12-955-2019.

Urco Cordero, Juan Miguel Edgar (2020). "Beyond the spatio-temporal limits of atmospheric radars". en. In: DOI: 10.18453/ROSDOK_ID00003356.

Vadas, Sharon L. and Erich Becker (Sept. 2018). "Numerical Modeling of the Excitation, Propagation, and Dissipation of Primary and Secondary Gravity Waves during Wintertime at McMurdo Station in the Antarctic". In: *Journal of Geophysical Research: Atmospheres* 123.17, pp. 9326–9369. DOI: 10.1029/2017jd027974.

Vadas, Sharon L., Jian Zhao, Xinzhao Chu, and Erich Becker (Sept. 2018). "The Excitation of Secondary Gravity Waves From Local Body Forces: Theory and Observation". In: *Journal of Geophysical Research: Atmospheres* 123.17, pp. 9296–9325. DOI: 10.1029/2017jd027970.

Vallis, Geoffrey K. (June 2017). *Atmospheric and Oceanic Fluid Dynamics*. Cambridge University Press.

Wallace, John M. and Peter V. Hobbs (2006). *Atmospheric Science*. Elsevier.

Walterscheid, R. L., J. H. Hecht, R. A. Vincent, I. M. Reid, J. Woithe, and M. P. Hickey (1999). "Analysis and interpretation of airglow and radar observations of quasi-monochromatic gravity waves in the upper mesosphere and lower thermosphere over Adelaide, Australia (35°S, 138°E)". In: *Journal of Atmospheric and Solar-Terrestrial Physics* 61 (6). DOI: 10.1016/S1364-6826(99)00002-4.

Walterscheid, R. L. and M. P. Hickey (June 2011). "Group velocity and energy flux in the thermosphere: Limits on the validity of group velocity in a viscous atmosphere". In: *Journal of Geophysical Research* 116.D12. DOI: 10.1029/2010jd014987.

Yue, Jia, Chiao-Yao She, Takuji Nakamura, Sean Harrell, and Tao Yuan (2010). "Mesospheric bore formation from large-scale gravity wave perturbations observed by collocated all-sky OH imager and sodium lidar". In: *Journal of Atmospheric and Solar-Terrestrial Physics* 72 (1), pp. 7–18. DOI: 10.1016/j.jastp.2009.10.002.

Zhang, Xiaoli, Jeffrey M. Forbes, Maura E. Hagan, James M. Russell, Scott E. Palo, Christopher J. Mertens, and Martin G. Mlynczak (Sept. 2006). "Monthly tidal temperatures 20–120 km from TIMED/SABER". In: *Journal of Geophysical Research* 111.A10. DOI: 10.1029/2005ja011504.

Declaration of Authorship

Ich gebe folgende Erklärung ab:

- Die Gelegenheit zum vorliegenden Promotionsvorhaben ist mir nicht kommerziell vermittelt worden. Insbesondere habe ich keine Organisation eingeschaltet, die gegen Entgelt Betreuerinnen/Betreuer für die Anfertigung von Dissertationen sucht oder die mir obliegenden Pflichten hinsichtlich der Prüfungsleistungen für mich ganz oder teilweise erledigt.
- Ich versichere hiermit an Eides statt, dass ich die vorliegende Arbeit selbstständig angefertigt und ohne fremde Hilfe verfasst habe. Dazu habe ich keine außer den von mir angegebenen Hilfsmitteln und Quellen verwendet und die den benutzten Werken inhaltlich und wörtlich entnommenen Stellen habe ich als solche kenntlich gemacht.

Kesava Ramachandran	Kuehlungsborn, 30.11.2023
Unterschrift	Ort, Datum

Kesava Ramachandran

Date of Birth: 10.05.1992, Indian

Alte Molkerei 3
18225, Kühlungsborn
015901735614
ramachandran@iap-kborn.de

Professional Experience

2018 - 2021 **Research Assistant**, *Leibniz Institute of Atmospheric Physics, Kühlungsborn*

- Mathematical modelling of a new three-dimensional approach to analyse the generation of turbulence in the synoptic- and mesoscales in the lower atmosphere using ICON-IAP.
- Implementation of standard Smagorinsky scheme for horizontal momentum diffusion in ICON-IAP.

Education

2021 - 2024 **Ph.D Student**, *Leibniz Institute of Atmospheric Physics, Kühlungsborn*

- Developing numerical models to study atmospheric instabilities and compare them with observation data from instruments like radars, airglow imagers, and lidars.

2014 - 2017 **Masters in Computational Mechanics**, *University of Duisburg-Essen, Germany*

2013 - 2014 **Deutsch Sprachkurs - DSH(Deutsche Sprachprüfung für den Hochschulzugang)** *Hochschule Wismar, Germany*

2009 - 2013 **Bachelors in Aeronautical Engineering**, *Anna University, India*

1995 - 2009 Primary and High School, India

Publication

- Investigation of a dissipating mesospheric bore using airglow imager and direct numerical simulation, J. Geophys. Res., 128, e2022JA031114, doi:10.1029/2022JA031114, 2023.

Skills

Tools: LINUX, FORTRAN, OpenFOAM, python, Solidworks, Ansys , CATIA V5, STARCCM+

Language Skills: English - Fluent (C2)
German - Business Proficiency (C1)
Spanish - Elementary Proficiency
Tamil (Mother Tongue)

Hobbies

Origami, Rock climbing, Long distance biking, Badminton